Detection, Characterization, and Analysis of Gold Nanoparticles Fate and Dynamics in Aqueous Environment with Advanced Photonics Techniques

Matthew Yunho Chan

Dissertation submitted to the faculty of Virginia Polytechnic Institute and State University in partial fulfillment of the requirements for the degree of

Doctor of Philosophy
In
Civil Engineering

Peter J. Vikesland, Chair
Michael F. Hoechella, Jr.
Linsey C. Marr
Amy J. Pruden-Bagchi

March 24, 2017
Blacksburg, VA

Keywords: Environment; chemistry; nanotechnology; nanomaterials; nanoparticles; gold nanoparticles; groundwater; surface water; halide; Raman spectroscopy; surface-enhanced Raman spectroscopy; SERS; aggregation; deposition; DLVO; photonics; UV-Vis; DLS; fate; transport

Detection, Characterization, and Analysis of Gold Nanoparticles Fate and Dynamics in Aqueous Environment with Advanced Photonics Techniques

Matthew Yunho Chan

Abstract

Increased proliferation of nanotechnology has led to concerns regarding its implication to the water environment. Gold nanoparticles (AuNP) were used as a model nanomaterial to investigate the fate and dynamics of nanoparticles in the complex water environment. A column study was performed to examine the fate and transport of gold nanoparticles with two different coatings in porous media. The resulting data suggested that gold nanoparticles aggregate significantly in the porespace of the column interior, a finding that is not predicted by traditional colloidal filtration theory or Derjaguin-Landau-Verwey-Overbeek (DLVO) theory. Surface-enhanced Raman spectroscopy (SERS) was developed as a new technique to investigate AuNP aggregation in water with varying salt levels. The SERS technique proved valuable as an analytical technique, elucidating information about aggregation as well as AuNP surface interactions with dissolved halides in water. A thorough investigation examining AuNP aggregation with monovalent and divalent salts utilizing SERS, ultraviolet-visible light (UV-Vis) spectroscopy, and dynamic light scattering (DLS) was conducted. Each technique provided data describing different aspects of the dynamic behavior of AuNPs in complex water environments. Results suggest that in addition to attractive and repulsive interactions described by DLVO theory, chemical interactions between the AuNP surface and dissolved halides were also a significant driving force for aggregation and other transformative behaviors of AuNPs in water. The SERS technique developed in this work was shown to be a viable tool to help unveil the vastly complex dynamics of nanomaterial in the water environment.

Detection, Characterization, and Analysis of Gold Nanoparticles Fate and Dynamics in Aqueous Environment with Advanced Photonics Techniques

Matthew Yunho Chan

General Audience Abstract

Nanotechnology is everywhere. It is in our smartphones, in our food, in our clothes, even if we do not recognize it is there. And this is a good thing, because nanotechnology – that is, technology that utilizes nanomaterials – can provide things that traditional technology often cannot. This is all because many nanomaterials have "superpowers" due to their size range: they are generally larger than what we may think of when we think of chemical molecules, but much smaller than macroscopic materials whose behaviors can be approximated by classic physics and chemistry. For example, we all know that gold has a shiny yellow metallic appearance. However, if we make little particles of gold – and these are going to be very tiny, with diameters about 10,000 times smaller than that of a strand of human hair (but about 100 times larger than what we would typically think of as molecules of chemicals) – and put them in water, the resulting mixture will be ruby-red like wine. One of the "superpowers" these gold nanoparticles possess is that they interact with light in a very different way than bulk gold. Currently, researchers in the biomedical field are producing promising work employing these particles in next-generation imaging, and much more. In this study, we were interested in what happens to these materials once they are released to the water environment. Because of the "superpowers" these gold nanoparticles possess, we really do not know how they will behave once they are released to either surface or groundwater because the physics and chemistry of those environments can be quite variable and complex. In this work, we have shown that traditional assumptions about particulate contaminants in water systems do not necessarily hold for gold nanoparticles. Laboratory simulations show that interactions between these particles and the surrounding environment that were once thought to be

negligible, are in fact highly significant. As our title suggests, we are developing new and advanced "photonics" methods to help us discover the dynamic complexity dictating the fate of these gold nanoparticles once they are in the water environment. Photonics methods are techniques that employ light as a probing tool. These techniques use a well understood laser light source that is directed towards the particles in a water environment, and we then measure changes in the scattered light after it has interacted with the particles. The technique we have employed here (called surface-enhanced Raman spectroscopy, or SERS) simultaneously provides us information about different behaviors of gold nanoparticles in water, including how they may aggregate (that is, stick to one another and form big clumps) and how they interact with existing dissolved chemicals that may be present in the natural water environment. By pairing this method with other existing methods, we were able to paint a more complete picture of how these nanoparticles behave in the water environment, and we can answer some questions as to why they do not follow some previously held assumptions. In the end, the work in this dissertation will help future scientists continue to unlock the complexity of nanomaterial fate and dynamics in the water environment.

Acknowledgements

The work in this dissertation would not be possible without the guidance and leadership from my committee members, Dr. Michael Hochella, Dr. Linsey Marr, Dr. Amy Pruden, and especially my committee chair and graduate advisor Dr. Peter Vikesland. My sincerest thanks for their wisdom, their generosity, and their kindness throughout my doctoral studies. Dr. Vikesland in particular gave me opportunities when I didn't think I deserved them, and was and continues to be infinitely patient and wise as my academic mentor. Many thanks also to my friends and colleagues within (or have since departed) the Vikesland Research Group: Dr. Becky Larr, Dr. Ron Kent, Dr. Param Pati, Dr. Xiaojun Chang, Dr. Matt Hull, Dr. Virginia Riquelme, Marjorie Willner, Hossein Abtahi, Haoran Wei, Chang Liu, Brian Sinclair, and many others; as well as other members of the Sustainable Nanotechnology Center: Dr. Carol Johnson, Dr. Nina Vance, Dr. Andrea Tiwari, Dr. James Dale, Dr. Jake Metch, Rui Maia, and many others; your support, friendship, and camaraderie were what kept me going through my long journey pursuing this degree. All work in this dissertation were supported financially by the Center for the Environmental Implication of NanoTechnology, a research center jointly funded by the National Science Foundation and the U.S. Environmental Protection Agency. Additional funding was provided by the Virginia Tech Center for Sustainable Nanotechnology, jointly funded by the Virginia Tech Institute for Critical Technology and Applied Sciences, and the Graduate School. I would also like to express my thanks for additional educational funding provided by the Interdisciplinary Graduate Education Program via the Graduate School, and the Charles E. Via Jr. Department of Civil and Environmental Engineering Department for the PhD Teaching Fellowship. Many thanks must also be given to Dean Karen DePauw of the Graduate School, specifically for the guidance, inspiration, and opportunities she has given through the Transformative Graduate Education initiatives, including but not limited the Preparing for Future Professoriate graduate certificate program, the Global Perspective

Program, and much informal mentoring. Additional leadership opportunities from the Graduate Student Assembly, the Division of Student Affairs, the Office of the Executive Vice President and Provost, and the Office of the President is much appreciated as well. Departmental support, including those from Betty Wingate, Beth Lucas, Jody Smiley, and Julie Petruska from the CEE Department, as well as Will Walton, Monika Gibson, and Lauren Surface from the Graduate School was vital to my experience here at Virginia Tech and many thanks must be given. Finally, I would like thank my friends: friends from the CEE department and neighboring departments – William, Kathleen, Chris, Jake, Dan, Amanda, Laurel, Mary Kate, Pan, Bekah, Matt, Sheldon, Aaron, Walter, Owen, Emily, Billy, Garrett, Ryan, Denise, Ross, Dave, and so many more; friends and colleagues from the GSA and GPP: Greg, Chelsea, Richard, Emma, Ashley, Anjelica, Alex, Sam, Eric, Matt, Kevin, Justin, Connie, Sarah, Mallory, Maria, Jen, and so many, many more folks - I can list names for pages and pages and I only stopped because this is getting ridiculous – and last but not least my family. THANK YOU for supporting me during times that are most difficulty for me; for believing in me when I didn't believe in myself, and reminding me of the one thing that matters. Thank you, with all my heart.

Table of Content

List of Figures

List of Tables

Chapter 1. Introduction

1.1 Background and Motivation

The applications of nanomaterials by industries and their incorporation in consumer products is becoming increasingly popular each year. The U.S. National Nanotechnology Initiative (which coordinates research from government agencies such as the NSF, NIH and EPA) provided as much as $849 million for nanotechnology research funding in the 2004 fiscal year.[1] Consumer products containing nanomaterials experienced a 521% rate of growth between 2006 and 2011.[2] The attraction of nanotechnology to researchers, industry and consumers stems from the fact that many nanomaterials feature novel and unique properties not found in macroscopic materials.[2,3] The novel features that nanomaterials exhibit are wide ranging and can include electronic, optical, thermal, and photoactive properties.[2,4] In particular, gold nanoparticles (AuNPs) show very promising potential applications in many fields including the biomedical industry (for drug delivery and cancer treatment), the material science industry (self-assembly), the environmental and public health sector (sensors for pathogens and contaminants), the chemical industry (low-temperature catalysts and analytical substrates), and many others.[5-15]

While all of these new prospects of technological application are very exciting, there are potential concerns. Production of nanomaterials, and specially manufactured nanoparticles, has increased year after year.[16] In addition, there are (data verified as recently as 2014) steady and significant increases in the availability of nano-enabled consumer products.[17] As of March 2017, there are currently little to no regulations governing the release and disposal of nanomaterials.[18,19] Therefore, it is of little doubt that the release of nanomaterials is occurring right now, and these releases will only increase in magnitude

with time. Nanoparticles that are released can be potentially transported throughout the environment. Depending on their final destination, nanoparticles can partition to the aqueous/marine food web, or to the terrestrial food chain.[20-23] There is evidence that nanomaterials, once consumed by living organisms can readily partition into their cells with potential cytotoxicity effects.[24-27] Hence, it is very important for nanomaterial fate and transport behavior to be fully understood, especially in complex environmental systems.

Historically, suspended particles in aqueous environments of a certain size range (< 1000 nm) were collectively referred to as colloidal materials.[28] Nanomaterial (defined as < 100 nm in one or more dimension) transport in aqueous environment was therefore often treated using classical or modified versions of colloidal theory.[29] For example, when a colloidal- or nano-material is released into the groundwater environment, many potential fates exist. If the chemistry of the pore water and the porous media allow the nanoparticle to remain stably suspended in the pore water, then it is possible that the particles will not be retained within the aquifer, and will eventually be transported out of the groundwater system.[30] On the other hand, attractive interactions (such as van der Waals forces) may overcome repulsive interactions (such as electrostatic forces or double layer interactions) between the nanoparticle and porous media surfaces thus resulting in destabilization.[30] For example, nanoparticles can interact physicochemically with the surface of the porous media (referred to in colloidal theory as a "collector"), where the nanoparticles are immobilized and deposited within the pore space of the aquifer. The nanoparticles themselves can also be attracted to one another, forming larger aggregates, via a process known as homoäggregation. These nanoparticle aggregates can become so large that they are physically strained or filtered by the pore space of the aquifer, or become dense enough to sediment, thus removing them from the groundwater flow.

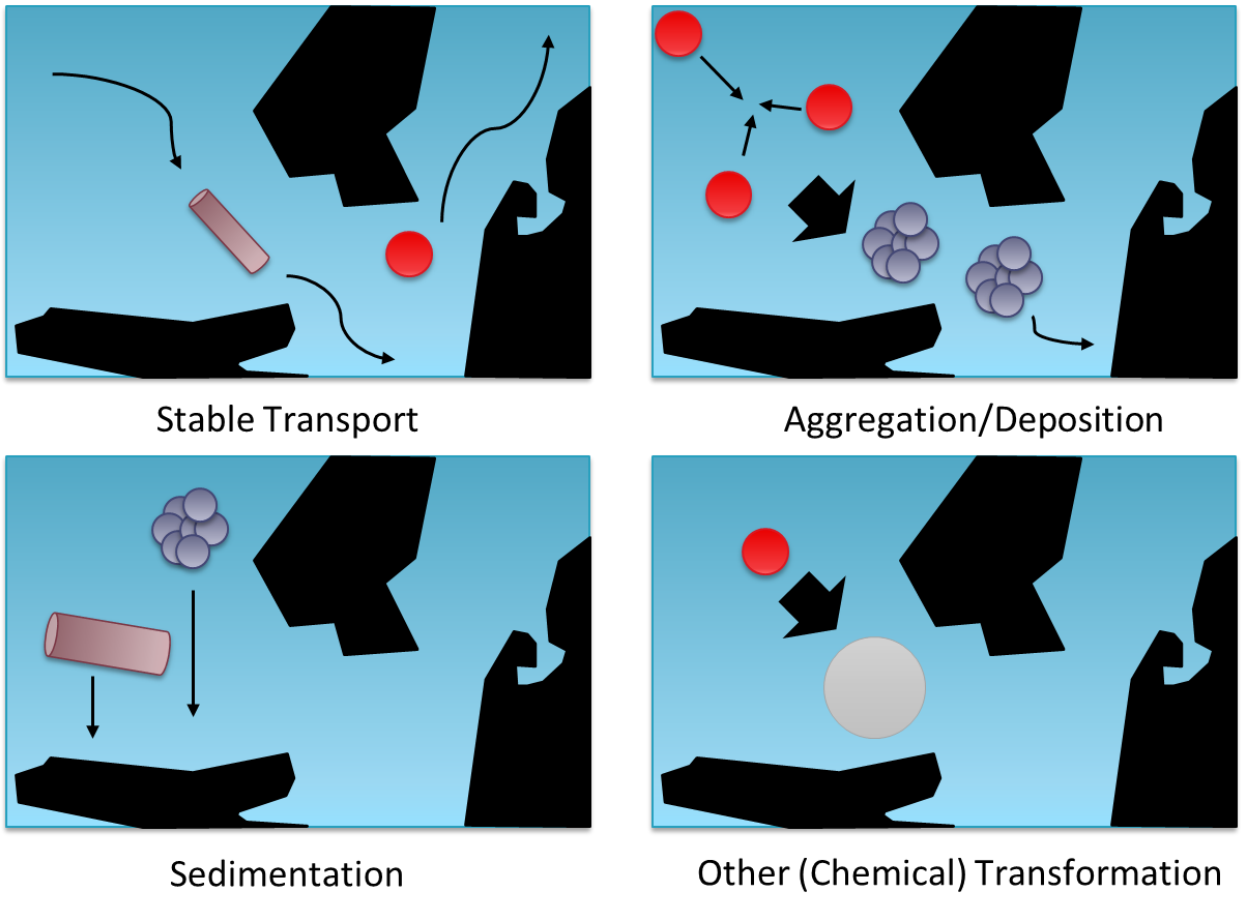

Figure 1-1 – A graphical representation of the complex possibility of fate and transport of nanomaterials in aqueous porous environment.

In reality, the transport behavior of nanoparticles in environmental systems will be a combination of all three of these possibilities (Figure 1-1). The exact mechanisms will be dictated by the surface chemistry of the nanoparticles and the porous media, the solution chemistry of the pore water, and other environmental factors such as temperature, flow rate, and porosity.

Raman spectroscopy has been identified as a strong candidate method that may help elucidate the dynamics of nanomaterial behavior in aqueous systems. Herein, we illustrate the applicability of this method to probe gold nanoparticle interactions in groundwater environments. Raman spectroscopy detects inelastically scattered photons that result from induced dipole interactions (Figure 1-2).[31] Only a very small fraction of the incident photons are scattered inelastically, thus leading to characteristically

weak Raman signals.[32] While it is possible to detect elemental gold crystals via conventional Raman spectroscopy, in our experience the signal is too low to be detectable under our normal operating laser intensity and acquisition time.

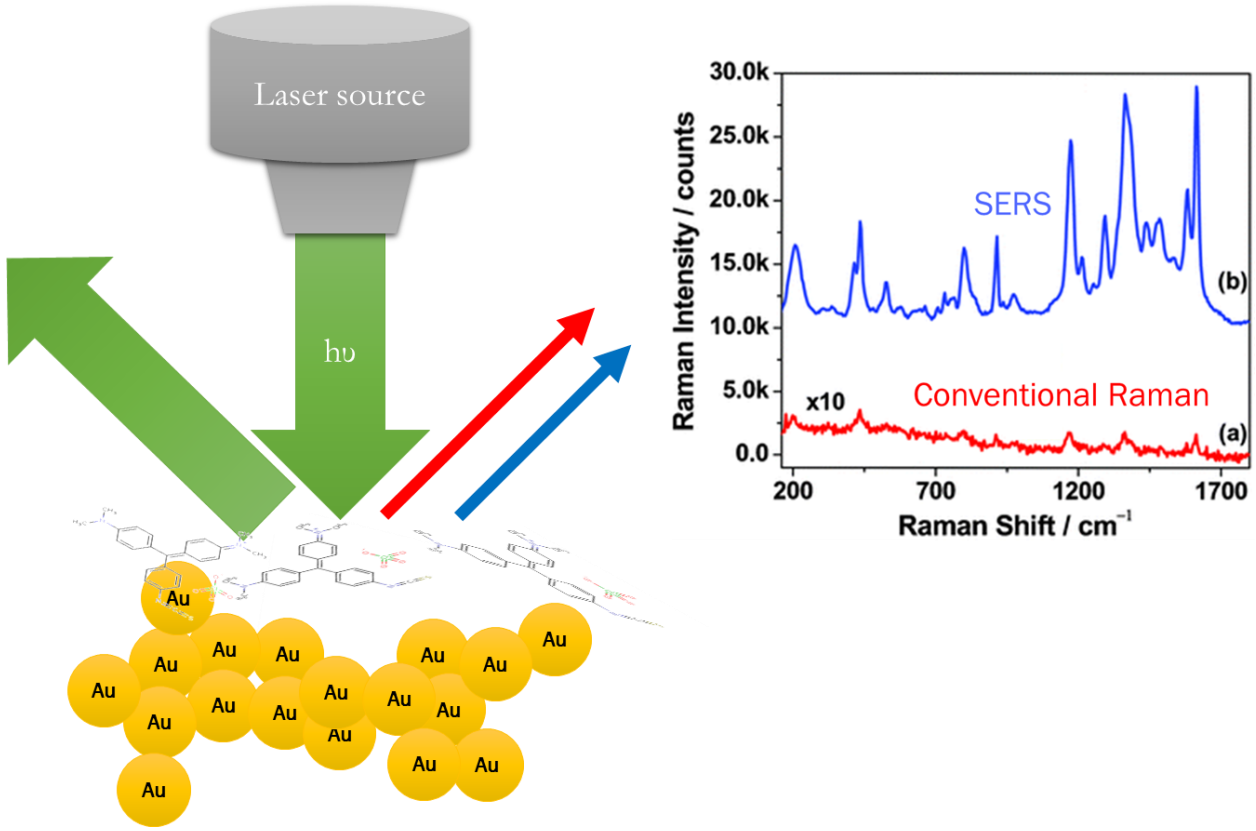

Figure 1-2 – Schematic of how Raman spectroscopy and SERS functions. The incident light (hν) is scattered by samples (the molecule Malachite green isothiocyanate is used here as an example) of interest. Some of the incident photons are absorbed (not shown), a large amount is elastically scattered (i.e., no observable change in energy from the incident photons, represented by large green arrow pointing away from samples), and a very small amount is inelastically scattered (represented by small red and blue arrow; scattered photons that either gained or lost energy.) Because only a small amount of photons is inelastically scattered, conventional Raman spectroscopy typically suffers from low intensity signals (inset spectra, conventional Raman data has been enhanced ten-fold, in this case even after this enhancement the individual peak intensities remain very low.) However, in the presence of a surface-enhancing substrate (in this case, aggregated AuNPs), the resultant SERS spectrum exhibits a dramatically stronger signal.

Herein, surface-enhanced Raman spectroscopy (SERS) was a mechanism we used to boost the weak Raman signals stemming from interactions of interest. Noble metal nanoparticles enhance vibrational Raman bands due to surface plasmon effects.[33] In our case, individual AuNPs generally offer negligible enhancement. However, once aggregated, electromagnetic coupling within AuNP aggregates gives rise to nano-structural 'hotspots' that exhibit higher SERS enhancements than individual nanoparticles (Figure 1-2).[34,35] The formation of such hotspots is a good indication of aggregation behavior for our AuNP systems. In addition, dissolved species in water such as halides (F^-, Cl^-, Br^-, and I^-) undergo strong interactions with the gold surface.[36] These electron rich interactions exhibit relatively large Raman cross-sections and their proximity to an optical enhancer (the gold aggregate surface) results in readily detectable signals that to our knowledge have not been utilized as a mechanism to characterize gold nanoparticle dynamics in aqueous systems.[37] SERS not only allows us to characterize the aggregation and fate of AuNP in water, but also provides the capacity to elucidate information regarding how these nano-aggregates interact with dissolved chemical species in water.

Herein, we present a traditional study of AuNP fate and transport in porous media under varying aqueous conditions. This study, described in **Chapter 2**, illustrates the complexity of AuNP dynamics in the environment and the need for new analytical techniques. Then, in **Chapter 3**, we thoroughly examine the SERS method and its viability to investigate AuNP interaction with dissolved halides in water. Finally, in **Chapter 4**, SERS is used along with ultraviolet-visible light (UV-Vis) spectroscopy and dynamic light scattering (DLS) to analyze AuNP aggregation and transformations in water, with each technique producing data that supplements the others. The combination of new and old analytical techniques will provide us and future scientists with more understanding of the vastly complex behavior of nanoparticles in the water environment.

1.2 Annotated Outline

The following work will be organized this manner:

Chapter 1 – the current chapter, introducing fundamental motivation and background information.

Chapter 2 - Porous Media Induced Aggregation of Protein-Stabilized Gold Nanoparticles

This chapter is a traditional investigation of the fate and transport of AuNP through porous media in a bench-scale column study (Figure 1-3). This column is packed with glass beads to simulate the ground water environment. Two types of AuNP (citrate-coated and protein-coated) were put through the column to examine their fate and transport behavior under varying aqueous environmental conditions.

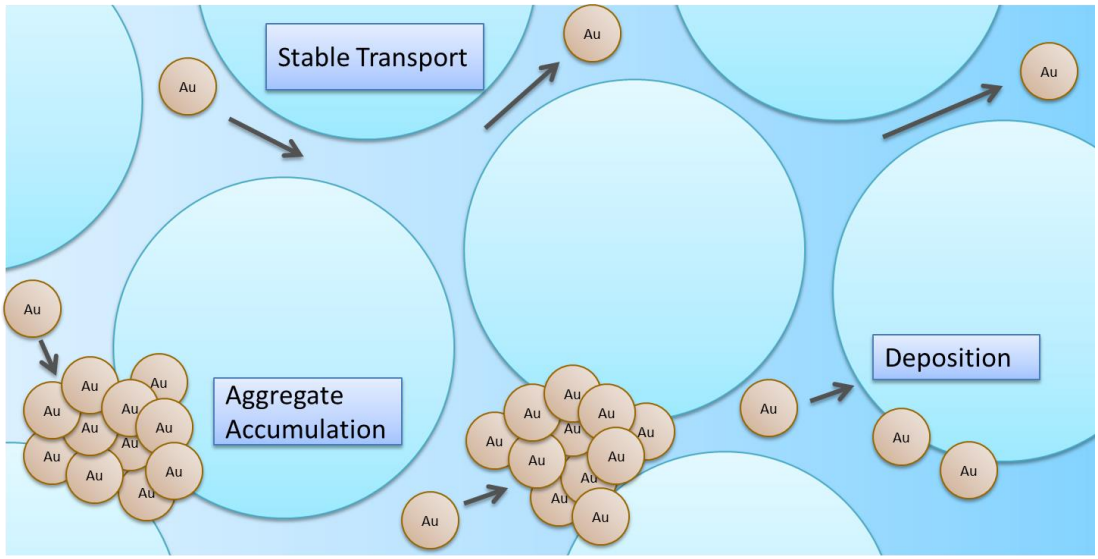

Figure 1-3 – A graphical representation of the interior of the packed column and the various behaviors AuNP may exhibit within the column porespace.[38]

The water chemistry was varied over a range of NaCl and $CaCl_2$ concentrations. The dynamics of AuNP elution from the column were examined and quantified with UV-Vis spectroscopy. This chapter illustrates the gap of knowledge regarding AuNP dynamics in the water environment that exists due to

the use of traditional analytical techniques (column experiments and UV-Vis spectroscopy) as well as classical colloidal theory (colloid filtration theory and DLVO theory).

Note: This chapter has been published by the American Chemical Society: Chan, M. Y.; Vikesland, P. J., Porous Media-Induced Aggregation of Protein-Stabilized Gold Nanoparticles. *Environ. Sci. Technol.* **2014,** *48*, (3), 1532-1540.

Chapter 3 - Surface-Enhanced Raman Spectroscopy Characterization of Salt Induced Gold Nanoparticle Aggregation

This chapter is an investigation of the theory behind the SERS signals resulting from the interaction between gold surfaces and dissolved halides. Surveying the past literature, we determined that SERS bands of interest arise from gold-halide surface interactions, and that these interactions are halide-specific with their vibrational frequencies correlated with the strength of the interaction. We concluded that surface-enhancement is absolutely necessary for the detection of these Raman bands, thus illustrating their usefulness as an indicator of AuNP aggregation.

Note: This chapter is being prepared as a manuscript to be submitted to the German Chemical Society for consideration to be published as a Communication in the journal *Angewandt Chemie-International Edition*.

Chapter 4 - Investigating Mono- and Divalent Cation Induced Aggregation of Gold Nanoparticles in Aqueous Environment via Surface-Enhanced Raman Spectroscopy

This chapter is an investigation utilizing the characteristic Au-X^- SERS bands from Chapter 3 as well as a surface-enhanced Rayleigh band recently described by work conducted elsewhere in the Vikesland

research group to study the aggregation and chemical interactions of AuNP in water. Sodium and calcium halide salts were used in varying concentrations to induce AuNP aggregation with UV-Vis spectroscopy, DLS, and SERS used to monitor their behavior. The collected data showed that despite previous assumptions that electrical double layer effects and van der Waals forces (DLVO theory) are the dominating forces driving AuNP aggregation behavior, in some cases the interactions between halides and the gold nanoparticles have very significant effects that affect aggregation behavior. A preliminary and qualitative investigation into AuNP aggregation and halide attachment kinetics was conducted. Results from this chapter illustrated that multiple analytical techniques were essential to unveil the complex and dynamic behavior of AuNPs in the water environment, and that SERS is a new technique that can be used to elucidate unique and important information.

Note: This chapter is being prepared as a manuscript to be submitted to the Royal Chemical Society for consideration to be published as an Article in the journal *Environmental Science: Nano*.

Chapter 5 – Conclusions and Future Direction

References

1. NNI Supplement to the President's 2016 Budget | Nano.

2. Klaine, S. J.; Alvarez, P. J. J.; Batley, G. E.; Fernandes, T. F.; Handy, R. D.; Lyon, D. Y.; Mahendra, S.; McLaughlin, M. J.; Lead, J. R., Nanomaterials in the environment: Behavior, fate, bioavailability, and effects. *Environ. Toxicol. Chem.* **2008,** *27*, (9), 1825-1851.

3. Bottero, J.-Y.; Wiesner, M. R., *Environmental nanotechnology: applications and impacts of nanomaterials*. McGraw-Hill Professional: 2007; p 553.

4. Petosa, A. R.; Jaisi, D. P.; Quevedo, I. R.; Elimelech, M.; Tufenkji, N., Aggregation and Deposition of Engineered Nanomaterials in Aquatic Environments: Role of Physicochemical Interactions. *Environ. Sci. Technol.* **2010,** *44*, (17), 6532-6549.

5. Ghosh, P.; Han, G.; De, M.; Kim, C. K.; Rotello, V. M., Gold nanoparticles in delivery applications. *Adv. Drug Deliv. Rev.* **2008,** *60*, (11), 1307-1315.

6. Paciotti, G. F.; Myer, L.; Weinreich, D.; Goia, D.; Pavel, N.; McLaughlin, R. E.; Tamarkin, L., Colloidal Gold: A Novel Nanoparticle Vector for Tumor Directed Drug Delivery. *Drug Deliv.* **2004,** *11*, (3), 169-183.

7. Paciotti, G. F.; Kingston, D. G. I.; Tamarkin, L., Colloidal gold nanoparticles: a novel nanoparticle platform for developing multifunctional tumor-targeted drug delivery vectors. *Drug Dev. Res.* **2006,** *67*, (1), 47-54.

8. Visaria, R. K.; Griffin, R. J.; Williams, B. W.; Ebbini, E. S.; Paciotti, G. F.; Song, C. W.; Bischof, J. C., Enhancement of tumor thermal therapy using gold nanoparticle–assisted tumor necrosis factor-α delivery. *Mol. Cancer Ther.* **2006,** *5*, (4), 1014-1020.

9. Visaria, R.; Bischof, J. C.; Loren, M.; Williams, B.; Ebbini, E.; Paciotti, G.; Griffin, R., Nanotherapeutics for enhancing thermal therapy of cancer. *Int. J. Hyperthermia* **2007,** *23*, (6), 501-511.

10. Brust, M.; Bethell, D.; Kiely, C. J.; Schiffrin, D. J., Self-Assembled Gold Nanoparticle Thin Films with Nonmetallic Optical and Electronic Properties. *Langmuir* **1998,** *14*, (19), 5425-5429.

11. Krasteva, N.; Besnard, I.; Guse, B.; Bauer, R. E.; Müllen, K.; Yasuda, A.; Vossmeyer, T., Self-Assembled Gold Nanoparticle/Dendrimer Composite Films for Vapor Sensing Applications. *Nano Lett.* **2002,** *2*, (5), 551-555.

12. Haruta, M., Catalysis of Gold Nanoparticles Deposited on Metal Oxides. *CATTECH* **2002,** *6*, (3), 102-115.

13. Haruta, M., Nanoparticulate Gold Catalysts for Low-Temperature CO Oxidation. *J. New Mat. Electrochem. Syst.* **2004,** *7*, (3), 163-172.

14. Haruta, M., Gold as a novel catalyst in the 21st century: Preparation, working mechanism and applications. *Gold Bull.* **2004,** *37*, (1), 27-36.

15. Halvorson, R. A.; Vikesland, P. J., Surface-Enhanced Raman Spectroscopy (SERS) for Environmental Analyses. *Environ. Sci. Technol.* **2010,** *44*, (20), 7749-7755.

16. Mueller, N. C.; Nowack, B., Exposure Modeling of Engineered Nanoparticles in the Environment. *Environ. Sci. Technol.* **2008,** *42*, (12), 4447-4453.

17. Vance, M. E.; Kuiken, T.; Vejerano, E. P.; McGinnis, S. P.; Jr, M. F. H.; Rejeski, D.; Hull, M. S., Nanotechnology in the real world: Redeveloping the nanomaterial consumer products inventory. *Beilstein Journal of Nanotechnology* **2015,** *6*, (1), 1769-1780.

18. Johnson, D. R.; Methner, M. M.; Kennedy, A. J.; Steevens, J. A., Potential for Occupational Exposure to Engineered Carbon-Based Nanomaterials in Environmental Laboratory Studies. *Environ. Health Perspect.* **2010,** *118*, (1), 49-54.

19. Nowack, B.; Mueller, N. C.; Krug, H. F.; Wick, P., How to consider engineered nanomaterials in major accident regulations? *Environ. Sci. Europe* **2014,** *26*, (1), 2.

20. Judy, J. D.; Unrine, J. M.; Bertsch, P. M., Evidence for Biomagnification of Gold Nanoparticles within a Terrestrial Food Chain. *Environ. Sci. Technol.* **2011,** *45*, (2), 776-781.

21. Gardea-Torresdey, J. L.; Rico, C. M.; White, J. C., Trophic Transfer, Transformation, and Impact of Engineered Nanomaterials in Terrestrial Environments. *Environ. Sci. Technol.* **2014,** *48*, (5), 2526-2540.

22. Ferry, J. L.; Craig, P.; Hexel, C.; Sisco, P.; Frey, R.; Pennington, P. L.; Fulton, M. H.; Scott, I. G.; Decho, A. W.; Kashiwada, S.; Murphy, C. J.; Shaw, T. J., Transfer of gold nanoparticles from the water column to the estuarine food web. *Nat. Nanotechonol.* **2009,** *4*, (7), 441-444.

23. Miralles, P.; Church, T. L.; Harris, A. T., Toxicity, Uptake, and Translocation of Engineered Nanomaterials in Vascular plants. *Environ. Sci. Technol.* **2012,** *46*, (17), 9224-9239.

24. Khan, J. A.; Pillai, B.; Das, T. K.; Singh, Y.; Maiti, S., Molecular Effects of Uptake of Gold Nanoparticles in HeLa Cells. *ChemBioChem* **2007,** *8*, (11), 1237-1240.

25. Oh, N.; Park, J.-H., Surface Chemistry of Gold Nanoparticles Mediates Their Exocytosis in Macrophages. *ACS Nano* **2014,** *8*, (6), 6232-6241.

26. Liu, X.; Huang, N.; Li, H.; Jin, Q.; Ji, J., Surface and Size Effects on Cell Interaction of Gold Nanoparticles with Both Phagocytic and Nonphagocytic Cells. *Langmuir* **2013,** *29*, (29), 9138-9148.

27. Pan, Y.; Neuss, S.; Leifert, A.; Fischler, M.; Wen, F.; Simon, U.; Schmid, G.; Brandau, W.; Jahnen-Dechent, W., Size-Dependent Cytotoxicity of Gold Nanoparticles. *Small* **2007,** *3*, (11), 1941-1949.

28. Robertson, W. D.; Barker, J. F.; LeBeau, Y.; Marcoux, S., Contamination of an Unconfined Sand Aquifer by Waste Pulp Liquor: A Case Study. *Ground Water* **1984,** *22*, (2), 191-197.

29. Elimelech, M.; Gregory, J.; Jia, X.; Williams, R., *Particle deposition and aggregation: measurement, modelling and simulation*. Butterworth-Heinemann: 1998; p 459.

30. McCarthy, J. F.; Zachara, J. M., Subsurface transport of contaminants. *Environ. Sci. Technol.* **1989,** *23*, (5), 496-502.

31. Pelletier, M. J., *Analytical Applications of Raman Spectroscopy*. 1 edition ed.; Blackwell Publishing: Osney Mead, Oxford ; Malden, MA, 1999; p 496.

32. Long, D. A., *Raman spectroscopy*. McGraw-Hill International Book Company: London, 1977.

33. Smith, E.; Dent, G., *Modern Raman Spectroscopy: A Practical Approach*. John Wiley & Sons: 2013; p 216.

34. Blatchford, C. G.; Campbell, J. R.; Creighton, J. A., Plasma resonance—enhanced Raman scattering by absorbates on gold colloids: the effects of aggregation. *Surf. Sci.* **1982,** *120*, (2), 435-455.

35. Creighton, J. A.; Blatchford, C. G.; Albrecht, M. G., Plasma resonance enhancement of Raman scattering by pyridine adsorbed on silver or gold sol particles of size comparable to the excitation wavelength. *J. Chem. Soc. Faraday II* **1979,** *75*, 790.

36. Cotton, F. A.; Wilkinson, G.; Murillo, C. A.; Bochmann, M., *Advanced Inorganic Chemistry*. 6 edition ed.; Wiley-Interscience: New York, 1999; p 1376.

37. Alvarez-Puebla, R. A.; Liz-Marzán, L. M., SERS Detection of Small Inorganic Molecules and Ions. *Angew. Chem.-Int. Edit.* **2012,** *51*, (45), 11214-11223.

38. Chan, M. Y.; Vikesland, P. J., Porous Media-Induced Aggregation of Protein-Stabilized Gold Nanoparticles. *Environ. Sci. Technol.* **2014,** *48*, (3), 1532-1540.

Chapter 2. Porous Media Induced Aggregation of Protein-Stabilized Gold Nanoparticles

Matthew Y. Chan and Peter J. Vikesland

The Charles E. Via, Jr. Department of Civil and Environmental Engineering, Virginia Tech, Blacksburg, VA, USA.

Institute for Critical Technology and Applied Science, Virginia Tech, Blacksburg, VA, USA.

NSF-EPA Center for the Environmental Implications of Nanotechnology, Duke University, Durham, NC, USA

2.1 Abstract

Gold-nanoparticles (AuNPs) are employed for cancer treatment, drug delivery, chemical analyses, and many other uses. As AuNP manufacture increases it is imperative that we understand the environmental fate of these nanomaterials. We investigated the transport and stability of AuNP under simulated groundwater conditions. Batch experiments indicated that 16 nm AuNP stabilized with bovine serum albumin (BSA-cit-AuNP) was slightly more stable under high ionic strength conditions than citrate-functionalized AuNP (cit-AuNP) of the same core size. Both types of AuNP were injected into glass bead packed columns and subjected to transport with varying NaCl and $CaCl_2$ concentrations. BSA-cit-AuNP deposited less than cit-AuNP in the presence of increasing concentrations of $CaCl_2$, but the opposite trend was observed in the presence of increasing concentrations of NaCl. This finding differed from the results obtained in the batch studies. Calculated attachment efficiencies (α) failed to reflect the observed experimental column data, with α at maximum only approaching 0.1 even though a majority of the AuNPs were retained in the column. Colloid filtration theory fails to predict and explain this

discrepancy. We conclude that media induced nanoparticle aggregation is responsible for the inconsistency.

2.2 Introduction

Nanomaterials exhibit novel characteristics not possessed by their bulk counterparts. In the case of gold nanoparticles (AuNPs), these unusual properties have led to the development of AuNP based tumor targeting vectors and sensing agents.[1-5] Unfortunately, to date there are few regulations governing nanomaterial release and disposal.[1] Because of their increased use and application there is little doubt that AuNP nanomaterial discharges are currently occurring and that the quantities released will only increase with time. AuNPs discharged into the environment will be subject to transport and it is expected that they will partition to the aqueous/marine food web as well as the terrestrial food chain.[2,3]

Nanoparticle surfaces are modified for a variety of reasons. For example, citrate is a common surface coating for AuNP because it is often present during AuNP synthesis as both reducing agent and dispersant.[4,5] In addition, to enhance their colloidal stability many nanoparticles are coated with polymers or other macromolecules.[6-12] When either surface functionalized or 'bare' nanoparticles are used for biomedical applications they become stabilized by a non-specifically bound protein layer.[13] Bovine serum albumin (BSA) is a well characterized protein that is used both medically and as a model for the examination of AuNP-protein interactions because serum albumins are the most abundant proteins in blood plasma.[14,15] BSA is a globular protein consisting of 583 amino acid residues with a molecular weight of 66.4 kDa and an isoelectric point of 4.7.[16,17] Nanoparticles coated by either citrate or proteins such as BSA are expected to behave very differently from one another in environmental matrices due to physicochemical differences between the coatings.

Recent work has established that proteins such as BSA are non-specifically bound to citrate-stabilized AuNP (cit-AuNP) and that the citrate layer is retained.[18,19] For this reason, we refer to BSA functionalized

AuNP as BSA-cit-AuNP. Given the prevalence and utility of protein functionalized AuNP to the biomedical industry, it is reasonable to conclude that large quantities of discharged AuNP will be non-specifically functionalized with proteins or other macromolecules. In addition, and of significant importance from an environmental perspective, proteins are a major component of wastewater effluents and thus AuNPs in wastewater discharges can be expected to have proteins associated with them.[20]

At present there is a lack of understanding of how non-specifically bound surface coatings affect nanoparticle fate and transport. The literature often suggests that thicker coatings such as proteins or polymers promote nanoparticle stability and transport in the environment,[10,21,22] however, this hypothesis has never been tested for BSA stabilized AuNPs, especially in a groundwater context. In this study, we compared the stability of cit-AuNP and BSA-cit-AuNP in both batch and transport experiments. Elucidating differences in the interactions of "bare" cit-AuNP and protein-coated-AuNP in aqueous environments is essential to a holistic understanding of how different stabilizing coatings affect nanoparticle fate and transport in environmental media.

2.3 Methods

All reagents were purchased from Fisher Scientific. All water used in these experiments was ultrapure with resistivity >18.2 MΩ·cm (Barnstead Nanopure, Thermo Scientific). All glassware was cleansed using a laboratory disinfector-washer (Lancer 1400 LXP, Lancer Industry). All glassware in contact with AuNP was additionally cleaned with aqua regia to ensure removal of remnant gold and then copiously rinsed with ultrapure water.

2.3.1 Preparation and Characterization of the Porous Media

Spherical soda-lime glass beads (260 μm; MO-SCI) were used as the porous medium in column experiments. Scanning electron microscopy analysis of the beads was consistent with this reported diameter and indicated that a majority of the glass beads did not have any discernible imperfections. Prior to use, the beads were extensively washed via the method of Tufenkji *et al*.[23] Streaming potential measurements were performed on ≈2 g glass bead samples using an electrokinetic analyzer (SurPASS, Anton Paar). The measured streaming potentials were converted into zeta potentials via Henry's equation by the on-board software.[24-26]

2.3.2 AuNP Synthesis and Characterization

Cit-AuNP of ≈16 nm diameter were prepared as described by Turkevich.[4] BSA-cit-AuNP were prepared by incubating cit-AuNP with 0.1 mg/mL BSA as described by Ao *et al*.[27] All suspensions were filter-sterilized (0.22 μm pore size) and stored in the dark at 4 °C. Both cit-AuNP and BSA-cit-AuNP were analyzed by transmission electron microscopy (TEM). A Zeiss 10CA TEM operating at 60 kV (Advanced Microscopy Techniques Corp.) was used to determine size and morphology. Micrographs were analyzed using Image-J (National Institutes of Health) to quantify the AuNP core size. The electrophoretic properties of AuNP were measured using a Zetasizer NanoZS (Malvern Instruments) particle analyzer equipped with a MPT-2 autotitrator. AuNP suspensions in 2 mM $NaHCO_3$ (pH≈8.2) were titrated with either NaCl or $CaCl_2$ and the electrophoretic mobility (EPM) was determined at each point of the titration. The NanoZS was also used to obtain dynamic light scattering (DLS) measurements of the Z_{ave} particle size distributions for both types of AuNP suspensions via the method of cumulants.

Total gold concentrations of the stock AuNP were measured by inductively coupled plasma mass spectrometry (X-Series ICP-MS, Thermo Scientific). For this purpose, a 2 μL aliquot of aqua regia was added to a 1 mL sample of AuNP suspension and the resulting solution was analyzed according to

Standard Method 3125B.[28] The concentrations of the stock suspensions (both cit- and BSA-cit-AuNP) used for the column experiments were ≈160 mg/L. In a column experiment, following dilution of the stock AuNP suspension by the mobile phase, the initial concentration of AuNP entering the column was ≈25 mg/L.

UV-Vis spectroscopy was used to quantify AuNP concentrations. Calibration curves plotting the intensity of the absorbance maximum of the localized-surface plasmon resonance (LSPR) band for AuNP (520 nm for cit-AuNP and 526 nm for BSA-cit-AuNP) as a function of AuNP concentration were obtained prior to a column experiment. Molar extinction coefficients obtained for multiple calibration curves ranged between 0.018-0.022 $M^{-1}cm^{-1}$ ($\bar{x} = 0.02,\ n = 33,\ s_n = 9.3 \times 10^{-4}$). The extinction coefficients from the calibration curves have a very narrow range and a very small standard deviation (s_n) thus illustrating the consistency of the system.

2.3.3 Batch Experiments

Batch experiments were conducted by adding aliquots of stock salt solutions to achieve final concentrations of 5-80 mM NaCl or 0.1–1.0 mM $CaCl_2$ in cit-AuNP or BSA-cit-AuNP suspensions in the presence of 2 mM of $NaHCO_3$ buffer. Time-resolved UV-Vis spectroscopy was conducted with periodic scanning from 400–600 nm. A parallel set of batch experiments was conducted to examine cit-AuNP stability in the presence of the glass beads. Briefly, 10 g of glass beads were incubated in Erlenmeyer flasks containing 24.5 mg/L cit-AuNP and varying [NaCl]. Additional flasks with the same AuNP content, but without glass beads served as controls. Aliquots from the flask were periodically withdrawn and were analyzed by UV-Vis spectroscopy.

2.3.4 Column Experiments

Deposition experiments were performed using a glass column with dimension 1.6 (I.D.) × 10 cm (C 10/20, GE Healthcare). The column was dry packed to a 10 cm depth. The total pore volume (V_{pore}) and porosity (ε) of the column were determined by comparing the dry weight of the packed column to the weight of a water filled (but without porous media) column. V_{pore} and ε were set to ≈4.30 mL and 34%, respectively. A mobile phase of 2 mM $NaHCO_3$ was introduced at high flow (≈30 mL/min) to saturate the column, thereafter the flow was decreased to the experimental flow rate, and the column was equilibrated for $10V_{pore}$. As shown in Figure A-1 our column packing protocol enabled collection of highly reproducible breakthrough curves for any given experimental condition.

A large volume syringe pump (Model 500D, Teladyne ISCO) was used to supply mobile phase that was mixed with the flow from a smaller pump (PHD2000, Harvard Apparatus) injecting AuNP into the column. An injection volume equal to $5V_{pore}$ was used, and give a total flow rate of 2.843 mL (i.e., a Darcy velocity of 0.00023 m/s, a value consistent with groundwater flow rates)[29], this combination corresponds to a 7.5 min injection time. The effluent from the column passed through a quartz flow-cell (Starna Cells) for UV-Vis analysis. Mobile phase contained 2 mM $NaHCO_3$ buffer with either 10-100 mM NaCl or 0.1-1.0 mM $CaCl_2$. Prior to and after each AuNP experiment, an inert $NaNO_3$ solution was injected into the column as a tracer and the effluent nitrate concentration was evaluated spectrophotometrically at 302 nm.[30] There were no discernible changes in the tracer profiles following an experiment, thus indicating that AuNP retention did not significantly alter the porous media transport characteristics (Figure A-2).

2.4 Results and Discussion

2.4.1 Nanoparticle and Porous Media Characterization

The AuNP used herein have an average core diameter (d_{TEM}) of 16±1.2 nm (n=200) as determined via TEM (Figure A-3). DLS measurements indicate Z_{ave} hydrodynamic diameters (d_{DLS}) of 19.7±0.1 nm and 29.4±0.1 nm for cit-AuNP and BSA-cit-AuNP, respectively. These measurements indicate that both types of AuNP were relatively monodisperse. The increase in d_{DLS} for BSA-cit-AuNP relative to cit-AuNP is consistent with a protein over-layer or "corona" surrounding the nanoparticles.[31] Quartz crystal microbalance studies suggest that a monolayer of BSA has dimension of ≈6-7 nm and thus the measured increase in diameter of ≈10 nm for BSA-cit-AuNP is consistent with monolayer adsorption.[18,32] The larger value for d_{DLS} relative to d_{TEM} for cit-AuNP is expected due to the presence of a surface hydration layer that would not be detected by TEM.

EPM measurements were obtained to evaluate the surface charge of cit-AuNP and BSA-cit-AuNP under conditions representative of those used in the batch and deposition studies. As summarized in Table S1, the EPMs of cit-AuNP and BSA-cit-AuNP in 2 mM $NaHCO_3$ at pH=8.2 were -3.01±0.06 and -1.93±0.11 $\mu m \cdot cm \cdot V^{-1} \cdot s^{-1}$, respectively, with corresponding zeta potentials of -38.4±1.00 mV and -24.6±1.64 mV, respectively. The Smoluchowski equation enabling the calculation of zeta potential from raw EPM data is valid for cit-AuNP;[33] however, there is debate about the validity of this calculation for BSA-cit-AuNP. Nonetheless, zeta potential values are reported for consistency with the literature. The decrease in the apparent surface charge following association of BSA with the particles is consistent with a past report that suggested that citrate forms a "salt bridge" with amino acid groups in BSA.[14]

Electrolyte titrations were conducted to examine how changes in solution composition affect AuNP surface charge. The concentration ranges of NaCl and $CaCl_2$ employed were chosen to represent the range of ionic strengths relevant to the column experiments discussed *vide infra*. The titration results are summarized here and presented in the SI. As shown in Figure A-4, there is a subtle, yet discernible decrease in the magnitude of the EPM of AuNP with an increase in ionic strength. As expected, the EPM

of BSA-cit-AuNP was less than that of cit-AuNP as past studies have shown that proteins such as BSA alter the properties of the nanoparticles such that they behave more like the protein itself.[34,35] According to the Schultz-Hardy rule Ca^{2+} is expected to exert a greater charge screening effect that will destabilize colloidal suspensions at lower relative ionic strengths.[36,37] Under our experimental conditions, however, comparative evaluation of charge-screening effects was not possible due to our use of widely divergent NaCl and $CaCl_2$ concentrations.

Surface charge characterization of the glass beads was conducted across a majority of the experimental NaCl and $CaCl_2$ concentration ranges. However, due to an instrument ionic strength limitation of 10 mM NaCl the streaming potential measurements were restricted by this upper maximum. Nonetheless, trends in zeta potential with changes in salt content are apparent as summarized in Figure 2-1. The zeta potential of the glass beads was ≈-80 mV at ambient salt concentration (2 mM $NaHCO_3$) and then decreased to ≈-55 mV at the highest $CaCl_2$ concentration. At 10 mM NaCl, the zeta potential was ≈-35 mV. Based upon the trends in Figure 2-1 and the literature[38] it is reasonable to conclude that for [NaCl] >10 mM the zeta potential will be near neutral. A near neutral zeta potential implies that deposition to the surface of the glass beads will be not be electrostatically hindered.

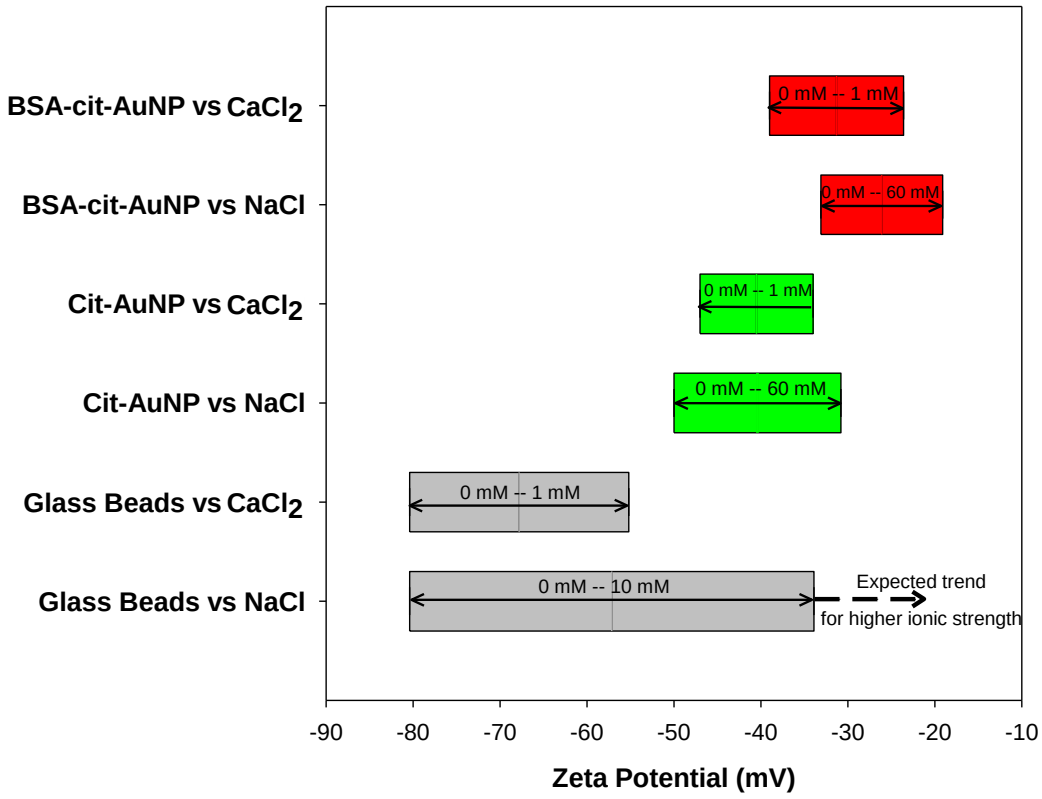

Figure 2-1 - Summary of zeta potential data for conditions representative of those used in the column experiments. Zeta potential of AuNP obtained by electrophoretic mobility measurements; zeta potential of glass beads obtained by streaming potential measurements.

2.4.2 Batch Experiments with cit-AuNP and BSA-AuNP

Time-resolved UV-Vis spectra indicate that both cit-AuNP and BSA-cit-AuNP exhibit short-term colloidal stability over a wide range of salt concentrations. As shown in Figures 2-1A and A-5A to A-7A there was no observed shift or decline in the LSPR peak over a ten-minute timeframe (we note this timeframe was used to match the in-column residence times). If significant nanoparticle aggregation had occurred over this timescale an observable red-shift in the LSPR band, a measurable decline in extinction intensity, and formation of a secondary LSPR band would be observed.[39] Such outcomes are discernible at longer timescales for cit-AuNP (data not shown), but not within a ten-minute period. We note that at

the highest salt concentrations, BSA-cit-AuNP is more resistant to destabilization as indicated by the greater stability of the LSPR band. For cit-AuNP at high [NaCl] and [$CaCl_2$] there is evidence of destabilization as indicated by time-dependent fluctuations in the spectra. These batch experiment results along with the zeta potential

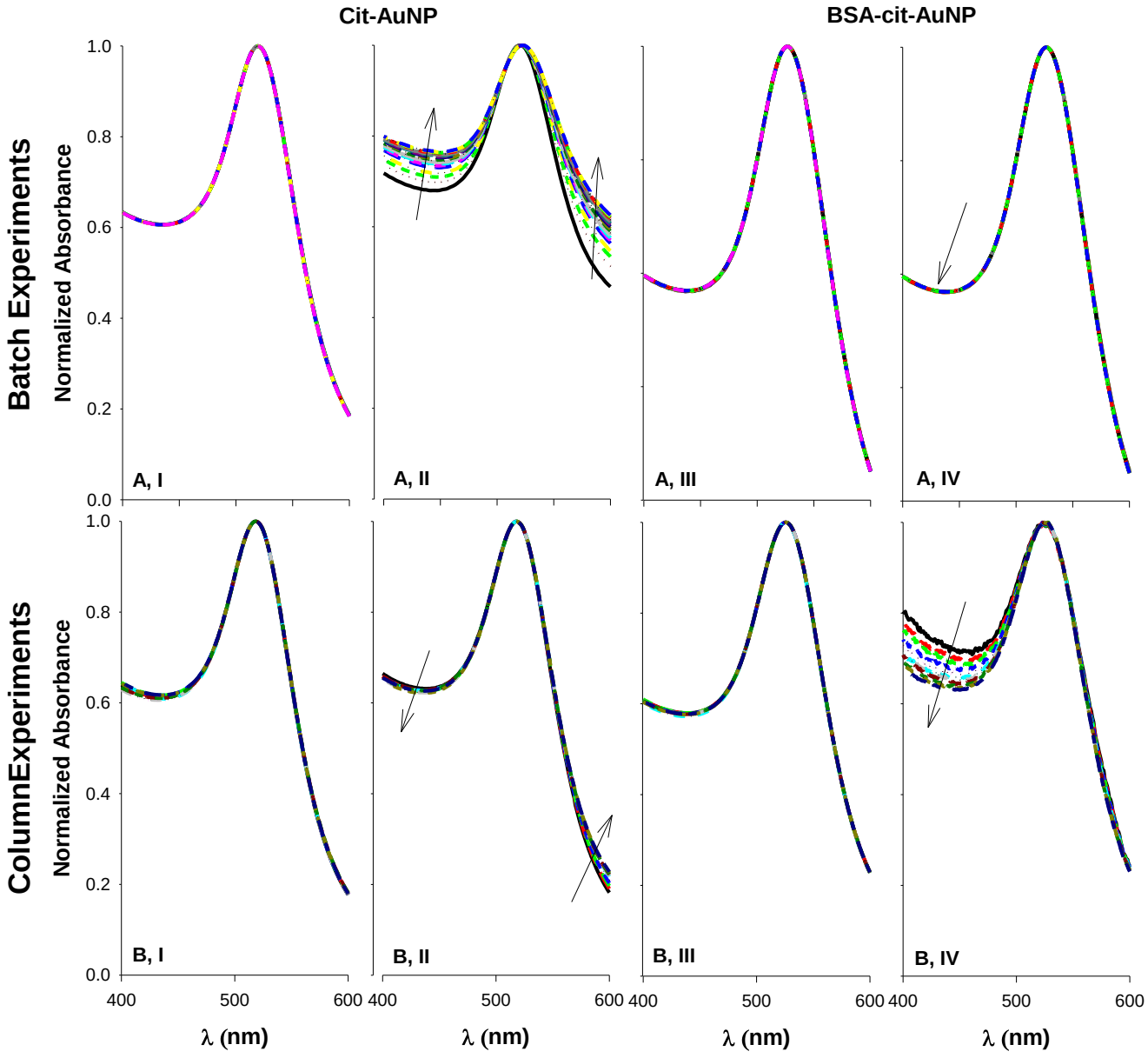

Figure 2-2 – UV-Vis spectra for batch and column experiments with NaCl. As labeled, the four graphs on the left are for cit-AuNP, while the graphs on the right are for BSA-cit-AuNP. Plots in the top row (A) are batch experimental results ($0 < t < 10.5$ minutes) and plots in the second row (B) are column effluent data ($2.8 < V_{pore} < 6.1$). NaCl concentrations: I = 20 mM, II = 40 mM, III = 5 mM, IV = 22 mM. All column effluent data are for V_{pore} values representative of the breakthrough curve plateau region. All data points were normalized by the LSPR maxima to account for slight differences in AuNP

concentration. The corresponding absolute absorbance data may be found in the SI. The arrows denote time-variant changes in the collected data. Arrows indicate time progression.

results indicate the BSA coating provides a stabilizing electrosteric repulsive force between individual AuNP. Because BSA decreases the measured EPM of the AuNP, while increasing its stability, it is reasonable to conclude that the primary stabilizing force is steric in nature.

2.4.3 Cit-AuNP Column Experiments

Experiments with variable NaCl and $CaCl_2$ showed that as the mobile phase electrolyte concentration increased that greater amounts of cit-AuNPs were retained in the column (Figure 2-3). An increase in ionic strength decreases repulsion between the AuNP and the glass beads and thus enhances AuNP retention. Similar trends have been observed in previous column studies with a variety of nanomaterials.[40] At comparable ionic strengths, Ca^{2+} is expected to be more effective at compressing the double layer, destabilizing colloidal suspensions[36,37] and enhancing deposition.[41] As expected, much lower concentrations of $CaCl_2$ were required to achieve similar levels of cit-AuNP retention within the columns relative to NaCl (compare Figures 2-3A and 2-3B). The differential destabilizing capacity of the monovalent and divalent salts is consistent with previously reported results. In a study examining *n*C_{60} transport through porous media both 10 mM $CaCl_2$ and 60 mM NaCl produced similar breakthrough curves.[42]

We highlight the changing slopes in the "plateau region" of the breakthrough curves (Figures 2-3A & 2-3B), which are consistent with the sloping plateaus observed in parallel experiments examining cit-AuNP transport as a function of V_{pore} in the presence of 30 mM NaCl (Figure A-8). The slope of the plateau region changes from positive to negative with an increase in electrolyte concentration. The change in slopes, as summarized in Figure A-9, is consistent with some previous studies.[43-45] In the case where the slope in the plateau region is positive, this may be due to negatively charged AuNP blocking

less negatively charged deposition sites on the glass bead surface such that deposition is repulsively hindered.[46] The switch from positive to negative slope is similar to a result obtained by Solovitch *et al.* in their C_{60} column deposition experiments.[44] The negative slope is evidence of surface ripening of the glass beads.[47-49] A simple batch experiment suggests that a surface interaction between the glass beads

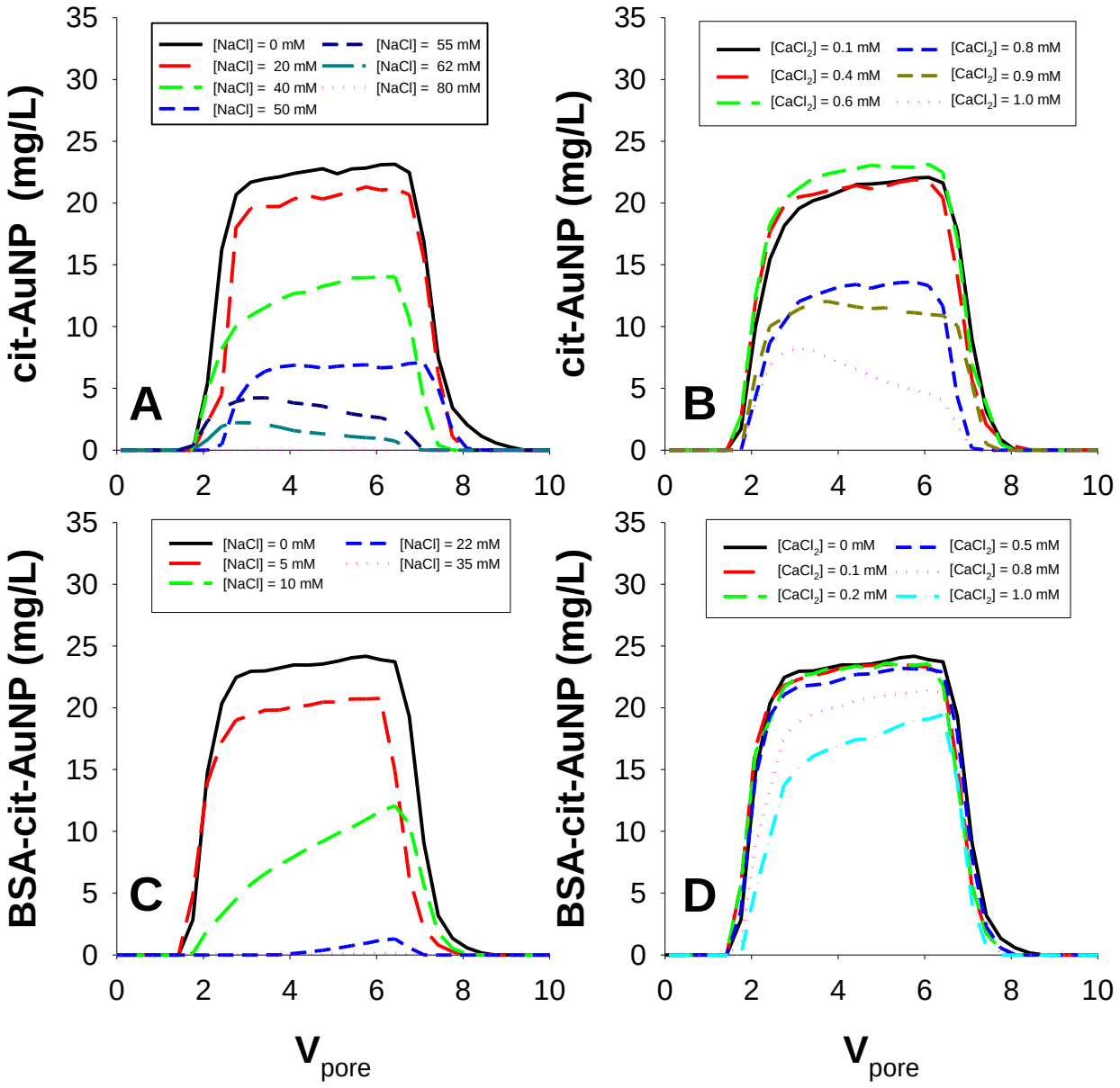

Figure 2-3 - AuNP breakthrough curves with varying [NaCl] and [$CaCl_2$]. A) cit-AuNP and [NaCl], B) cit-AuNP and [$CaCl_2$], C) BSA-cit-AuNP and [NaCl], and D) BSA-cit-AuNP and [$CaCl_2$]. The mobile phase contained a variable amount of NaCl or $CaCl_2$ and 2 mM $NaHCO_3$ as buffer. C_0 for cit-AuNP was

≈24.5 mg/L; C_0 for BSA-cit-AuNP was ≈25.4 mg/L. Additional data sets were obtained for other electrolyte concentrations, but only a select few are presented here for clarity.

and cit-AuNP can accelerate cit-AuNP aggregation (Figure A-10). Aggregation within the column porespace would lead to increased AuNP retention.

2.4.4 BSA-cit-AuNP Column Experiments

To evaluate the effects of surface associated BSA on AuNP transport, a set of column experiments were conducted under conditions identical to those for cit-AuNP (Figures 2-3C & 2-3D). As discussed previously, in batch systems BSA-cit-AuNP was more resistant to salt mediated destabilization than cit-AuNP. It might therefore be anticipated that electrosteric effects would also inhibit AuNP deposition. As shown by comparing Figures 2-3B and 2-3D, this expectation was confirmed for $CaCl_2$ as significantly more BSA-cit-AuNPs were recovered from the column than cit-AuNP. However, for column experiments with NaCl and BSA-cit-AuNP, the protein-coated particles were heavily retained within the column at relatively low [NaCl] (Figure 2-3C). As shown in Figure 2-4A, for 22 mM NaCl, ≈70% of cit-AuNP was recovered in the column effluent, while only ≈3% of BSA-cit-AuNP was recovered. This trend differs completely from that for $CaCl_2$ (Figure 2-4B) in that BSA-cit-AuNP was more resistant to $CaCl_2$-induced destabilization relative to cit-AuNP.

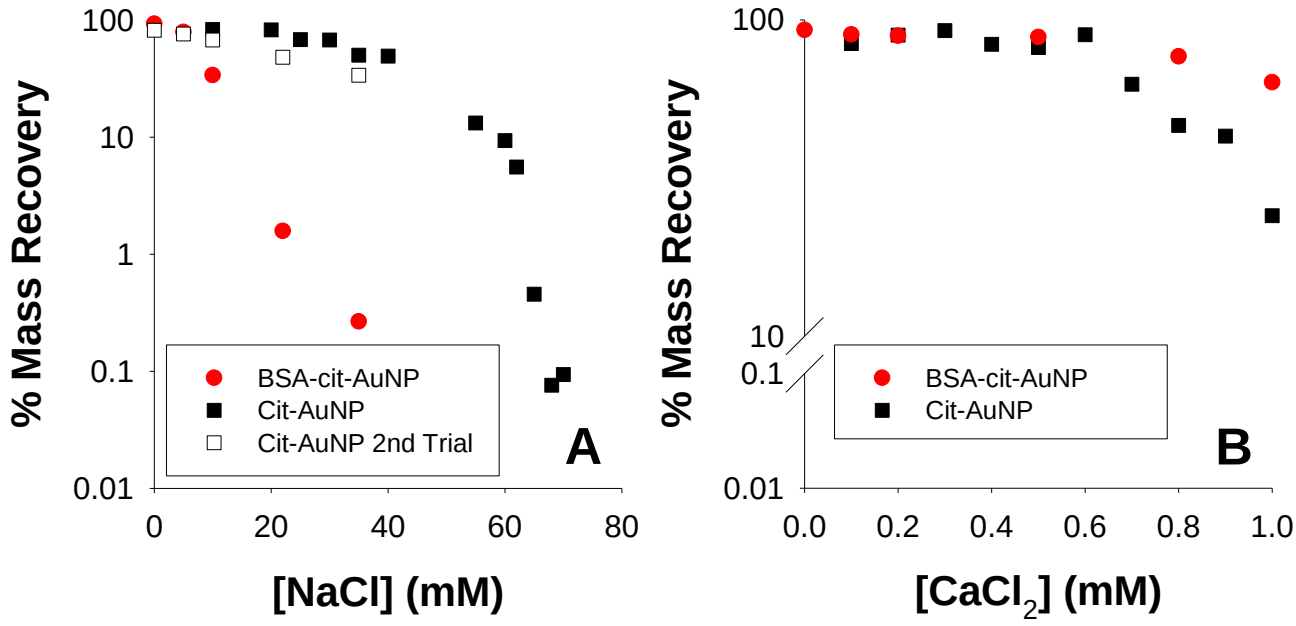

Figure 2-4 - Mass recovery of AuNP in the column effluent with increasing A) [NaCl] and B) [$CaCl_2$]. Results obtained by integrating the area beneath the breakthrough curves from the respective experiments. Note that the y-axis is in log-scale and an axis-break is included in panel B. Figure 3A includes replicate data obtained with cit-AuNP.

As shown in Figure 2-1 both the glass beads and the AuNPs had zeta potentials that approached 0 mV as salt concentration increased. Batch experiments indicated that BSA-cit-AuNP was more resistant to salt-mediated destabilization than cit-AuNP (Figure 2-2 and A-5 to A-7). That the opposite was observed in the BSA-cit-AuNP column experiment with NaCl was unexpected. One possible theory to explain this result is that in column experiments with BSA-cit-AuNP and NaCl the combined effect of the near neutral zeta potentials of both the nanoparticles and the glass beads overcame the electrosteric stabilization imparted by BSA, thus resulting in significant aggregation and/or deposition within the column. This interaction was not observed in the cit-AuNP column experiment with NaCl because the zeta potential of cit-AuNP was far from neutral under the experimental conditions. Lin *et al.* recently suggested that polymeric coatings are effective at protecting nanoparticles against homoaggregation destabilization.[50] However, in their deposition experiments, they observed similar trends as those discussed herein where

nanoparticles stable against homoaggregation readily deposited onto silica collectors.[50] They attributed this destabilization to the possibility that the thick polymer coatings prevented the double layer repulsive force from being effective because the interaction range between the nanoparticle surface and the collector surface was beyond the interaction range of the double layers.[50]

2.4.5 Nanoparticle Aggregation or Nanoparticle Deposition?

To more fully understand AuNP retention in the columns, the single-cell filtration attachment efficiency (α) was calculated as described in the SI.[51] The calculated α values reflect the ratio of AuNPs that attached to a glass bead after successful collision relative to the total collisions.[52,53] As shown in Figure 2-5, even though the ionic strengths for the $CaCl_2$ experiments were much lower than those used in the NaCl experiments they were still sufficient to result in α values that are of the same order of magnitude.

A common anomaly of the α values calculated for both cit-AuNP and BSA-cit-AuNP is that they are strikingly low given the observed AuNP retention. For example, in Figure 2-5A the data point for [NaCl] ≈70 mM gave an α value of ≈0.1. This result would suggest that 10% of the cit-AuNP that collided with the glass beads in the column remained attached and consequently were retained. However, upon comparison of this α value to the corresponding actual mass recovery one can see that in reality >90% of cit-AuNPs were retained for [NaCl] >60 mM. This discrepancy between the calculated α values and the actual retention of AuNP was observed across all of our collected data.

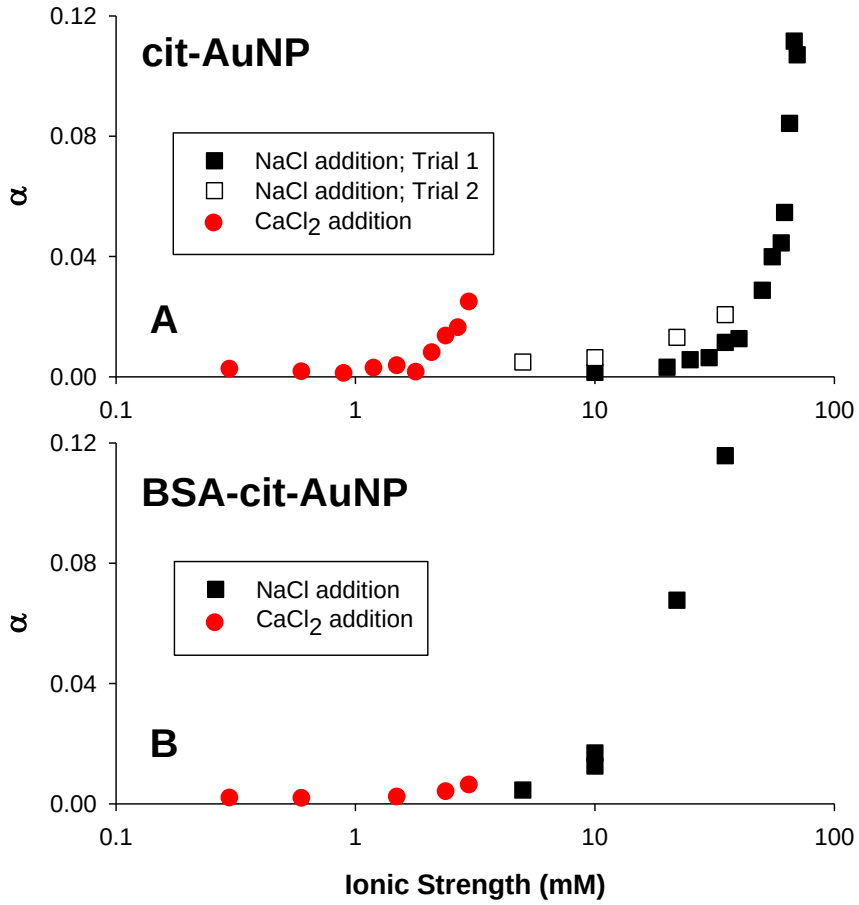

Figure 2-5 – Calculated attachment efficiencies (α) for A) cit-AuNP and B) BSA-cit-AuNP with increasing ionic strength.

In general, most column studies examining engineered nanoparticle deposition report α values that asymptotically approach 1.[41,42,54-59] The breakthrough curves reported in these papers typically exhibit low C/C_0 values at high ionic strengths. Under these conditions as C/C_0 approaches 0, α is expected to approach 1. Low mass recoveries were often observed herein, but the resulting α values were much lower than expected, and do not approach 1. A possible explanation for this discrepancy is nanoparticle aggregation within the column porespace.

Solovitch *et al.* reported α values of 0.04-0.09 when conducting column experiments using TiO_2 nanoparticles.[44] They attributed this to the fact that the α and η_0 calculations did not account for non-1-to-1 heterodeposition between a glass bead and a nanoparticle. Potential interactions not included in the

α calculations are nanoparticle aggregation within the porespace and column ripening. Our experimental data suggests that either one or both of these processes was occurring. As discussed in Appendix A (Figure A-10), batch experiments indicate that nanoparticle aggregation occurs more rapidly in the presence of the glass bead collector surface than in its absence. It is thus conceivable that large quantities of AuNP aggregated within the porespace and were retained either via physical straining or physicochemical attachment to the porous media. It is also possible, however, that collector ripening (i.e., the deposition of AuNP onto previously deposited AuNP) also occurs. If either or both processes were occurring, the very low α values are not erroneous, but rather only describe a limited portion of the processes occurring within the porespace.

2.4.6 Aggregation within the Column Porespace

Examining the temporal evolution of the UV-Vis spectra of AuNPs in the column effluent indicates that AuNP aggregation occurred within the porespace. Broadening of the LSPR band of the effluent UV-Vis spectra is the result of enhanced interactions between surface plasmons on the AuNPs.[60] In the presence of high [NaCl], slight broadening of the LSPR band was detected for cit-AuNP, while a substantial decrease in the 400-500 nm region of the spectrum was observed for BSA-cit-AuNP (as indicated by the arrows in Figures 2-2B-II and 2-2B-IV, respectively). As noted previously, at low [NaCl] both cit-AuNP and BSA-cit-AuNP were generally resistant to destabilization under low-salt conditions, while at higher [NaCl] cit-AuNP becomes destabilized yet BSA-cit-AuNP remained stable (Figures 2-2A-II & 2-2A-IV).

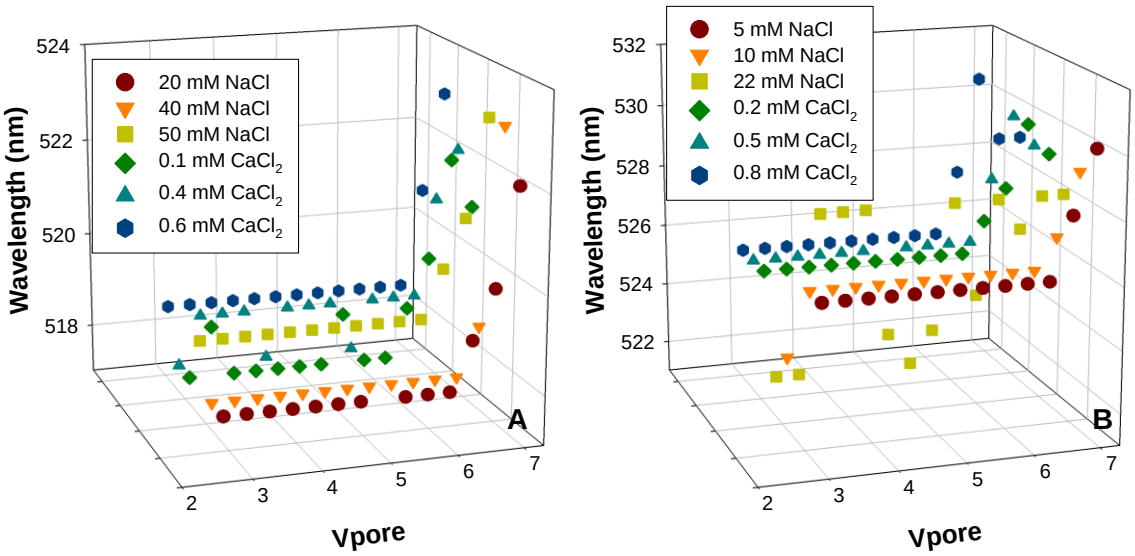

Figure 2-6 – LSPR shift during column experiments. A: cit-AuNP. B: BSA-cit-AuNP

In addition to these changes, there was a detectable elution-time dependent redshift in the LSPR band. As shown in Figure 6, redshifts from ≈518 to ≈523 nm were observed for cit-AuNP and redshifts from ≈525 to ≈530 nm were observed for BSA-cit-AuNP in the presence of both NaCl and $CaCl_2$. These redshifts are indicative of aggregated AuNPs and support our contention that aggregated nanoparticles were being transported in the effluent. DLVO calculations that further support this argument may be found in Appendix A. We note that aggregation that occurs in the porespace is not accounted for by colloid filtration theory and that this is a possible explanation for why the calculated α values failed to reflect our experimental observations.

We hypothesize that AuNP were induced to aggregate by their proximity to the silica surfaces and the progressive ripening of those surfaces. As AuNP deposits onto the surface of the glass beads, the silica surfaces are modified such that additional AuNPs interact with deposited AuNP rather than the silica surface. This ripening process occurs until sufficiently large AuNP aggregates break off of the bead surface and elute out of the column.

From an environmental perspective, it remains important for us to consider how surface modifications of nanoparticles affect their behavior when they are released into the environment. It has been shown

herein that nanoparticles that are coated with a thick protein layer can be more colloidally stable than nanoparticles that lack such a layer under a batch conditions. The assumption that such behavior can be expected within porous media has been shown by this effort to be dubious. Our work has shown that protein coated nanomaterials interact with porous media surfaces and aggregate in a way that is not predicted by batch experiments. The fate of non-specifically functionalized nanomaterials in the environment should thus be carefully evaluated on a case by case basis.

Disclosure

This work has been published by the American Chemical Society: Chan, M. Y.; Vikesland, P. J., Porous Media-Induced Aggregation of Protein-Stabilized Gold Nanoparticles. *Environ. Sci. Technol.* **2014,** *48*, (3), 1532-1540.

Supporting Information

All supporting information cited in this chapter is located in Appendix A.

References

1. Johnson, D. R.; Methner, M. M.; Kennedy, A. J.; Steevens, J. A., Potential for Occupational Exposure to Engineered Carbon-Based Nanomaterials in Environmental Laboratory Studies. *Environ. Health Perspect.* **2010,** *118*, (1), 49-54.

2. Ferry, J. L.; Craig, P.; Hexel, C.; Sisco, P.; Frey, R.; Pennington, P. L.; Fulton, M. H.; Scott, I. G.; Decho, A. W.; Kashiwada, S.; Murphy, C. J.; Shaw, T. J., Transfer of gold nanoparticles from the water column to the estuarine food web. *Nat. Nanotechonol.* **2009,** *4*, (7), 441-444.

3. Judy, J. D.; Unrine, J. M.; Bertsch, P. M., Evidence for Biomagnification of Gold Nanoparticles within a Terrestrial Food Chain. *Environ. Sci. Technol.* **2011,** *45*, (2), 776-781.

4. Turkevich, J.; Stevenson, P. C.; Hillier, J., A study of the nucleation and growth processes in the synthesis of colloidal gold. *Discuss. Faraday Soc.* **1951,** *11*, 55-75.

5. Ji, X.; Song, X.; Li, J.; Bai, Y.; Yang, W.; Peng, X., Size Control of Gold Nanocrystals in Citrate Reduction: The Third Role of Citrate. *J. Am. Chem. Soc.* **2007,** *129*, (45), 13939-13948.

6. Phenrat, T.; Cihan, A.; Kim, H.-J.; Mital, M.; Illangasekare, T.; Lowry, G. V., Transport and Deposition of Polymer-Modified Fe0 Nanoparticles in 2-D Heterogeneous Porous Media: Effects of Particle Concentration, Fe0 Content, and Coatings. *Environ. Sci. Technol.* **2010,** *44*, (23), 9086-9093.

7. Cumberland, S. A.; Lead, J. R., Synthesis of NOM-Capped Silver Nanoparticles: Size, Morphology, Stability, and NOM Binding Characteristics. *ACS Sustainable Chem. Eng.* **2013,** *1*, (7), 817-825.

8. Stankus, D. P.; Lohse, S. E.; Hutchison, J. E.; Nason, J. A., Interactions between Natural Organic Matter and Gold Nanoparticles Stabilized with Different Organic Capping Agents. *Environ. Sci. Technol.* **2011,** *45*, (8), 3238-3244.

9. Felix, L. C.; Ortega, V. A.; Ede, J. D.; Goss, G. G., Physicochemical Characteristics of Polymer-Coated Metal-Oxide Nanoparticles and their Toxicological Effects on Zebrafish (Danio rerio) Development. *Environ. Sci. Technol.* **2013,** *47*, (12), 6589-6596.

10. Liu, Y.; Shipton, M. K.; Ryan, J.; Kaufman, E. D.; Franzen, S.; Feldheim, D. L., Synthesis, Stability, and Cellular Internalization of Gold Nanoparticles Containing Mixed Peptide−Poly(ethylene glycol) Monolayers. *Anal. Chem.* **2007,** *79*, (6), 2221-2229.

11. Housni, A.; Ahmed, M.; Liu, S.; Narain, R., Monodisperse Protein Stabilized Gold Nanoparticles via a Simple Photochemical Process. *J. Phys. Chem. C* **2008,** *112*, (32), 12282-12290.

12. Phenrat, T.; Song, J. E.; Cisneros, C. M.; Schoenfelder, D. P.; Tilton, R. D.; Lowry, G. V., Estimating Attachment of Nano- and Submicrometer-particles Coated with Organic Macromolecules in Porous Media: Development of an Empirical Model. *Environ. Sci. Technol.* **2010,** *44*, (12), 4531-4538.

13. Shukla, R.; Bansal, V.; Chaudhary, M.; Basu, A.; Bhonde, R. R.; Sastry, M., Biocompatibility of Gold Nanoparticles and Their Endocytotic Fate Inside the Cellular Compartment: A Microscopic Overview. *Langmuir* **2005,** *21*, (23), 10644-10654.

14. Brewer, S. H.; Glomm, W. R.; Johnson, M. C.; Knag, M. K.; Franzen, S., Probing BSA Binding to Citrate-Coated Gold Nanoparticles and Surfaces. *Langmuir* **2005,** *21*, (20), 9303-9307.

15. Peters Jr, T., Serum Albumin. In *Advances in Protein Chemistry*, Academic Press: Orlando, Florida, 1985; Vol. 37, pp 161-164.

16. Bischel, H. N.; MacManus-Spencer, L. A.; Zhang, C.; Luthy, R. G., Strong associations of short-chain perfluoroalkyl acids with serum albumin and investigation of binding mechanisms. *Environ. Toxicol. Chem.* **2011,** *30*, (11), 2423-2430.

17. Valle-Delgado, J. J.; Molina-Bolívar, J. A.; Galisteo-González, F.; Gálvez-Ruiz, M. J.; Feiler, A.; Rutland, M. W., Interaction Forces between BSA Layers Adsorbed on Silica Surfaces Measured with an Atomic Force Microscope. *J. Phys. Chem. B* **2004,** *108*, (17), 5365-5371.

18. Dominguez-Medina, S.; McDonough, S.; Swanglap, P.; Landes, C. F.; Link, S., In Situ Measurement of Bovine Serum Albumin Interaction with Gold Nanospheres. *Langmuir* **2012,** *28*, (24), 9131-9139.

19. Dominguez-Medina, S.; Blankenburg, J.; Olson, J.; Landes, C. F.; Link, S., Adsorption of a Protein Monolayer via Hydrophobic Interactions Prevents Nanoparticle Aggregation under Harsh Environmental Conditions. *ACS Sustainable Chem. Eng.* **2013,** *1*, (7), 833-842.

20. Sridhar, M. K. C.; Pillai, S. C., Proteins in Wastewater and Wastewater Sludges. *Journal (Water Pollution Control Federation)* **1973,** *45*, (7), 1595-1600.

21. Tejamaya, M.; Römer, I.; Merrifield, R. C.; Lead, J. R., Stability of Citrate, PVP, and PEG Coated Silver Nanoparticles in Ecotoxicology Media. *Environ. Sci. Technol.* **2012,** *46*, (13), 7011-7017.

22. Saleh, N. B.; Pfefferle, L. D.; Elimelech, M., Influence of Biomacromolecules and Humic Acid on the Aggregation Kinetics of Single-Walled Carbon Nanotubes. *Environ. Sci. Technol.* **2010,** *44*, (7), 2412-2418.

23. Tufenkji, N.; Miller, G. F.; Ryan, J. N.; Harvey, R. W.; Elimelech, M., Transport of Cryptosporidium Oocysts in Porous Media: Role of Straining and Physicochemical Filtration†. *Environ. Sci. Technol.* **2004,** *38*, (22), 5932-5938.

24. Delgado, A. V.; González-Caballero, F.; Hunter, R. J.; Koopal, L. K.; Lyklema, J., Measurement and interpretation of electrokinetic phenomena. *J. Colloid Interface Sci.* **2007,** *309*, (2), 194-224.

25. Henry, D. C., The Cataphoresis of Suspended Particles. Part I. The Equation of Cataphoresis. *Proc. R. Soc. Lond. A* **1931,** *133*, (821), 106-129.

26. Henry, D. C., The electrophoresis of suspended particles. IV. The surface conductivity effect. *Trans. Faraday Soc.* **1948,** *44*, 1021-1026.

27. Ao, L.-M.; Gao, F.; Pan, B.-F.; Cui, D.-X.; Gu, H.-C., Interaction between Gold Nanoparticles and Bovine Serum Albumin or Sheep Antirabbit Immunoglobulin G. *Chin. J. Chem.* **2006,** *24*, (2), 253-256.

28. Eaton, A. D.; Clesceri, L. S.; Rice, E. W.; Greenberg, A. E.; Franson, M. A. H., *Standard Methods for the Examination of Water & Wastewater: Centennial Edition*. 21 Har/Cdr ed.; Amer Public Health Assn: 2005.

29. Mwh, *Water Treatment: Principles and Design*. 2 ed.; Wiley: 2005; p 1968.

30. Krishnan, K.; Guha, A., The absorption spectra of nitrates and nitrities in relation to their photo-dissociation. *P. Math. Sci.* **1934,** *1*, (4), 242-249.

31. Dobrovolskaia, M. A.; Patri, A. K.; Zheng, J.; Clogston, J. D.; Ayub, N.; Aggarwal, P.; Neun, B. W.; Hall, J. B.; McNeil, S. E., Interaction of colloidal gold nanoparticles with human blood: effects on

particle size and analysis of plasma protein binding profiles. *Nanomed.-Nanotechnol. Biol. Med.* **2009,** *5*, (2), 106-117.

32. Kohli, I.; Alam, S.; Patel, B.; Mukhopadhyay, A., Interaction and diffusion of gold nanoparticles in bovine serum albumin solutions. *Appl. Phys. Lett.* **2013,** *102*, (20), 203705-203705-4.

33. Smoluchowski, M., Contributiona la théorie de l'endosmose électrique et de quelques phenomenes corrélatifs. *Bull. Intl Acad. Sci. Cracovie* **1903,** *8*, 182-200.

34. Rezwan, K.; Meier, L. P.; Rezwan, M.; Vörös, J.; Textor, M.; Gauckler, L. J., Bovine Serum Albumin Adsorption onto Colloidal Al2O3 Particles: A New Model Based on Zeta Potential and UV−Vis Measurements. *Langmuir* **2004,** *20*, (23), 10055-10061.

35. Rezwan, K.; Studart, A. R.; Vörös, J.; Gauckler, L. J., Change of ζ Potential of Biocompatible Colloidal Oxide Particles upon Adsorption of Bovine Serum Albumin and Lysozyme. *J. Phys. Chem. B* **2005,** *109*, (30), 14469-14474.

36. Hardy, W. B., A Preliminary Investigation of the Conditions which Determine the Stablity of Irreversible Hydrosols. *J. Phys. Chem.* **1900,** *4*, (4), 235-253.

37. Schulze, H., Schwefelarsen in wässriger Lösung. *J. Prakt. Chem.* **1882,** *25*, (1), 431-452.

38. Revil, A.; Pezard, P. A.; Glover, P. W. J., Streaming potential in porous media: 1. Theory of the zeta potential. *J. Geophys. Res.* **1999,** *104*, (B9), 20021-20031.

39. Zook, J. M.; Rastogi, V.; MacCuspie, R. I.; Keene, A. M.; Fagan, J., Measuring Agglomerate Size Distribution and Dependence of Localized Surface Plasmon Resonance Absorbance on Gold Nanoparticle Agglomerate Size Using Analytical Ultracentrifugation. *ACS Nano* **2011,** *5*, (10), 8070-8079.

40. Petosa, A. R.; Jaisi, D. P.; Quevedo, I. R.; Elimelech, M.; Tufenkji, N., Aggregation and Deposition of Engineered Nanomaterials in Aquatic Environments: Role of Physicochemical Interactions. *Environ. Sci. Technol.* **2010,** *44*, (17), 6532-6549.

41. Elimelech, M.; O'Melia, C. R., Kinetics of deposition of colloidal particles in porous media. *Environ. Sci. Technol.* **1990,** *24*, (10), 1528-1536.

42. Espinasse, B.; Hotze, E. M.; Wiesner, M. R., Transport and Retention of Colloidal Aggregates of C60 in Porous Media: Effects of Organic Macromolecules, Ionic Composition, and Preparation Method. *Environ. Sci. Technol.* **2007,** *41*, (21), 7396-7402.

43. Li, Y.; Wang, Y.; Pennell, K. D.; Abriola, L. M., Investigation of the Transport and Deposition of Fullerene (C60) Nanoparticles in Quartz Sands under Varying Flow Conditions. *Environ. Sci. Technol.* **2008,** *42*, (19), 7174-7180.

44. Solovitch, N.; Labille, J. r. m.; Rose, J. r. m.; Chaurand, P.; Borschneck, D.; Wiesner, M. R.; Bottero, J.-Y., Concurrent Aggregation and Deposition of TiO2 Nanoparticles in a Sandy Porous Media. *Environ. Sci. Technol.* **2010,** *44*, (13), 4897-4902.

45. Wang, Y.; Li, Y.; Fortner, J. D.; Hughes, J. B.; Abriola, L. M.; Pennell, K. D., Transport and Retention of Nanoscale C60 Aggregates in Water-Saturated Porous Media. *Environ. Sci. Technol.* **2008,** *42*, (10), 3588-3594.

46. Lin, S.; Cheng, Y.; Bobcombe, Y.; L. Jones, K.; Liu, J.; Wiesner, M. R., Deposition of Silver Nanoparticles in Geochemically Heterogeneous Porous Media: Predicting Affinity from Surface Composition Analysis. *Environ. Sci. Technol.* **2011,** *45*, (12), 5209-5215.

47. Liu, D.; Johnson, P. R.; Elimelech, M., Colloid Deposition Dynamics in Flow-Through Porous Media: Role of Electrolyte Concentration. *Environ. Sci. Technol.* **1995,** *29*, (12), 2963-2973.

48. Tiraferri, A.; Sethi, R., Enhanced transport of zerovalent iron nanoparticles in saturated porous media by guar gum. *J. Nanopart. Res.* **2009,** *11*, (3), 635-645.

49. Chen, G.; Liu, X.; Su, C., Transport and Retention of TiO2 Rutile Nanoparticles in Saturated Porous Media under Low-Ionic-Strength Conditions: Measurements and Mechanisms. *Langmuir* **2011,** *27*, (9), 5393-5402.

50. Lin, S.; Cheng, Y.; Liu, J.; Wiesner, M. R., Polymeric Coatings on Silver Nanoparticles Hinder Autoaggregation but Enhance Attachment to Uncoated Surfaces. *Langmuir* **2012,** *28*, (9), 4178-4186.

51. Yao, K.-M.; Habibian, M. T.; O'Melia, C. R., Water and waste water filtration. Concepts and applications. *Environ. Sci. Technol.* **1971,** *5*, (11), 1105-1112.

52. Elimelech, M., Effect of Particle Size on the Kinetics of Particle Deposition under Attractive Double Layer Interactions. *J. Colloid Interface Sci.* **1994,** *164*, (1), 190-199.

53. Lecoanet, H. F.; Bottero, J.-Y.; Wiesner, M. R., Laboratory Assessment of the Mobility of Nanomaterials in Porous Media. *Environ. Sci. Technol.* **2004,** *38*, (19), 5164-5169.

54. Franchi, A.; O'Melia, C. R., Effects of Natural Organic Matter and Solution Chemistry on the Deposition and Reentrainment of Colloids in Porous Media. *Environ. Sci. Technol.* **2003,** *37*, (6), 1122-1129.

55. Jaisi, D. P.; Elimelech, M., Single-Walled Carbon Nanotubes Exhibit Limited Transport in Soil Columns. *Environ. Sci. Technol.* **2009,** *43*, (24), 9161-9166.

56. Liu, X.; Wazne, M.; Christodoulatos, C.; Jasinkiewicz, K. L., Aggregation and deposition behavior of boron nanoparticles in porous media. *J. Colloid Interface Sci.* **2009,** *330*, (1), 90-96.

57. Pelley, A. J.; Tufenkji, N., Effect of particle size and natural organic matter on the migration of nano- and microscale latex particles in saturated porous media. *J. Colloid Interface Sci.* **2008,** *321*, (1), 74-83.

58. Saleh, N.; Kim, H.-J.; Phenrat, T.; Matyjaszewski, K.; Tilton, R. D.; Lowry, G. V., Ionic Strength and Composition Affect the Mobility of Surface-Modified Fe0 Nanoparticles in Water-Saturated Sand Columns. *Environ. Sci. Technol.* **2008,** *42*, (9), 3349-3355.

59. Tufenkji, N.; Elimelech, M., Breakdown of Colloid Filtration Theory: Role of the Secondary Energy Minimum and Surface Charge Heterogeneities. *Langmuir* **2005,** *21*, (3), 841-852.

60. Khlebtsov, N. G.; Dykman, L. A.; Krasnov, Y. M.; Mel'nikov, A. G., Light absorption by the clusters of colloidal gold and silver particles formed during slow and fast aggregation. *Colloid Journal* **2000,** *62*, (6), 765-779.

Chapter 3. Surface-Enhanced Raman Spectroscopy Characterization of Salt Induced Gold Nanoparticle Aggregation

Matthew Y. Chan, Weinan Leng, and Peter J. Vikesland

The Charles E. Via, Jr. Department of Civil and Environmental Engineering, Virginia Tech, Blacksburg, VA, USA.

Institute for Critical Technology and Applied Science, Virginia Tech, Blacksburg, VA, USA.

NSF-EPA Center for the Environmental Implications of Nanotechnology, Duke University, Durham, NC, USA

3.1 Abstract

Low frequency (<300 cm^{-1}) vibrational interactions between gold surfaces and dissolved halides in water were investigated by surface enhanced Raman spectroscopy (SERS). Experiments with NaF, NaCl, NaBr, and NaI salts indicate that the Raman shift of the Au-X^- SERS band is correlated with the bond-strength of the corresponding covalent interaction. These low frequency SERS bands open up new methods to investigate the behavior of nanoparticle-halide interactions in aqueous environments.

3.2 Background

Herein we illustrate that the aggregation of gold nanoparticles can be studied by surface enhanced Raman spectroscopy (SERS). Raman spectroscopy detects inelastically scattered photons that result from induced dipole interactions.[1] Only a very small fraction of the incident photons are scattered inelastically, thus leading to characteristically weak Raman signals.[2] Although elemental gold inelastically scatters incident photons and is thus Raman active, the resulting signal is generally too low to be detectable under typical laser intensities and acquisition times. Halides such as F^-, Cl^-, Br^-, and I^- undergo strong interactions with the gold surface.[3] These electron rich interactions exhibit large Raman cross-sections and their proximity to an optical enhancer (a roughened or nanoparticulate gold, or AuNP, surface) produces a strong Raman signal.[4] To date, due to instrument limitations, there have been only limited studies examining the SERS activity of Au-X^- (where X^- is a halide) interactions because they give rise to Raman bands with low wavenumber (<300 cm^{-1}) vibrational modes.[5] However, this low frequency range contains valuable information about the relative bond-energies of halide-metal interactions.[4-6] Noble metal nanoparticles enhance vibrational Raman bands due to surface plasmon effects.[7] Individual AuNPs generally provide negligible enhancement. However, as shown herein, nanoparticle aggregation induced by salt addition enables electromagnetic coupling within AuNP aggregates that gives rise to nano-structural 'hotspots' that exhibit higher SERS enhancements than individual nanoparticles.[8,9]

3.3 Methods, Results, and Discussions

We first utilized SERS to characterize the interaction between gold and dissolved aqueous halides. 2D scans of NaX droplets on a commercial gold SERS substrate (Klarite®) were collected as described in Appendix B. Briefly, aliquots of NaX salts (X = F, Cl, Br, I) were deposited and dried on the surface of Klarite®, and a confocal Raman spectrometer was then rastered across the substrate to produce a 2D map. Maps obtained for a series of NaX salts illustrate that the Au-X^- interactions are readily detectible via SERS (Figure 3-1A). We note that solution phase Au-X^- interactions do not generate sufficient signal for them to be detectable by conventional Raman spectroscopy. The Raman signal intensity is proportional to the scattering path length, and for surface interactions, such path lengths are generally very short, resulting in a 10^5-fold signal loss relative to bulk samples.[10] The SERS substrate not only provides a gold surface that the halogen ions interact with, but is also crucial because it provides the signal enhancement required to detect Au-X^- interactions. Additional salt addition studies were conducted, but instead involved the use of citrate-coated gold nanoparticle (cit-AuNP) suspensions. The 15 nm diameter AuNP employed does not give rise to an intense SERS signal due to the lack of overlap between the localized surface plasmon resonance (LSPR) band and the 785 nm laser used; however, when the AuNPs aggregate and the LSPR band redshifts toward the incident laser wavelength due to plasmon-plasmon interactions the SERS signal intensity increases. Detailed experimental procedures and characterization data for cit-AuNP is presented in Appendix B.

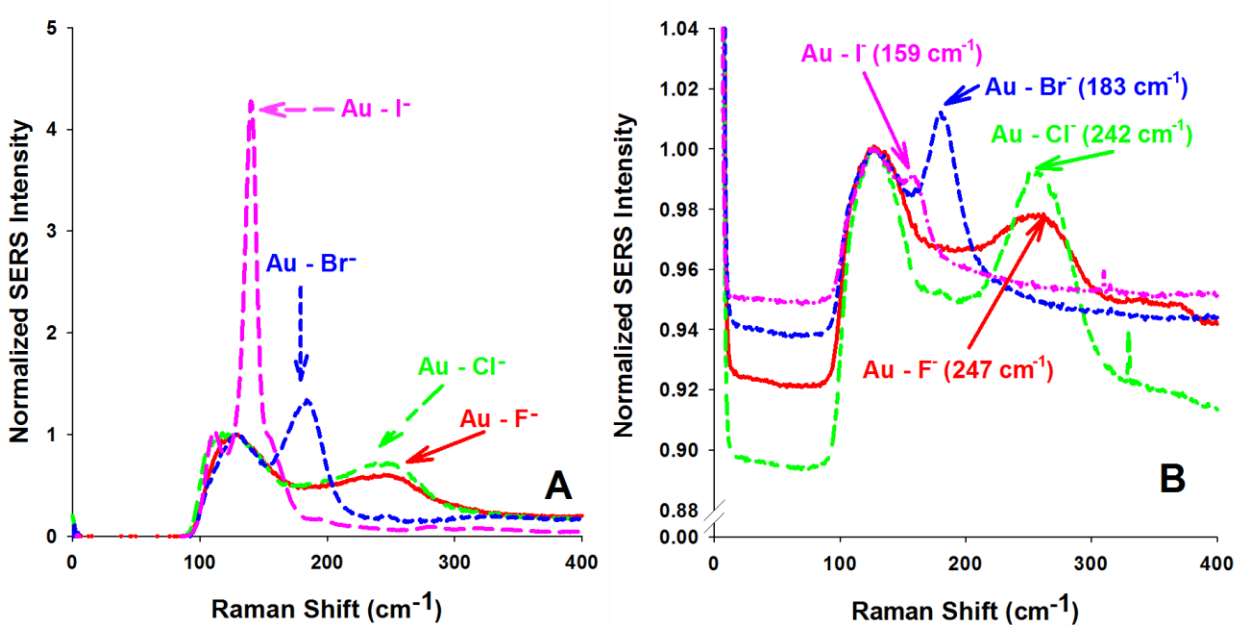

Figure 3-1 – **A**: SERS spectra of Au-X^- gold surface interactions. This experiment was performed using 1 mM NaX solutions. **B**: SERS spectra of cit-AuNP interacting with 10 mM of NaX. Spectra normalized to peak at ≈ 130 cm^{-1} for visibility.

As illustrated in Figure 3-1, each test halide exhibited a unique Au-X^- Raman band both for the experiments conducted with the SERS substrate as well as with cit-AuNP. The exact origin of these low-frequency Raman bands is the subject of debate. Gao & Weaver conducted experiments with a roughened gold electrode and dissolved halides. In their experiments, a range of voltages were applied to the gold electrode and the interactions between the roughened electrode and the halides were observed via SERS. The locations of each Au-X^- SERS band are presented in Table 3-1 for our experiments with Klarite® and cit-AuNP and can be compared with the open circuit potential results of Gao & Weaver. Our experimental results are highly similar to those of Gao & Weaver, thus suggesting that we observed the same phenomenon.

Table 3-1 Comparison of Au-X^- SERS band location with Gao & Weaver.[5] All values in cm^{-1}.

	Klarite® Substrate	Cit-AuNP	Gao & Weaver[5,[a]]
Au-F^-	252	247	n/a
Au-Cl^-	249	242	258
Au-Br^-	181	183	184
Au-I^-	140	159	158

[a] Gao & Weaver conducted Au-X experiments on an electrode. SERS shift location was dependent on applied voltage. Reported values are at open circuit potential.

The locations of the Au-X^- SERS bands for Klarite® and the cit-AuNP experiments were consistent, thus indicating that the SERS bands obtained using aggregated cit-AuNP arose from a halide gold-surface interaction that became detectable due to aggregation induced surface enhancement. In contrast, for the experiments performed with Klarite®, the enhancement originates from the nanoscale features of the substrate.[11] In the experiments involving cit-AuNP, however, the particles must aggregate to form SERS 'hotspots' that provide a signal enhancement (Figure 3-2A).[8] Salt-induced aggregation of cit-AuNPs led to a time-dependent increase in the Au-Cl^- SERS band at ≈250 cm^{-1}. The increased intensity of this band over time provides an indication of both the rate of SERS hot-spot formation as well as the rate at which chloride associates with the gold surface. Under the conditions of this study cit-AuNP are negatively charged (pH ≈ 3.2, electrophoretic mobility ≈ -3.0 $\mu m \cdot cm \cdot V^{-1} \cdot s^{-1}$) and thus nanoparticle aggregation is induced due to the destabilizing effects of cation addition, and more specifically sodium (Na^+) ion addition. As cit-AuNP aggregates, hot spots form between adjacent nanoparticles and the association of the anion with the surface becomes apparent. Similar time-dependent spectra for F^-, Br^-, and I^- illustrate the generality of this trend (data not shown).

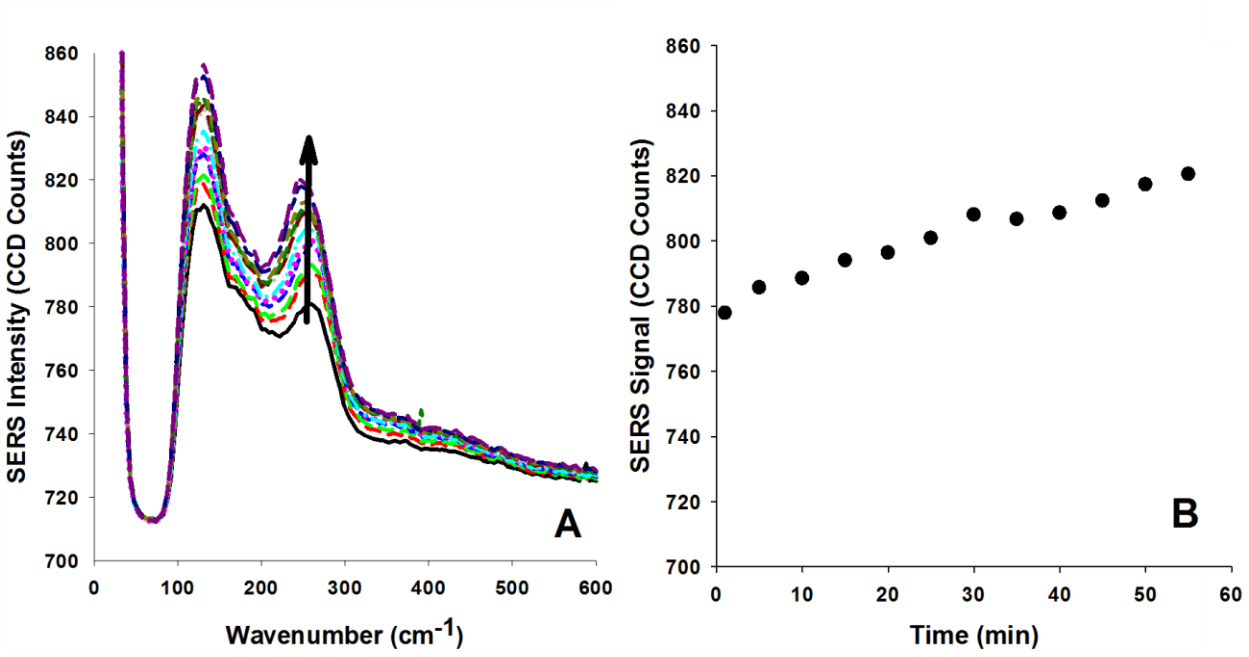

Figure 3-2 – **A**: SERS spectra of cit-AuNP in the presence of 10 mM NaCl. Au-Cl^- SERS band located at ≈ 240 cm^{-1}; arrow indicates time progression where each spectrum is obtained at a 5-minute interval, and **B**: Time-resolved Au-Cl^- SERS band intensity of the same experiments.

Our data show that the gold-halide SERS bands increases in intensity as aggregation proceeds, and that each SERS vibrational mode is distinct depending on the identity of the halide. These combined properties of the SERS bands may enable their application in characterizing the kinetics of AuNP aggregation as well as the interaction between the AuNP aggregate surface and aqueous halides. Past work by Loo investigating the physicochemical nature of these SERS bands suggested that halides form coordination complexes with the Au^0 surface that lead to gold dissolution, the formation of Au^+, and production of Raman active vibrational modes.[12] The complexes formed by adding halides to gold are expected to be the linear complex Au^IX^{2-} or the planar complex $Au^{III}X^{4-}$. Loo used a roughened gold electrode that was exposed to halide solution while applying a voltage and observed numerous low frequency (≈150-350 cm^{-1}) Raman bands

that they assigned to the $Au^{I}X^{2-}$ stretch and the planar deformation of $Au^{III}X^{4-}$. The SERS bands for the gold halide complexes as reported by Loo were not observed either by Gao & Weaver or herein. Our results and those of Gao & Weaver suggest that the low-frequency SERS bands are the result of the direct interaction between the halides themselves and the gold surface and do not require formation of dissolved gold complexes. Experiments conducted with dissolved $HAuCl_4$ solution control corroborates this (see Appendix B).

While the Au-X^- SERS band locations for Au-Cl^-, Au-Br^-, and Au-I^- are comparable to those reported by Gao & Weaver, to our knowledge, the location of the Au-F^- band at ≈247 cm^{-1} has not previously been reported. Assigning Raman and SERS bands for experiments involving surface interfacial interactions can be challenging.[13] However, for each halide experiment using either Klarite® or cit-AuNP there was only one variable SERS band that emerged when the halide identity was altered. The location of the Au-X^- band moves closer towards the Rayleigh line (at 0 cm^{-1}) as the halide identity was changed downward within Group 17 of the periodic table. The frequencies of these Au-X^- SERS bands depend on the mass of the vibrating bond (≈ the mass of the halide) and the force constant of the interaction.[5] As the halide identity moves down within Group 17 (from fluorine to iodine), the interaction between the halide and the gold surface becomes more "covalent" than "ionic" and this manifests as an increase in force constant. The nature of the Au-X^- interaction was previously studied by thermal desorption measurements that indicate that the gas phase binding strength of the gold–halogen bond follows the order Cl > Br > I.[14] The implication of this trend is that when halogen atoms adsorb to the metal surface that a charge transfer interaction between the metal surface and the halogen atom occurs. The strength of this interaction is correlated with the binding strength (Cl > Br > I), where the metal surface adsorbent exhibits a localized positive charge with a corresponding strength due to the charge transfer

interaction. This "ionic" interaction is strongest for Cl, followed by Br and I. Based on this trend, the "covalency" of Au-I^- is expected to be greatest, with Au-Br^-, and Au-Cl^- weaker in succession.[5] The general simplified relationship between Raman shift frequency and force constant is described as[5]:

$$f_{M-X} = 4\pi^2 \nu_{M-X}^2 c^2 \mu$$

Where f_{M-X} is the force constant for a given Au-X^- interaction in dyn/cm, ν_{M-X} is the Raman shift frequency for the interaction in wavenumbers, c is the velocity of light, and μ is the effective reduced mass of the vibrating interaction (taken to be the mass of the halide herein).[5,15-18] Force constants for our experiments involving Klarite® and cit-AuNP were calculated (Table 3-2). μ increases as X^- moves down Group 17 and the calculated f_{M-X} increases because the interaction becomes more "covalent" and less "ionic", and as such ν_{M-X} reflects the dynamics between increasing mass and force constant. The decreasing trend of ν_{M-X} as we move down Group 17, resulted in the aforementioned increasing trend of the force constants of Au-X^- interaction, which is consistent with our hypothesis of the covalent-ionic dynamics and characteristic of these interactions. The force constants calculated for our SERS experiments follow the trend $f_{Au-F} < f_{Au-Cl} < f_{Au-Br} < f_{Au-I}$. We note that this trend is opposite that observed for the force constants of bulk solid AuX_x salts (Table 3-2). Gao & Weaver obtained similar values for Au-Cl^-, Au-Br^-, and Au-I^- and explained the observed trend to the aforementioned covalency versus charge transfer dynamics for adsorbed specie, especially when compared to bulk salts for which ionic interactions dominate. The observed force constant trend supports the notion that Au-X^- interactions reflect adsorbate-surface interactions.[5]

We are not aware of prior studies that have characterized the strength of the Au-F^- interaction. Assuming that fluoride follows the previously described trend in the strength of the charge transfer interaction (F > Cl > Br > I) it should exhibit a SERS Au-F^- band at a wavenumber greater than the SERS Au-Cl^- band, which is what we experimentally observed (Table 3-1). It is understood that fluorine exhibits strong electronegativity (stronger than all other halogens) and therefore its ion should exhibit the strongest ionic interaction as compared to other halides. Based on our reasoning, a strong ionic interaction between gold and F^- would lead to weak covalency of that interaction, resulting in a lower force constant, which is what was experimentally observed. We note that the charge-transfer interactions trend mirrors that of the observed signal intensities; however, for Klarite® this trend could have been an artifact associated with how the salt solution dried on the substrate. The fact that similar SERS intensity trends were observed in the cit-AuNP experiments indicates this to not be the case.

Table 3-2 – Comparison of Au-X^- force constants with Gao & Weaver reported values; all values in units of 10^5 dyn/cm.

	Klarite®	Cit-AuNP	Gao & Weaver	Bulk solid AuX_x[16]
Au-F^-	0.72	0.69	n/a	n/a
Au-Cl^-	1.30	1.23	1.39	1.75
Au-Br^-	1.51	1.54	1.59	1.63
Au-I^-	1.46	1.88	1.87	1.22

We note that a characteristic Raman band at ≈130 cm^{-1} was detected in all experiments where a SERS enhancement was observed (Figure 3-1). Previous studies generally do not report this peak. Although Loo reported Raman bands for gold complexes that are in the vicinity of this

characteristic peak, we found that its location did not change with halide identity and we thus rule out the possibility that gold complexes are the origin of this band. Other possible origins for this peak include citrate-gold interactions, or bonds within the citrate molecule that are enhanced by SERS effects. Neither of these origins are probable because such interactions generally give rise to Raman shift frequencies above 1000 cm^{-1} and not the low frequency mode observed.[19] While there are reports of detectable Raman shifts for gold-gold interactions within a crystalline structure, including possible plasmon-phonon interactions, these Raman shifts generally occur at even lower frequency – generally below 75 cm^{-1} and possibly below 1.0 cm^{-1}.[20-22] Regardless of its origin, in the cit-AuNP experiments this characteristic peak was only observed when sufficient aggregation had occurred to provide a SERS enhancement. Experiments to determine the nature of this peak are ongoing elsewhere in the *Vikesland* group.

While Au-X^- SERS bands have been previously observed on a macroscopic gold surface, to date they had not been investigated using aggregated AuNPs in suspension. We illustrate that Au-X^- SERS bands become observable when halides are introduced into AuNP suspension. Importantly, while Au-X^- SERS bands are conditionally observable only when particle aggregation leads to SERS hotspots formation, we were able to detect the Au-X signal at a concentration of 10 mM of NaCl. This is a value well below the critical coagulation concentration of similarly sized cit-AuNP.[23] These low frequency SERS bands between gold and halides open up new methods of investigating the behavior of AuNPs in aqueous environments via SERS.

Disclosure

This work is being prepared as a manuscript to be submitted to the German Chemical Society for consideration to be published as a Communication in the journal *Angewandt Chemie International Edition*.

Supporting Information

All supporting information cited in this chapter is located in Appendix B.

References

1. Pelletier, M. J., *Analytical Applications of Raman Spectroscopy*. 1 edition ed.; Blackwell Publishing: Osney Mead, Oxford ; Malden, MA, 1999; p 496.

2. Long, D. A., *Raman spectroscopy*. McGraw-Hill International Book Company: London, 1977.

3. Cotton, F. A.; Wilkinson, G.; Murillo, C. A.; Bochmann, M., *Advanced Inorganic Chemistry*. 6 edition ed.; Wiley-Interscience: New York, 1999; p 1376.

4. Alvarez-Puebla, R. A.; Liz-Marzán, L. M., SERS Detection of Small Inorganic Molecules and Ions. *Angew. Chem.-Int. Edit.* **2012,** *51*, (45), 11214-11223.

5. Gao, P.; Weaver, M. J., Metal-adsorbate vibrational frequencies as a probe of surface bonding: halides and pseudohalides at gold electrodes. *J. Phys. Chem.* **1986,** *90*, (17), 4057-4063.

6. Loo, B. H., In situ identification of halide complexes on gold electrode by surface-enhanced Raman spectroscopy. *J. Phys. Chem.* **1982,** *86*, (4), 433-437.

7. Smith, E.; Dent, G., *Modern Raman Spectroscopy: A Practical Approach*. John Wiley & Sons: 2013; p 216.

8. Blatchford, C. G.; Campbell, J. R.; Creighton, J. A., Plasma resonance—enhanced Raman scattering by absorbates on gold colloids: the effects of aggregation. *Surf. Sci.* **1982,** *120*, (2), 435-455.

9. Creighton, J. A.; Blatchford, C. G.; Albrecht, M. G., Plasma resonance enhancement of Raman scattering by pyridine adsorbed on silver or gold sol particles of size comparable to the excitation wavelength. *J. Chem. Soc. Faraday II* **1979,** *75*, 790.

10. McCreery, R. L., Raman Spectroscopy of Surfaces. In *Raman Spectroscopy for Chemical Analysis*, John Wiley & Sons, Inc.: 2000; pp 373-413.

11. Perney, N. M. B.; Baumberg, J. J.; Zoorob, M. E.; Charlton, M. D. B.; Mahnkopf, S.; Netti, C. M., Tuning localized plasmons in nanostructured substrates for surface-enhanced Raman scattering. *Opt. Express* **2006,** *14*, (2), 847-857.

12. Gaur, J. N.; Schmid, G. M., Electrochemical behavior of gold in acidic chloride solutions. *J. Electroanal. Chem. Interfacial Electrochem.* **1970,** *24*, (2–3), 279-286.

13. Nichols, H.; Hexter, R. M., Site symmetry of surface adsorbed molecules. *J. Chem. Phys.* **1981,** *75*, (6), 3126-3136.

14. Grunze, M.; Dowben, P. A., A review of halocarbon and halogen adsorption with particular reference to iron surfaces. *Appl. Surf. Sci* **1982,** *10*, (2), 209-239.

15. Braunstein, P.; Clark, R. J. H., The preparation, properties, and vibrational spectra of complexes containing the AuCl2–, AuBr2–, and AuI2– ions. *J. Chem. Soc., Dalton Trans.* **1973**, (17), 1845-1848.

16. Husson, E.; Quy Dao, N.; Breitinger, D. K., Vibrational spectra and normal coordinate analyses of the gold halides AuX (X = Cl, Br and I). *Spectroc. Acta Pt. A-Molec. Biomolec. Spectr.* **1981,** *37*, (12), 1087-1092.

17. Weaver, M. J.; Hupp, J. T.; Barz, F.; Gordon, J. G.; Philpott, M. R., Surface-enhanced raman spectroscopy of electrochemically characterized interfaces. *J. Electroanal. Chem. Interfacial Electrochem.* **1984,** *160*, (1), 321-333.

18. Wetzel, H.; Gerischer, H.; Pettinger, B., Surface enhanced raman scattering from silver-halide and silver-pyridine vibrations and the role of silver ad-atoms. *Chem. Phys. Lett.* **1981,** *78*, (2), 392-397.

19. Kerker, M.; Siiman, O.; Bumm, L. A.; Wang, D. S., Surface enhanced Raman scattering (SERS) of citrate ion adsorbed on colloidal silver. *Appl. Optics* **1980,** *19*, (19), 3253.

20. Bayle, M.; Combe, N.; Sangeetha, N. M.; Viau, G.; Carles, R., Vibrational and electronic excitations in gold nanocrystals. *Nanoscale* **2014,** *6*, (15), 9157-9165.

21. Girard, A.; Gehan, H.; Crut, A.; Mermet, A.; Saviot, L.; Margueritat, J., Mechanical Coupling in Gold Nanoparticles Supermolecules Revealed by Plasmon-Enhanced Ultralow Frequency Raman Spectroscopy. *Nano Lett.* **2016**.

22. Palpant, B.; Saviot, L.; Lermé, J.; Prével, B.; Pellarin, M.; Duval, E.; Perez, A.; Broyer, M., Plasmon-phonon coupling and resonant raman scattering of silver clusters. *Eur. Phys. J. D* **1999,** *9*, (1), 585-589.

23. Afrooz, A. R. M. N.; Sivalapalan, S. T.; Murphy, C. J.; Hussain, S. M.; Schlager, J. J.; Saleh, N. B., Spheres vs. rods: The shape of gold nanoparticles influences aggregation and deposition behavior. *Chemosphere* **2013,** *91*, (1), 93-98.

Chapter 4. Investigating Mono- and Divalent Cation Induced Aggregation of Gold Nanoparticles in Aqueous Environments via Surface-Enhanced Raman Spectroscopy

Matthew Y. Chan, Weinan Leng and Peter J. Vikesland

The Charles E. Via, Jr. Department of Civil and Environmental Engineering, Virginia Tech, Blacksburg, VA, USA.

Institute for Critical Technology and Applied Science, Virginia Tech, Blacksburg, VA, USA.

NSF-EPA Center for the Environmental Implications of Nanotechnology, Duke University, Durham, NC, USA

4.1 Abstract

Surface-enhanced Raman spectroscopy (SERS) was used as a novel technique to examine gold nanoparticle (AuNP) aggregation behaviour and the interactions between dissolved sodium and calcium halides and the gold nanoparticle surface. The collected SERS data were compared with data from similar experiments characterized using ultraviolet-visible light (UV-Vis) spectroscopy and dynamic light scattering (DLS). The salt concentration range for sodium salts (NaF, NaCl, NaBr, and NaI) was 5-20 mM, while for the calcium salts ($CaCl_2$, $CaBr_2$, and CaI_2) it was from 0.1-1.0 mM. UV-Vis and DLS data revealed that sodium and calcium chloride salts were extraordinarily more effective at inducing AuNP aggregation at these concentration levels. The collected SERS data suggest that halide displacement of AuNP surface citrate groups was a

significant mechanism for AuNP aggregation, particularly for the chloride and bromide salts. The SERS technique provided insight regarding both AuNP aggregation and the surface interactions between AuNP and halides via observation of changes in the surface-enhanced Rayleigh band and the characteristic Au-X^- bands (where X^- is a halide). Qualitative comparison of kinetic data obtained via SERS showed a positive correlation with SERS hotspot formation, as well as a positive correlation between rates of halide attachment to AuNP aggregate surfaces and salt concentration. However, pseudo first-order rate constants showed that bromide exhibited a high enough affinity to the AuNP aggregate surface such that there was no correlation between bromide attachment and salt concentration. All of the chloride salts employed induced AuNPs to form highly fractal aggregate networks that were significantly different from those produced by non-chloride salts. High (20 mM) chloride concentrations produced aggregates large enough to sediment. The SERS method proved to be a valuable supplemental tool to investigate the complex dynamics of AuNP fate and behaviour in aqueous environments.

4.2 Introduction

Nanomaterials are being developed for *in situ* and *in vivo* applications such as cellular imaging and drug delivery.[1,2] Furthermore, they are being incorporated in readily available commercial products such as cosmetics and childcare products.[3,4] Given their widespread application there is a pressing need to develop sensitive tools to characterize nanoparticle behavior in complex aquatic environments. Noble metal nanoparticle tracking is of particular interest because of the potential biomedical applications of noble metal nanoparticles as well as concerns about noble metal toxicity.[1,2,5-8] Understanding the behavior of these nanomaterials in the complex aqueous environment is thus imperative. Similar to other categories of nanomaterials, noble metal

nanoparticles such as gold nanoparticles (AuNP) can be transformed from their pristine starting conditions via a number of mechanisms. These mechanisms may include aggregation, sedimentation, and deposition. Dissolved species in the aqueous environment, such as halides, can interact strongly with the surfaces of noble metal nanomaterials. Current analytical methods used to characterize gold nanoparticle behavior in aqueous environments include microscopy, ultraviolent-visible light (UV-Vis) spectroscopy, and dynamic light scattering (DLS). UV-Vis spectroscopy characterizes the aggregation and morphology changes of AuNPs by monitoring changes in the localized surface plasmon resonance (LSPR) wavelength location and intensity, which are both dependent on the size, shape, and surface chemistry of the AuNPs.[9,10] Unfortunately, UV-Vis spectroscopy suffers from sensitivity issues and is unable to disentangle aggregation from sedimentation.[11] DLS is another popular technique to characterize nanoparticle aggregation and size changes by correlating measured diffusion coefficients with size distributions.[12] However, it is well recognized that DLS exhibits a measuring bias towards larger particles and that this bias is exacerbated when the particle distribution is broad.[13] Conventional DLS measurements have difficulty resolving the size distributions of non-spherical particles and/or aggregates.[14] Furthermore, the aforementioned techniques are incapable of probing the interactions between dissolved species and the nanoparticle surface. Herein, we conducted a thorough investigation of gold nanoparticle aggregation and interaction with dissolved halides via UV-Vis spectroscopy, DLS, and surface enhanced Raman spectroscopy (SERS).

As discussed in Chapter 3, temporal monitoring of the Au-X^- SERS band intensity is a viable method to monitor AuNP aggregation. Detection of AuNP aggregation and the characterization of this transformation by Raman spectroscopy requires several physicochemical factors to be simultaneously in place. Gold nanoparticles are elemental nanocrystals that generally cannot be

detected by Raman spectroscopy directly due their low signals.[15] However, when sodium and calcium halide salts are added to induce AuNP aggregation, the dissociated "spectator" halides are known to interact strongly with gold surfaces, and these gold-halide interactions are readily detected by Raman spectroscopy.[16] In the absence of any signal enhancement mechanisms the halide-gold vibrational modes, while exhibiting relatively large Raman cross-sections, produce Raman signals that are too weak to be detected conventionally due to the short scattering path length.[17] In general, Raman spectroscopy detects inelastically scattered photons that arise from induced dipole interactions.[18] Signals for small inorganic molecules are weak because only a small fraction of incident photons are scattered inelastically, especially when compared to larger organic macromolecules.[19] Therefore, signal augmentation mechanisms such as surface enhancement are necessary for detection and characterization.[20,21] SERS is an extended Raman technique that enhances scattering signals by a factor up to 10^{11}.[22] When the interaction being characterized occurs adjacent to an optical enhancing surface that provides an electric field, signal enhancement can occur through the oscillation of the localized plasmon in resonance with the incident laser of the spectrometer.[23] While noble metal nanoparticles enhance vibrational Raman bands due to surface plasmon effects,[24] the SERS enhancement of individual ≈15 nm spherical nanoparticles is far lower ($< 10^3$) than that exhibited by highly aggregated nanoparticles.[25-27] One primary reason for the higher Raman enhancements of aggregated nanoparticles is the electromagnetic coupling between adjacent nanoscale structural features.[28,29] In particular, electromagnetic coupling gives rise to nano-structural SERS "hotspots" that exhibit higher signal enhancements than individual nanoparticles. In our experiments, the AuNP surfaces act as the optical enhancing surface, greatly increasing the signal strength of the photons inelastically scattered by the gold-halide interactions. Because signal enhancement under these surface enhancing conditions only occurs when the

plasmon oscillations in resonance are perpendicular to the surfaces, gold surfaces with varying nano-scale topography allow for high numbers of oscillation configurations to provide signal enhancements, resulting in the aforementioned SERS "hotspots".[20,30]

Table 4-1 - Vibrational frequency of SERS band of interests.

Surface Interaction	**Approx. Location of SERS Band**
$Au\text{-}F^-$	247 cm^{-1}
$Au\text{-}Cl^-$	242 cm^{-1}
$Au\text{-}Br^-$	183 cm^{-1}
$Au\text{-}I^-$	159 cm^{-1}

SERS hotspots and their formation are crucial to our effort to examine AuNP aggregation via SERS for two reasons: 1) our instrumentation only detects the gold-halide interaction when the scattering signal is enhanced by SERS hotspot formation; 2) when various sodium or calcium halide solutions are added to the AuNP suspension to induce nanoparticle aggregation, the resulting AuNP aggregates possess enough nanoscale surface features to ensure formation of SERS hotspots. The gold-halide interaction used in our experiments to characterize aggregation results in relatively low wavenumber (<400 cm^{-1}) Raman/SERS bands that shift depending on the halide identity (Table 1).[15] Due to instrument limitations most prior Raman spectroscopy studies have not probed these low wavenumber Raman bands; to date there have only been a limited number of studies examining the SERS signals that result from such $Au\text{-}X^-$ interactions.[31-35]

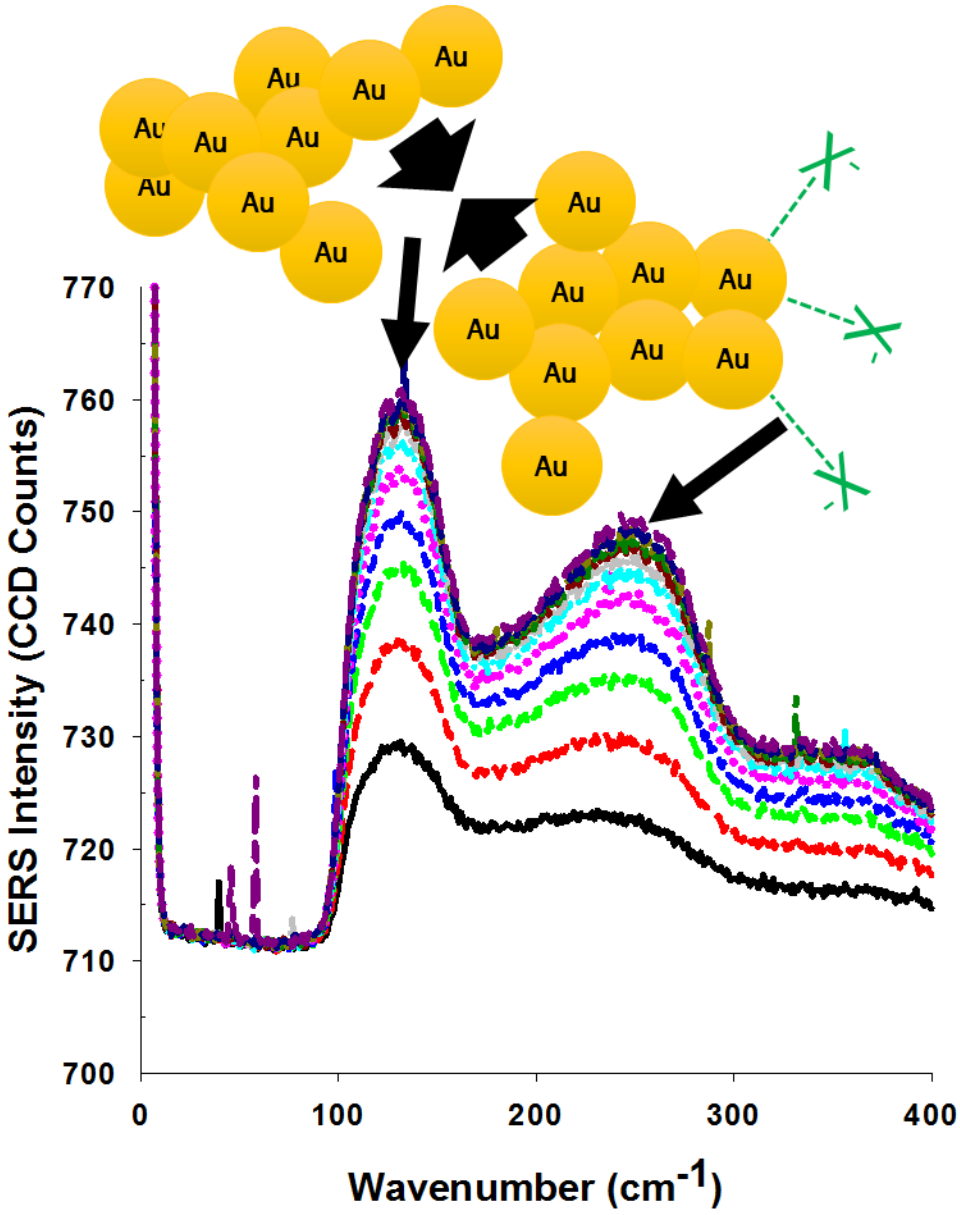

Figure 4-1 – Schematic of SERS signal arising from AuNP aggregation. Peak at ≈126 cm^{-1} is a surface-enhanced Rayleigh Band resulting from AuNP aggregation and the simultaneous formation of SERS hotspots, while the peak at ≈247 cm^{-1} is the Au-X^- (in this example, $X^- = F^-$) interaction enhanced by the SERS hotspots.

An additional point of note is that the aforementioned surface enhancement from the gold aggregate surfaces simultaneously enhance the Rayleigh band centered at 0 cm^{-1}. Due to our standard Raman instrumental set up, optical filters block out this signal below ≈100 cm^{-1}. However, the 'tail' from this Rayleigh band that is not blocked by the optical filter manifests itself as a peak

at ≈126 cm^{-1} (Figure 4-1) if there is sufficient surface enhancement. In other work (yet to be published) conducted within the *Vikesland* research group, there is strong evidence that the development of this surface enhanced Rayleigh band provides an indication of the presence of SERS hotspots. The SERS hotspots formed in our experiments only result from AuNP aggregation and thus the development of this surface enhanced Rayleigh band can be used as a surrogate indicator of particle aggregation. Furthermore, the Au-X^- SERS band described above, serves as an indicator of particle aggregation as well as the interaction of the halides with the particle surface. Analyses of the kinetics of the formation of these bands, in combination with UV-Vis spectroscopy and DLS, provide a fuller picture of the behavior and transformations of AuNPs in the aqueous environment.

4.3 Methods

All chemical reagents were from Fisher Scientific (Pittsburgh, PA) and were of reagent grade purity. Ultra-pure water with a resistivity of 18.2 MΩ·cm (Barnstead Nanopure, Thermo Scientific, Waltham, MA) was used in all experiments. All glassware was cleaned using a laboratory disinfector-washer (Lancer 1400 LXP, Lancer Industry, Lake Mary, FL). Glassware used for nanoparticle syntheses was further cleansed with an aqua regia wash, followed by copious rinsing with ultra-pure water to remove residual acid.

4.3.1 Nanoparticle Synthesis and Characterization

Citrate-coated gold nanoparticles (AuNPs) of diameter 16 ± 1.2 nm (n = 200) as determined via transmission election microscopy and Z_{ave} = 18.99 ± 0.41 nm and zeta potential = -38.4 ± 1.00 mV as determined by DLS were synthesized as described by Turkevich et al.[36] AuNPs were characterized by ultraviolet-visible (UV-Vis) spectroscopy using a Varian Cary 5000 spectrophotometer (Agilent Technologies, Santa Clara, CA) to identify the location of the LSPR band. AuNPs were analyzed via DLS using a Zetasizer NanoZS (Malvern, Westborough, MA) to determine the average hydrodynamic diameter (Z_{ave}) of the suspension via the method of cumulants. Electrophoretic mobility measurements were performed using the same instrument and the Smoluchowski approximation was used to calculate the zeta potential distribution of the suspensions.[37]

4.3.2 Kinetic SERS Measurement of AuNP Aggregation

A 1 mm path length quartz cuvette (Starna, Atascadero, CA) was used for all aggregation experiments. A 1 mL sample of AuNP suspension (≈ 1 mg/L by gold mass) was spiked with a small aliquot (≈ 1 μL) of concentrated salt stock (NaF, NaCl, NaBr, NaI, $CaCl_2$, $CaBr_2$, and CaI_2) to produce suspensions with final salt concentrations between 5 – 20 mM for the sodium salts and 0.1 – 1.0 mM for the calcium salts. These salt-treated AuNP suspensions were then immediately injected into the cuvette. Raman spectra were collected continuously from both near the top and near the bottom of the reactor every 5 minutes. UV-Vis spectroscopy and DLS were used to further characterize the AuNP aggregation state at the conclusion of each kinetic experiment.

4.4 Results and Discussion

4.4.1 AuNP Aggregation as Monitored by UV-Vis Spectroscopy

It is well known that the addition of salt to a nanoparticle suspension will generally destabilize the suspension leading to nanoparticle aggregation. This result is largely due to the compression of the electrical double layer surrounding the AuNPs that negates the repulsive stabilizing forces between particle surfaces, thus allowing attractive forces between surfaces such as van der Waals interactions to prevail.[38-40] Under UV-Vis spectroscopy, AuNP Aggregation can manifest as a change in the shape of the LSPR band in the resulting spectra. Some of these expected spectral changes can be observed in Figure 4-2B (20 mM NaCl added to AuNP) including a decrease of the ≈ 519 nm LSPR band intensity, and deformities in the band shape over time with the development of the two "shoulders" of the peak (i.e., the plateau area below and above the ≈ 519 nm LSPR peak.) The increase in the UV-Vis signal intensity above 600 nm in particular is a good indication of AuNP aggregate formation.[41] One important factor to consider is that while a decrease in the intensity of the LSPR peak is an indication of aggregation, it can also indicate that there is sedimentation occurring within the AuNP suspension. With the exception of the 20 mM NaCl experiment, none of the other sodium halides induced aggregation at such an extent to be detectable by UV-Vis spectroscopy (Figure 4-2).

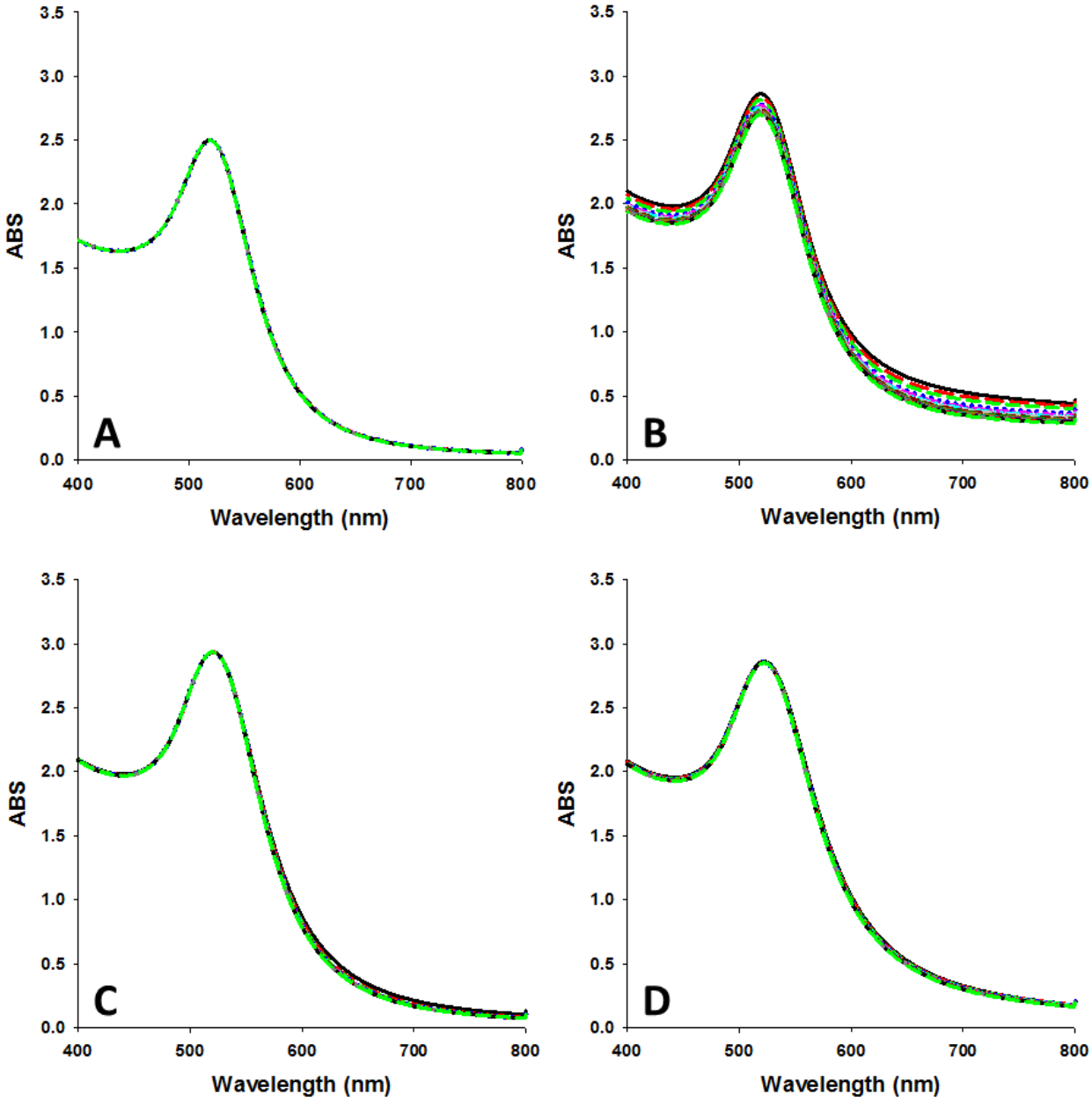

Figure 4-2 – UV-Vis spectra taken after salt addition to a 1 mg/L AuNP suspension at 1 min intervals for 60 minutes. The LSPR band for AuNP used in our experiment is located at 519 nm. AuNP with no salt addition produced a LSPR band that was stable over the time frame of these experiments (data not shown.) A.) 20 mM NaF; B.) 20 mM NaCl); C.) 20 mM NaBr; D.) 20 mM NaI

Other observations of note in the UV-Vis spectra collected in the sodium salt experiments were the fact that there was no detectable redshift (i.e., increase in wavelength) of the LSPR peak for the 20 mM NaCl experiment with the AuNPs (Figure 4-2B) even though aggregation was occurring to such an extent that the LSPR signal was decreasing due to sedimentation. The redshift of the LSPR band is an indication of aggregation and/or particle growth as larger gold nanomaterials exhibit higher wavelength LSPRs.[42-44] We hypothesize that the lack of an LSPR redshift indicates that in the presence of 20 mM NaCl that the AuNP aggregates were sedimenting out of the sampling zone of the spectrometer as rapidly as they formed.

Additional aggregation experiments were performed using the same AuNP suspension, but using calcium halides – $CaCl_2$, $CaBr_2$, and CaI_2. (Note that CaF_2 was not used because it is not soluble in water.) As expected, a lower concentration of calcium halide salts was required to achieve comparable results to the sodium experiments due to effects predicted by the Schulze-Hardy rule.[38] Similar to the NaCl experiments, AuNPs aggregated by addition of 1 mM $CaCl_2$ exhibited the greatest response as detectable by UV-Vis spectroscopy (Figure 4-3A) relative to the other calcium halide salts (Figure 4-3B & C). In contrast to the NaCl experiment, however, AuNP aggregated by 1 mM of $CaCl_2$ not only exhibited a steady redshift in the LSPR band, but also the development of an additional LSPR band at ≈650 nm. This result suggests that AuNPs aggregated by $CaCl_2$ at this concentration level did not sediment to any significant extent. An important observation must be noted at this point that from an electrical double layer point of view, because the AuNPs are negatively charged, it would be the Na^+ and Ca^{2+} ions that screen out the repulsive forces between the particle surfaces and induce aggregation, as described by classical DLVO theory.[39,40]

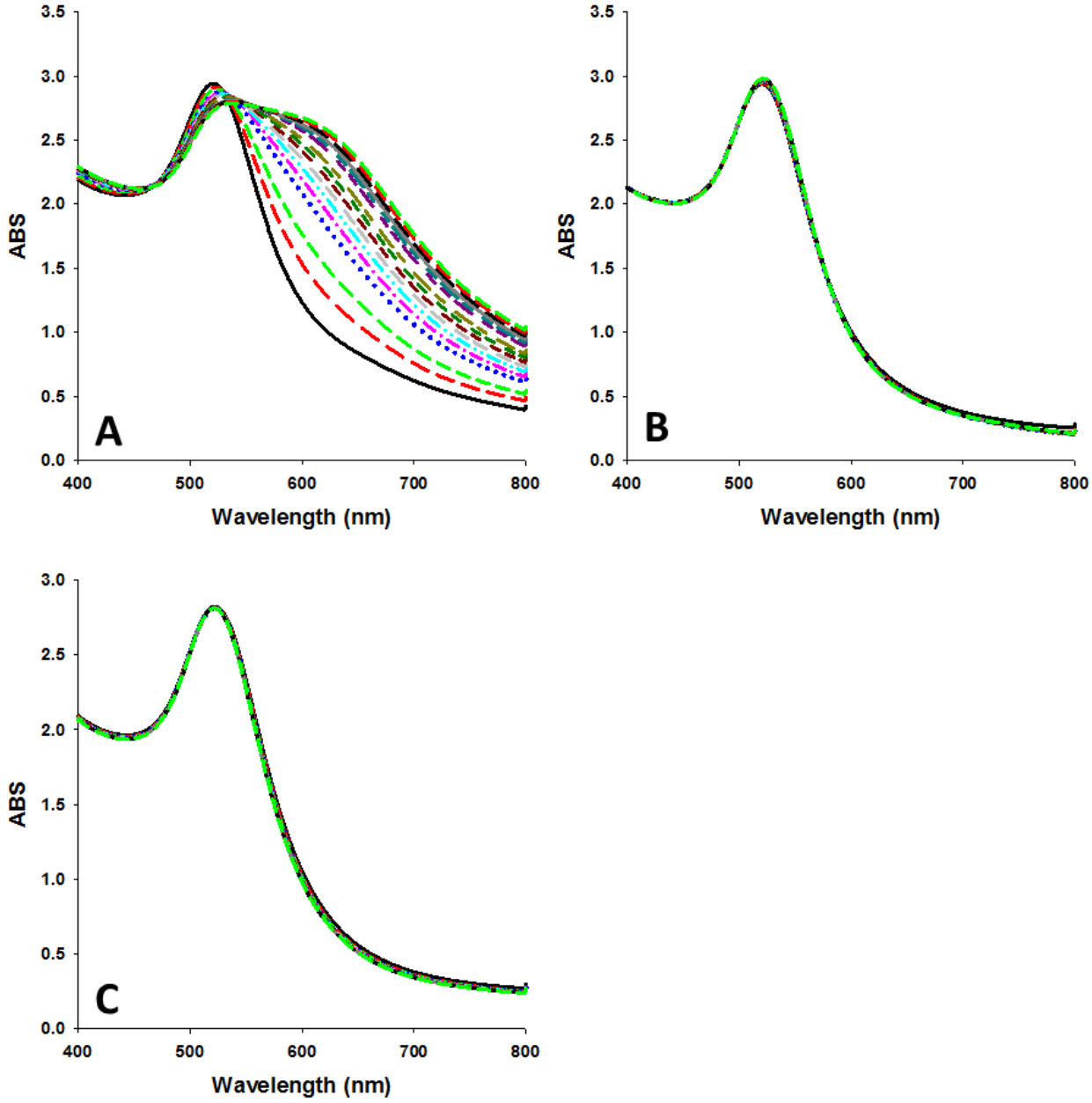

Figure 4-3 – UV-Vis spectra taken after salt addition to AuNP suspension at increasing time intervals superimposed onto the same graph at 1 min intervals. As time progresses from 0 to 60 minutes the shape of the spectra changes. The localized surface plasmon resonance band for unaggregated AuNP used in our experiment is located at ≈ 519 nm. AuNP with no salt addition produced a LSPR band that is stable over time (data not shown.) A.) 1.0 mM $CaCl_2$ B.) 1.0 mM $CaBr_2$; C.) 1.0 mM CaI_2.

Interestingly, as the results from both the sodium and calcium salt series of experiments (Figure 4-2 & 4-3) indicated, the identity of the halide counter ion has a significant impact on the aggregation behavior of the AuNP. In our experiments, non-chloride salts do not aggregate AuNPs to a UV-Vis detectable extent under our test conditions.

4.4.2 Gold Nanoparticle Aggregation as Verified by DLS

Data collected by DLS indicated that all of the sodium salts aggregated the AuNPs to a certain extent after a 60-minute period (Table 4-2) as compared to unaggregated AuNP. According to the DLS data, the addition of NaF, NaBr, and NaI aggregated the AuNP suspension to a similar extent ($Z_{ave} \approx 30$ nm), while the same molar concentration of NaCl produced aggregates with average diameters that were an order of magnitude longer.

Table 4-2 – DLS data collected with AuNPs after sodium salt addition. Data were collected after a 60-minute period had elapsed following salt addition. All salt additions were at 20 mM. Z_{ave} is the average diameter of the AuNP in the suspension. The polydispersity index (PDI) is a fitted parameter calculated by the particle analyzer, which varies between 0 and 1, with < 0.05 generally considered to be "monodisperse."

Salt Addition	Z_{ave} (nm)	PDI (dimensionless)
No Salt Blank	17.7 ± 0.80	0.03 ± 0.010
NaF	30.0 ± 0.45	0.55 ± 0.0067
NaCl	305 ± 12.28	0.90 ± 0.10
NaBr	32.3 ± 0.76	0.54 ± 0.086
NaI	31.8 ± 2.79	0.69 ± 0.15

The polydispersity index (PDI) of each salt addition experiment is worth noting. As with the Z_{ave} DLS data, the NaF, NaBr, and NaI experiments produced AuNP suspensions with similar magnitude PDI values after 60 minutes, while NaCl addition produced an aggregated AuNP

suspension that was far more polydisperse. These DLS data suggest that there is some degree of AuNP aggregation that occurs following addition of 20 mM of NaF/NaBr/NaI that is undetectable by UV-Vis spectroscopy. The large differences in aggregate size after 60 min between those formed by 20 mM NaCl and the other sodium salts supports the hypothesis that there may be significant sedimentation occurring in the NaCl experiment.

Table 4-3 – DLS data collected from AuNP after calcium salt addition. Data collected after a 60-minute waiting period had elapsed after salt addition. All salt additions at 1.0 mM. Z_{ave} is the average diameter of the AuNP in the suspension. The polydispersity index (PDI) is a fitted parameter calculated by the particle analyzer, which varies between 0 and 1, with < 0.05 generally considered to be "monodisperse."

Salt Addition	Z_{ave} (nm)	PDI (dimensionless)
Blank	17.7 ± 0.80	0.03 ± 0.010
$CaCl_2$	180 ± 3.47	0.48 ± 0.013
$CaBr_2$	36.2 ± 0.280	0.47 ± 0.0025
CaI_2	39.1 ± 0.473	0.57 ± 0.0055

DLS results from the calcium halide addition experiments indicated that the chloride salt again formed the largest aggregate as compared to the aggregates formed in the presence of $CaBr_2$ or CaI_2 (Table 4-3). For the calcium salts, however, the PDI was comparable between $CaCl_2$, $CaBr_2$, and CaI_2. This result differs from the sodium experiments where NaCl addition produced far more polydisperse aggregates. Combined with the UV-Vis data the DLS analyses support the following hypotheses: a.) aggregates formed by sodium salts have significantly different physical properties from aggregates formed by calcium salts, and b.) the halide counter ions (F^-, Cl^-, Br^-, and I^-) have a significant role in aggregate formation. These two factors likely have some cooperative effects

as aggregates formed by NaCl and by $CaCl_2$ also differ from one another as indicated by their relative PDI values.

4.4.3 Investigation of AuNP Aggregation via SERS

When NaF, NaCl, NaBr, or NaI are added to an AuNP suspension, the sodium cations act to induce the aggregation of the negatively-charged citrate-coated AuNPs, while the halides (F^-, Cl^-, Br^-, or I^-) interact with the AuNP aggregate surface giving rise to Raman signals as enhanced by SERS hotspots. In the collected SERS spectra there are two spectral features that provide an indication of AuNP aggregation: the characteristic Au-X^- band as summarized in Table 4-1, and the surface enhanced Rayleigh band at ≈126 cm^{-1} (Figure 4-4). We note that the surface enhancement of the Rayleigh band only occurs in the presence of SERS hotspots. As such, the presence of the 126 cm^{-1} surface-enhanced Rayleigh band and its time-dependent increase in intensity provide insight as to the properties and kinetics of AuNP aggregation since these aggregates are the only source of surface enhancement under our experimental conditions.

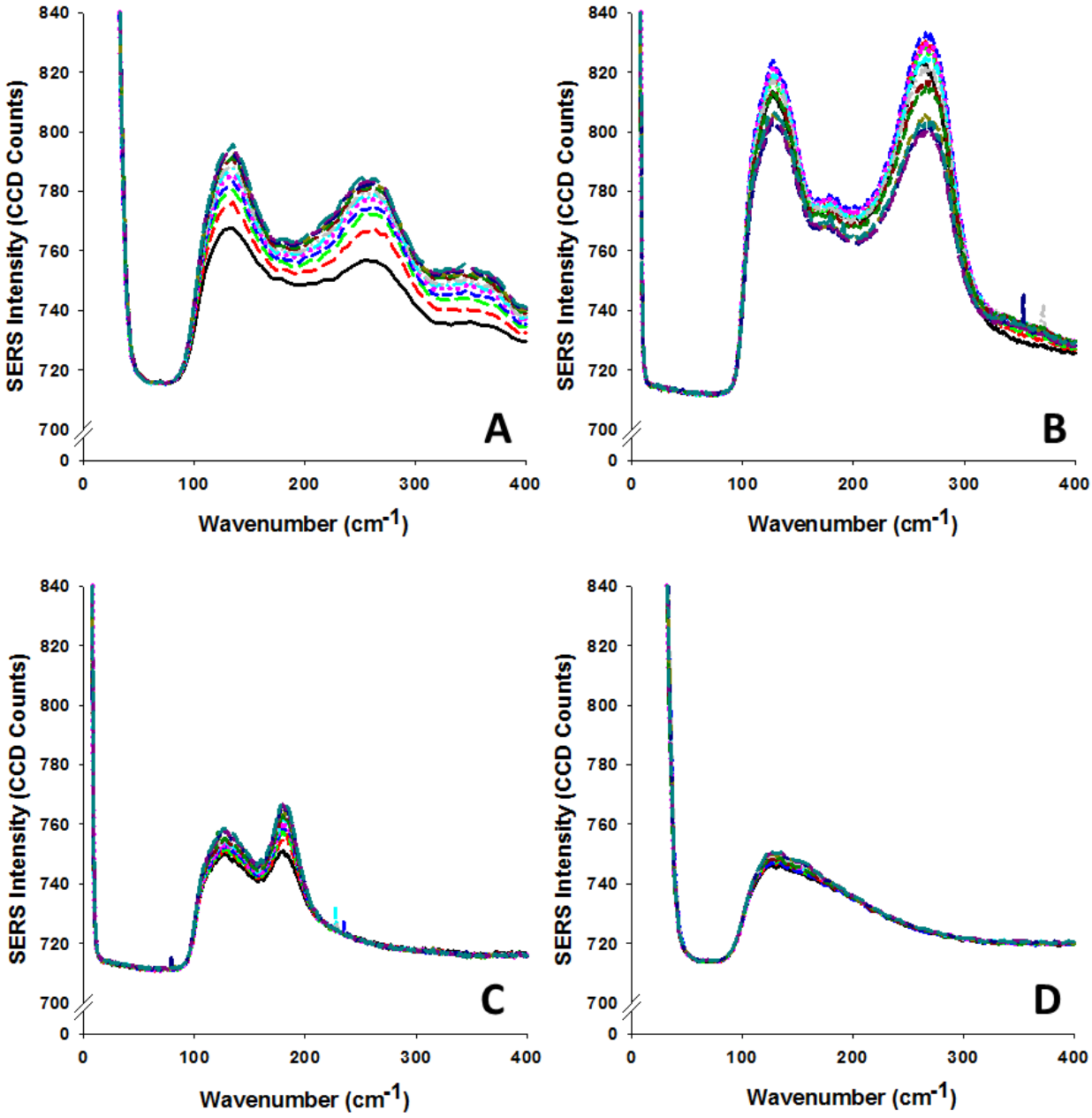

Figure 4-4 – SERS spectra taken for 60 minutes after salt addition to an AuNP suspension. Black solid plots are at t = 1 min; each subsequent plot was taken starting at t = 5 min using a 5 min interval. As time progresses the Au-X^- SERS characteristic band generally increases, except for NaI. A.) 20 mM NaF (characteristic SERS band at ≈247 cm^{-1}); B.) 20 mM NaCl (characteristic SERS band at ≈242 cm^{-1}); C.) 20 mM NaBr; (characteristic SERS band at ≈184 cm^{-1}) D.) 20 mM NaI (characteristic SERS band at ≈158 cm^{-1}, not present.) Note the presence and in some cases growth of the surface enhanced Rayleigh band at ≈126 cm^{-1}.

There are some similarities between the SERS data (Figure 4-4) and the UV-Vis data (Figure 4-2). As with the UV-Vis data, the NaCl experiments resulted in much greater detectable SERS responses in terms of aggregation. We were able to observe a significant increase in the SERS signal intensity over time for both the surface enhanced Rayleigh band (at ≈ 126 cm^{-1}) and the respective Au-X^- bands for all sodium halide experiments except NaI. The temporal trends of the SERS bands of interest are illustrated in Figure 4-5.

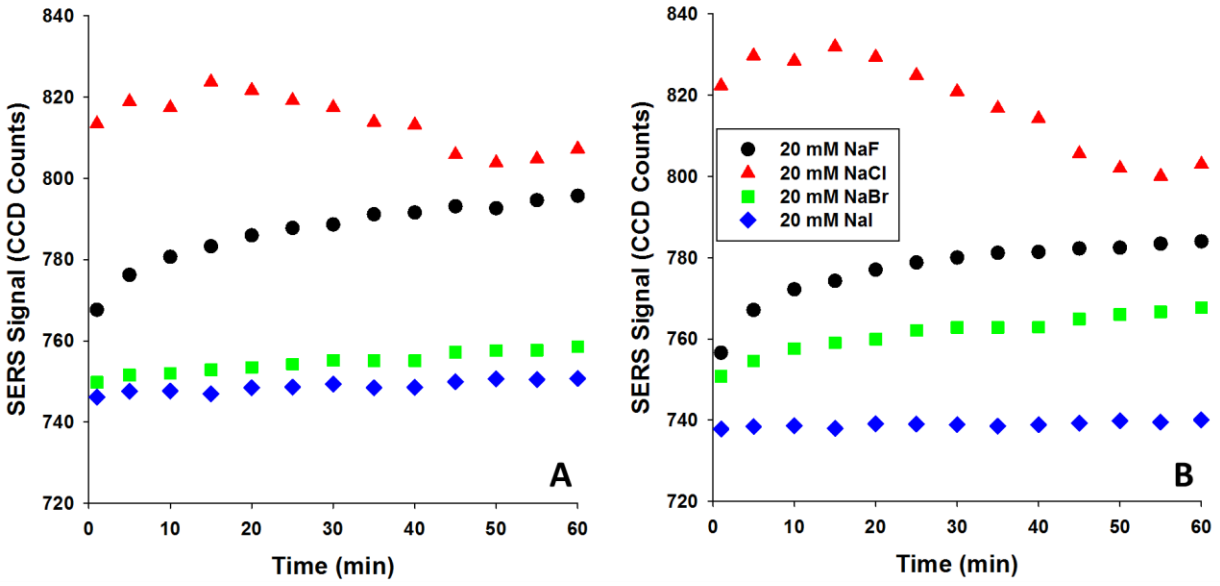

Figure 4-5 – Time-resolved band intensities for 20 mM NaX experiments. A.) Surface enhanced Rayleigh bands after salt (NaF, NaCl, NaBr, NaI) addition to AuNP suspension; B.) Au-X^- characteristic SERS band intensity after salt (NaF, NaCl, NaBr, NaI) addition to AuNP suspension

The SERS data for sodium experiments corroborated both the UV-Vis and DLS data as all of the results point to a much greater extent of aggregation via NaCl addition compared to all other sodium halides at the same concentration. Focusing initially on the surface-enhanced Rayleigh band, SERS was able to detect significant aggregation activity from addition of 20 mM of NaF as

well as 20 mM of NaBr (Figure 4-4 and Figure 4-5A). This result was not observable via UV-Vis spectroscopy (Figure 4-2), suggesting that there are some sensitivity difficulties with that method as DLS data (Table 4-2) confirmed that there was some aggregation occurring following NaF and NaBr addition. NaI addition elicited only a surface-enhanced Rayleigh band that slightly increased in intensity with time (Figure 4-4D and Figure 4-5A). Data from the Au-X^- SERS band provides additional information about AuNP behavior following sodium salt addition. This is especially apparent when comparing the relative change in intensity of the surface-enhanced Rayleigh bands (indicative of SERS hotspots formation, i.e., aggregation) and the Au-X^- characteristic SERS band (indicative of aggregation/SERS hotspots formation **and** halide-gold surface interaction).

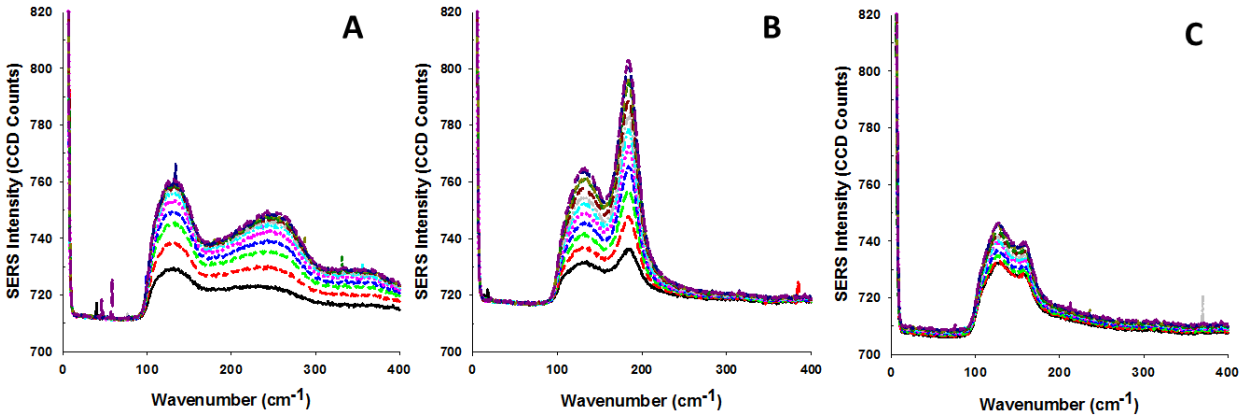

Figure 4-6 – SERS spectra taken after salt addition to an AuNP suspension at increasing time intervals superimposed onto the same graph. Black solid plots are at t = 1 min, each subsequent plot were taken starting at t = 5 min, and with increasing 5 minute intervals up to 60 minute. As time progresses the Au-X SERS characteristic band generally increases in intensity. A.) 1.0 mM $CaCl_2$ (characteristic SERS band at ≈242 cm^{-1}); B.) 1.0 mM $CaBr_2$ (characteristic SERS band at ≈184 cm^{-1}); C.) 1.0 mM CaI_2; (characteristic SERS band at ≈158 cm^{-1})

Repeating the calcium experiments while monitoring the Rayleigh and SERS bands resulted in informative data (Figure 4-6). As with the sodium experiments, AuNP aggregated with calcium salts exhibits both the surface-enhanced Rayleigh band at ≈126 cm^{-1} and the characteristic Au-X^- SERS bands. There are similarities and discrepancies between the calcium SERS and UV-Vis/DLS results.

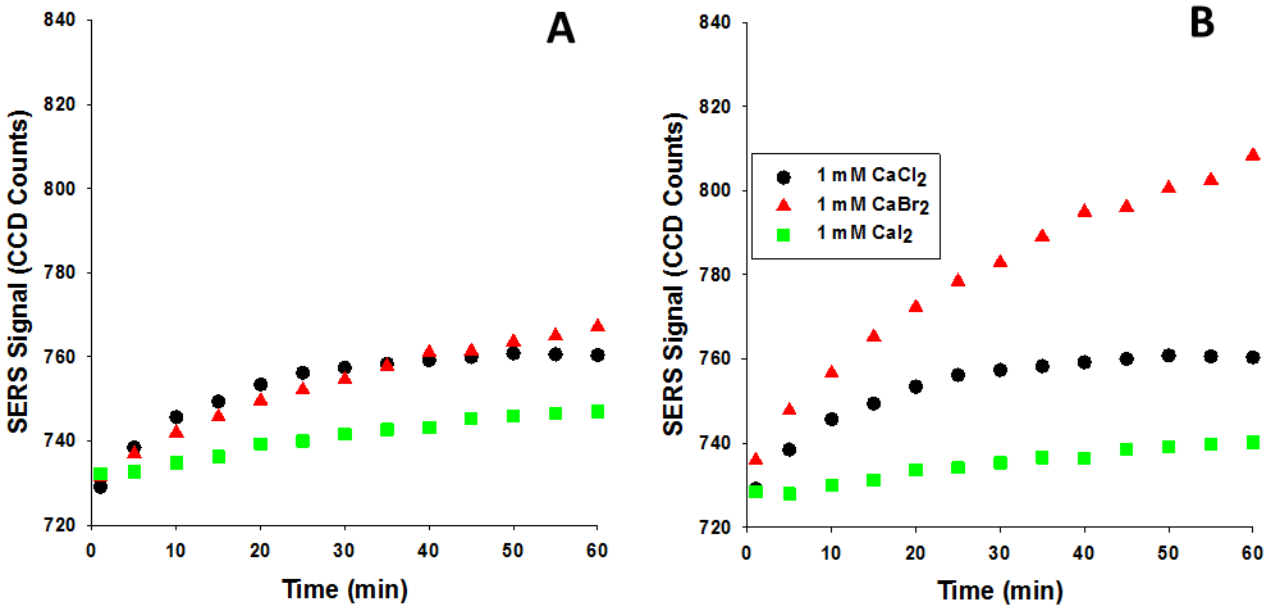

Figure 4-7 – Time-resolved band intensities for 1 mM CaX_2 experiments. A.) Surface enhanced Rayleigh bands after salt ($CaCl_2$, $CaBr_2$, CaI_2) addition to AuNP suspension; B.) Au-X^- characteristic SERS band intensity after salt ($CaCl_2$, $CaBr_2$, CaI_2) addition to AuNP suspension

Both UV-Vis and DLS results indicated that 1 mM $CaCl_2$ significantly aggregated the AuNP suspension, while $CaBr_2$ and CaI_2 showed stable LSPR bands and only small increases in the DLS-obtained Z_{ave}. However, the SERS results for calcium showed that $CaBr_2$ exhibited similar intensity trends in the surface-enhanced Rayleigh band as did $CaCl_2$ (Figure 4-7A). For the characteristic Au-X SERS bands, the $CaBr_2$ experiment exhibited the highest increasing trend,

suggesting that, at least according to SERS, it has the highest gold-halide activity when compared to the other calcium salt experiments.

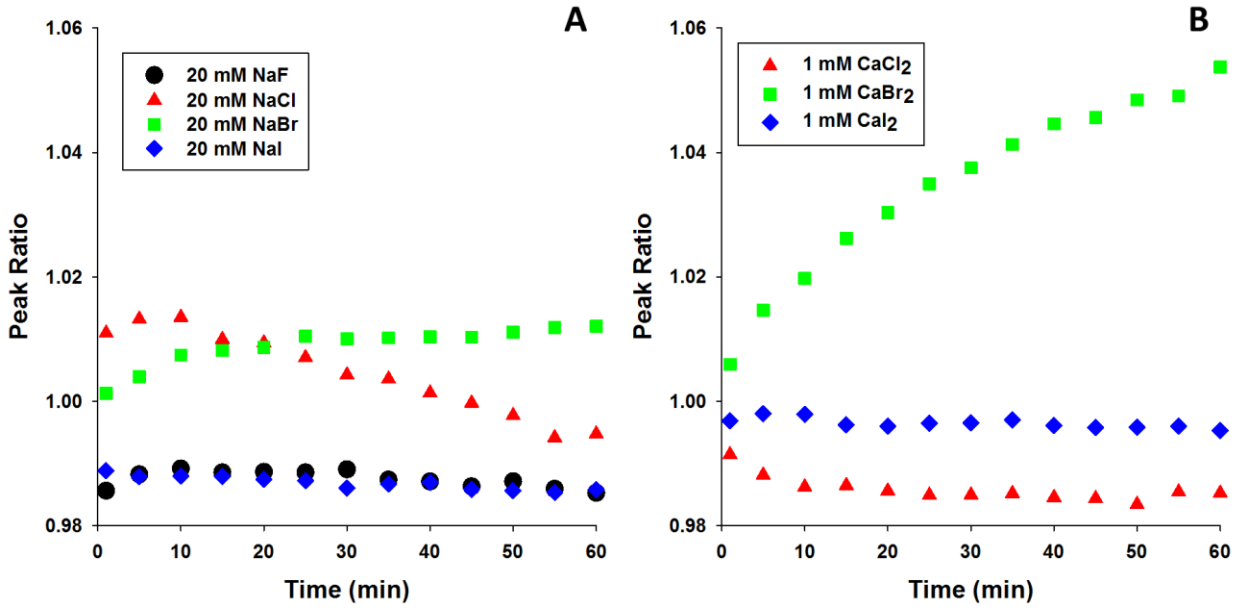

Figure 4-8 – The Raman signal intensity ratio between characteristic Au-X^- SERS band / surface-enhanced Rayleigh band. A.) 20 mM NaX experiments with AuNP; B.) 1.0 mM CaX_2 experiments with AuNP.

Comparing the signal intensity between the surface-enhanced Rayleigh bands and the characteristic Au-X^- bands provides useful information regarding the potential relationship between the aggregation state of the AuNPs and the interactions between gold surfaces and dissolved halides (Figure 4-8). For peak ratio values that are larger than 1, it would imply the possibility that there more gold-halide interactions generating the resultant SERS signal than gold aggregate SERS hotspot formation. The clearest example would be the experiments involving bromide. For both NaBr and $CaBr_2$, this peak ratio increases as time increases thus possibly implying that as more aggregates form that bromide ions are strongly attaching themselves to the

aggregate surface at a rate that is possibly faster than the rate of aggregation. Accordingly, it is possible that the Br^- interaction with the gold surface is positively reinforcing aggregation. On the other hand, addition of both fluoride and iodide (whether it be sodium or calcium salts) resulted in peak ratio trends that are rather flat and <1 throughout. This result and trend implies that for F^- and I^- that AuNP aggregation and the gold surface-halide interactions are occurring at similar rates. We note that the true behavioral dynamics are difficult to detangle here, because the Au-X^- characteristic SERS band requires both Au-X^- interaction **and** SERS hotspots formation.

The differences in AuNP aggregation behavior observed in our salt experiments are consistent with each halide's differing affinity to the AuNP surface and their varying capacities to displace surface citrate groups on the AuNPs.[45] Fluoride has a low affinity to the gold surface and generally does not displace surface citrate groups, therefore any aggregation that occurs in the NaF experiments is due to the dampening of repulsive electrical double layer interactions.[46] Both bromide and iodide bind strongly to gold surfaces, and as such can displace significant amounts of surface citrate groups. Accordingly, as the AuNPs aggregate following 20 mM NaBr or NaI addition, tightly bound aggregates formed, resulting in low signal both in the SERS experiments and via UV-Vis.[46-49] Chloride displaces surface citrate groups only partially, such that there are preferential sites on the AuNP surface that lead to the formation of large, fractal, and "sponge-like" aggregates.[46] Variable displacement of AuNP surface citrate groups by different halides accounts for the aggregation trends observed by SERS (Figure 4-5 & 4-7), UV-Vis (Figure 4-2 & 4-3), and also DLS (Table 4-2 & 4-3). If we focus on the peak ratios for each experiments and interpret those results within the context of the halide-citrate displacement phenomenon, we can note that the only consistent increasing trends that were observed were in the NaBr and the $CaBr_2$ experiments. A previous study by Zhang *et al*., found that the NaCl was the halide salt that created the most out of

the ordinary "sponge-like" aggregate networks, our work here shows that even at low salt concentrations (Zhang *et al.* conducted their experiments at 180 mM salt concentrations, and did not utilize calcium or any divalent salts in their aggregation experiments,) bromide and its corresponding cations induces AuNP aggregation behavior that a.) is significantly dependent on the halide concentration, implying bromide displacement of AuNP surface citrate groups to be a significant if not dominant contributor to aggregation; b.) even though bromide salts do significantly induce AuNP aggregation to such a degree as to be detected by SERS, the aggregates formed are physically different from those formed by chloride salts as they are smaller according to UV-Vis and DLS, and do not sediment according to UV-Vis and SERS, and c.) the "sponge-like" aggregate networks formed by NaCl addition observed in Zhang *et al.*'s work also formed in our experiments albeit at a much lower NaCl concentration (one order of magnitude apart), but not in our $CaCl_2$ experiments, at least not to a similar degree as the AuNP aggregates formed by NaCl because the former did not sediment (SERS and UV-Vis data), are much less polydisperse (DLS data), and exhibited significant LSPR redshifts not observed in any other aggregation experiments (UV-Vis data).

4.4.4 Preliminary Survey of AuNP Aggregation Kinetics

To obtain preliminary qualitative rate constants, the SERS aggregation experiments were repeated using a range of salt concentrations (raw SERS data in Appendix C). By fitting the linear portion of the change in the time-resolved peaks (for both the surface-enhanced Rayleigh band and the characteristic Au-X^- band) qualitative rate constants could be determined (Table 4-4).

Table 4-4 – Estimate of qualitative pseudo-first order rate constants from various SERS experiments with different salts. The Au-Au column includes rate constants determined from surface-enhanced Rayleigh band kinetics; The Au-X column includes rate constants determined from characteristic Au-X^- SERS bands. *Italicized* values are questionable due to low data quality (see footnote below). All rate constants have units of CCD counts/min.

	Concentration (mM)	Au-Au	Au-X^-	Au-X^-/Au-Au
NaF	5	0.42	0.44	1.06
	10	0.80	0.91	1.16
	20	1.42	1.71	1.20
NaCl	5	0.13	0.11	0.80
	10	1.05	1.21	0.87
	20	*0.62***	*0.57***	*1.09***
NaBr	5	*-0.02**	*-0.05**	*2.18**
	10	*-0.01**	*-0.03**	*2.97**
	20	0.14	0.43	2.78
NaI	5	*-0.06**	*-0.04**	*0.80**
	10	*0.01**	*-0.01**	*-0.96**
	20	*0.07**	*0.03**	*0.42**
$CaCl_2$	0.2	*0.07**	*0.06**	*0.92**
	0.5	*0.02**	*0.05**	*2.16**
	0.6	0.21	0.09	0.43
	0.8	0.15	0.12	0.78
	1	1.07	0.89	0.83
$CaBr_2$	0.1	*0.00**	*0.18**	*229.43**
	0.2	0.22	0.43	1.97
	0.5	0.50	1.02	2.06
	0.8	0.62	1.39	2.23
	1	0.93	1.87	2.01
CaI_2	0.5	0.05	0.05	0.70
	1	0.22	0.22	0.81

*Dubious value due to low to no aggregation behavior from SERS spectra (see Appendix C) **Dubious value due to significant sedimentation of aggregates (Figure 4-5)

Much of the information that can be gathered from the qualitative kinetic rate constants obtained in the SERS experiments corroborate with the results obtained the peak ratios. For example, the rate constant for the gold-halide interaction for 1.0 mM $CaBr_2$ is the largest, but the rate constants for hotspot formation (from the surface-enhanced Rayleigh band) are comparable to those from the 1.0 mM $CaCl_2$ experiment, just as the peak ratio plots suggested (Figure 4-8). There was a general increasing trend in the rate constants that correlates to salt concentration, which was expected because as salt concentration increases, aggregation tends to increase whether it be due to colloidal effects or surface citrate group displacement. The rate constant ratios (far right column of Table 4-4) offer some possible insight to the relationship between aggregation and halide attachment to AuNP aggregate surface, as there was a general increasing trend with respect to salt concentration as well. This would imply that for most of the aggregation condition with sodium or calcium salts, a higher salt concentration increases the halide attachment rate more so than the aggregation rate. The exception being the $CaBr_2$ series of experiments, in which the rate constant ratios exhibited no trends. This may suggest that bromide has a high affinity to gold surfaces that has little correlation with its concentration. This is consistent with the known trend in halide affinity to gold surfaces: $I^- > Br^- > Cl^- > F^-$.[45] Of note, iodide salts consistently did not exhibit an observable signal via SERS, DLS, or UV-Vis. Neither did they produce an observable SERS signal for the Au-X^- characteristic band, even though theoretically it has the highest affinity to gold surfaces.[48] A working hypothesis for the iodide results is that iodide essentially displaces all surface citrate groups of the AuNP and the resulting aggregates are dense and compact, which would be in contrast with the highly fractal aggregate networks that the chloride and bromide salts form. This hypothesis is supported by our UV-Vis data and DLS data, as Z_{ave} was small for the

iodide experiments, and there was no significant LSPR redshift. Compact AuNP aggregates serve as poor SERS hotspots, therefore we do not observe a characteristic Au-X^- SERS signal.

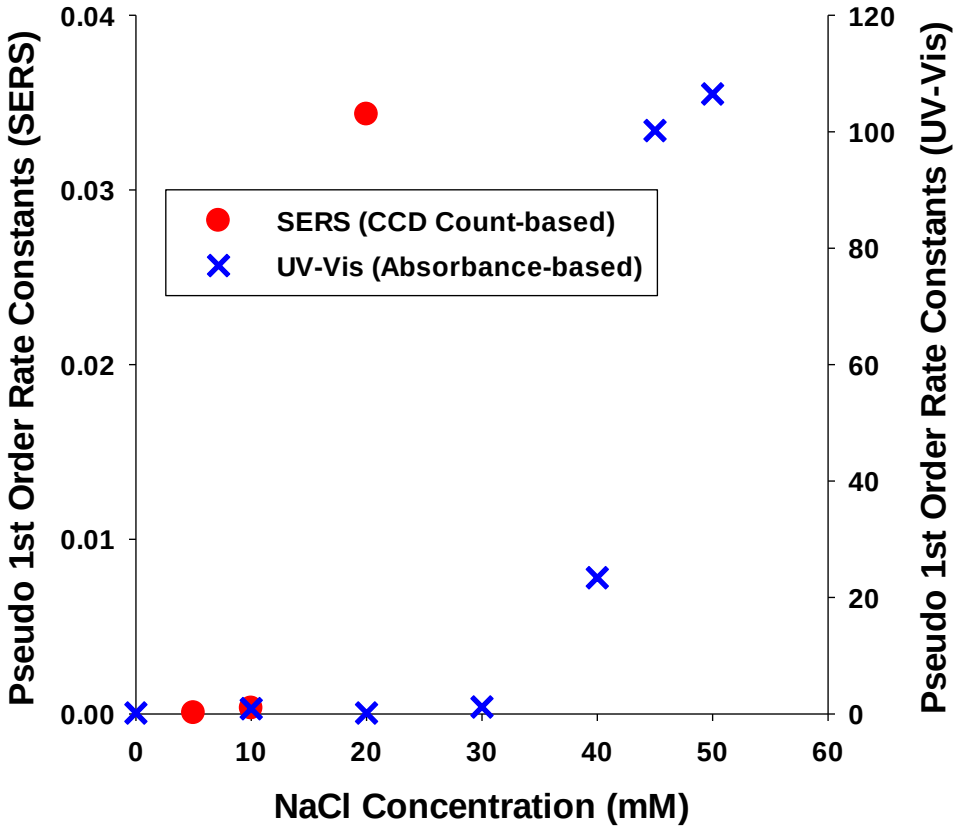

Figure 4-9 – Pseudo first order rate constants obtained by fitting a regression through the linear portion of the time-resolved SERS or UV-Vis data.

The kinetics of AuNP aggregation at low salt concentration are difficult to investigate. As salt concentration increases in the aqueous environment, the attractive forces between particle surfaces generally dominate over the repulsive forces, and at some concentration the fast diffusion-limited aggregation mechanism overtakes the slower reaction-limited aggregation process. The salt concentration level at which this occurs is referred to as the critical coagulation concentration (CCC).[50] A common method to determine the CCC is to plot aggregation rate constants against

salt concentration, and interpolate the inflection point of the resultant plot. In Figure 4-9, rate constants from the experiment where 20 mM NaCl was used to aggregate AuNP are plotted against the NaCl concentration. Two sets of data are presented in Figure 4-9, one collected by UV-Vis and one by SERS. While the two sets of rate constants are not directly comparable due to the lack of a calibration curve and fundamental differences of the science behind SERS and LSPR, there is some quantitative observable that is significant here. Most notably, the determined qualitative CCC is markedly different between the two methods, even though the experimental environments were exactly the same. There is a significant rate constant value jump between 40-45 mM NaCl for the UV-Vis dataset, where we can surmise the CCC is located somewhere between these two concentration values. However, this rate constant value "jump" occurs at a much lower concentration for the SERS set of data between 10 and 20 mM. It is currently unclear if there is a sensitively issue with the UV-Vis and LSPR method of investigating aggregation behavior, including CCC determination, but suffice to say that based on this single comparison we can conclude that the SERS method is much more sensitive at detecting and characterizing microscale interactions (such as surface attachment of halide and the development of fractal aggregates [i.e., SERS hotspot formation]) than UV-Vis spectroscopy, which is more suited to macroscale interactions such as changes in the local dielectric environment or the average plasmonic behavior of the AuNP suspension.

4.4.5 Addressing Sedimentation During AuNP aggregation

Notably from our UV-Vis data (Figure 4-2B) and our SERS data (Figure 4-5) there is strong indication of significant sedimentation of AuNP aggregates as evident by a decrease in the LSPR

band intensity over time and an observed drop in the SERS signal after an initial increasing period for the 20 mM NaCl aggregation experiments.

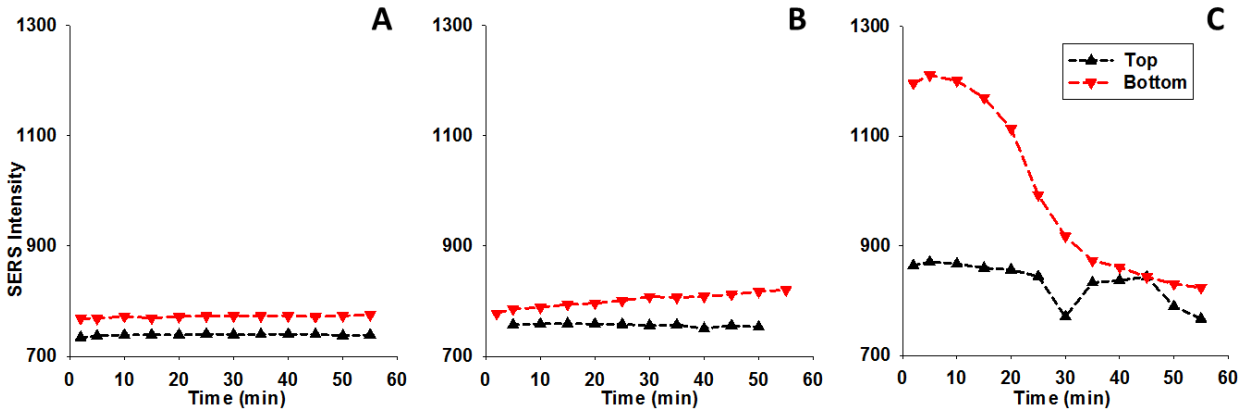

Figure 4-10 – Time resolved Au-Cl$^-$ SERS intensity at 242 cm^{-1} with varying addition of NaCl: A.) 5 mM, B.) 10 mM, C.) 20 mM. Black upward triangle data points obtained near the top of the sample cell. Red downward triangle data points obtained near the bottom of the sample cell.

To examine the sedimentation behavior of the AuNP aggregation following NaCl addition, we took advantage of the three-dimensional capabilities of the confocal Raman spectrometer and monitored AuNP aggregation by NaCl addition both towards the top of the sample cell and near the bottom (Figure 4-10). As shown in Figure 4-10A and 4-10B when 5 mM and 10 mM of NaCl were added, there was no evidence of significant sedimentation occurring. In the experiment where 20 mM of NaCl was added (Figure 4-10C, mirroring data presented in Figure 4-5), there was significant differences between the Au-Cl$^-$ SERS signal collected near the top of the sample cell and near the bottom. The data collected near the top of the sample cell steadily declined over time, while never producing a SERS signal intensity comparable to that collected near the bottom of the sample cell. This SERS signal trend is evidence that aggregates formed toward the top of the sample cell almost immediately sediment away from the sampling zone of the Raman spectrometer.

SERS data collected near the bottom of the sample cell exhibit very high signal intensities (Figure 4-10C) initially, with the signal gradually decreasing over time. This is an indication that high signal from Au-Cl^- were detected as large AuNP aggregates quickly form, but as these aggregates become larger over the experimental timeframe, a significant amount of the aggregates formed sedimented to the bottom of the sampling cell, well outside of the sampling zone of the Raman spectrometer. This is an advantage of the SERS method, since with UV-Vis spectroscopy it is difficult to detangle whether it was aggregation or sedimentation causing the LSPR signal drop, or both.

DLS measurements indicate that with no salt present, the hydrodynamic diameter of the AuNPs was 15.03 ± 0.03 nm, while at 20 nm NaCl after a 1-hour exposure, the AuNP aggregates were 305.2 ± 12.28 nm. Using a modified Stokes Law that accounts for fractal aggregates the ≈ 385 nm AuNP aggregates have an estimated settling velocity of 3.26 nm/s (See Appendix 3 for detailed calculations).[51-53] Using the classical Stokes Law, indivitual ≈ 15 nm AuNP would exhibit a settling velocity of 0.0073 nm/s.[54] The sampling cell has a depth of 0.1 cm (that is, 10×10^6 nm), therefore, at the end of the 60 min kinetic experiment run, the AuNP would have traveled 26.3 nm, and the aggregates would have traveled 11700 nm. While these calculations greatly simplify the experimental environment and many assumptions were made, they generally support our hypothesis of significant sedimentation of AuNP aggregate formed following 20 mM NaCl addition. At higher salt concentrations, it is probable that the aggregates formed are highly prone to sedimentation, thus increasing the difficulty of detangling the various transformation these AuNPs may experience in the aqueous environment.

4.5 Conclusions

From an environmental perspective, AuNPs exhibit very complex transformations in water of varying chemical properties. As this study has illustrated, relying on one analytical techniques is insufficient to thoroughly describe aggregation and other transformative processes that nanomaterials may undergo in the aqueous environment. The SERS technique used here provides advantages over UV-Vis spectroscopy and DLS: a.) SERS provide aggregation information as well as information that describes interactions between the aggregate surface and dissolved chemical species in water; b.) SERS provide some limited capacity to detangle nanomaterial sedimentation and aggregation in water, and c.) SERS is in general a more microscopic method with a higher sensitivity than UV-Vis spectroscopy and DLS. We present this technique as an important supplement for the continued work investigating nanomaterial fate and dynamics in the aqueous environment.

Disclosure

This work is being prepared as a manuscript to be submitted to the Royal Chemical Society for consideration to be published as an Article in the journal *Environmental Science: Nano*.

.

Supporting Information

All supporting information cited in this chapter is located in Appendix C.

References

1. Xu, H.; Li, Q.; Wang, L.; He, Y.; Shi, J.; Tang, B.; Fan, C., Nanoscale optical probes for cellular imaging. *Chem. Soc. Rev.* **2014,** *43*, (8), 2650-2661.

2. Sultana, S.; Khan, M. R.; Kumar, M.; Kumar, S.; Ali, M., Nanoparticles-mediated drug delivery approaches for cancer targeting: a review. *J. Drug Target.* **2012,** *21*, (2), 107-125.

3. Quadros, M. E.; Pierson, R.; Tulve, N. S.; Willis, R.; Rogers, K.; Thomas, T. A.; Marr, L. C., Release of Silver from Nanotechnology-Based Consumer Products for Children. *Environ. Sci. Technol.* **2013,** *47*, (15), 8894-8901.

4. Mihranyan, A.; Ferraz, N.; Strømme, M., Current status and future prospects of nanotechnology in cosmetics. *Prog. Mater. Sci.* **2012,** *57*, (5), 875-910.

5. Vo-Dinh, T.; Fales, A. M.; Griffin, G. D.; Khoury, C. G.; Liu, Y.; Ngo, H.; Norton, S. J.; Register, J. K.; Wang, H.-N.; Yuan, H., Plasmonic nanoprobes: from chemical sensing to medical diagnostics and therapy. *Nanoscale* **2013,** *5*, (21), 10127-10140.

6. Wijnhoven, S. W. P.; Peijnenburg, W. J. G. M.; Herberts, C. A.; Hagens, W. I.; Oomen, A. G.; Heugens, E. H. W.; Roszek, B.; Bisschops, J.; Gosens, I.; Van De Meent, D.; Dekkers, S.; De Jong, W. H.; van Zijverden, M.; Sips, A. J. A. M.; Geertsma, R. E., Nano-silver – a review of available data and knowledge gaps in human and environmental risk assessment. *Nanotoxicology* **2009,** *3*, (2), 109-138.

7. Khlebtsov, N.; Dykman, L., Biodistribution and toxicity of engineered gold nanoparticles: a review of in vitro and in vivo studies. *Chem. Soc. Rev.* **2011,** *40*, (3), 1647-1671.

8. Li, N.; Zhao, P.; Astruc, D., Anisotropic Gold Nanoparticles: Synthesis, Properties, Applications, and Toxicity. *Angew. Chem.-Int. Edit.* **2014,** *53*, (7), 1756-1789.

9. Nehl, C. L.; Hafner, J. H., Shape-dependent plasmon resonances of gold nanoparticles. **2008,** *18*, (21), 2415-2419.

10. Doak, J.; Gupta, R. K.; Manivannan, K.; Ghosh, K.; Kahol, P. K., Effect of particle size distributions on absorbance spectra of gold nanoparticles. *Physica E: Low-dimensional Systems and Nanostructures* **2010,** *42*, (5), 1605-1609.

11. Chan, M. Y.; Vikesland, P. J., Porous Media-Induced Aggregation of Protein-Stabilized Gold Nanoparticles. *Environ. Sci. Technol.* **2014,** *48*, (3), 1532-1540.

12. Berne, B. J.; Pecora, R., *Dynamic Light Scattering: With Applications to Chemistry, Biology, and Physics*. Courier Corporation: 2000; p 388.

13. Murdock, R. C.; Braydich-Stolle, L.; Schrand, A. M.; Schlager, J. J.; Hussain, S. M., Characterization of Nanomaterial Dispersion in Solution Prior to In Vitro Exposure Using Dynamic Light Scattering Technique. *Toxicol. Sci.* **2008,** *101*, (2), 239-253.

14. Aragón, S. R.; Pecora, R., Theory of dynamic light scattering from polydisperse systems. *J. Chem. Phys.* **1976,** *64*, (6), 2395-2404.

15. Alvarez-Puebla, R. A.; Liz-Marzán, L. M., SERS Detection of Small Inorganic Molecules and Ions. *Angew. Chem.-Int. Edit.* **2012,** *51*, (45), 11214-11223.

16. Cotton, F. A.; Wilkinson, G.; Murillo, C. A.; Bochmann, M., *Advanced Inorganic Chemistry*. 6 edition ed.; Wiley-Interscience: New York, 1999; p 1376.

17. McCreery, R. L., Raman Spectroscopy of Surfaces. In *Raman Spectroscopy for Chemical Analysis*, John Wiley & Sons, Inc.: 2000; pp 373-413.

18. Pelletier, M. J., *Analytical Applications of Raman Spectroscopy*. 1 edition ed.; Blackwell Publishing: Osney Mead, Oxford ; Malden, MA, 1999; p 496.

19. Long, D. A., *Raman spectroscopy*. McGraw-Hill International Book Company: London, 1977.

20. Blatchford, C. G.; Campbell, J. R.; Creighton, J. A., Plasma resonance—enhanced Raman scattering by absorbates on gold colloids: the effects of aggregation. *Surf. Sci.* **1982,** *120*, (2), 435-455.

21. Creighton, J. A.; Blatchford, C. G.; Albrecht, M. G., Plasma resonance enhancement of Raman scattering by pyridine adsorbed on silver or gold sol particles of size comparable to the excitation wavelength. *J. Chem. Soc. Faraday II* **1979,** *75*.

22. Blackie, E. J.; Ru, E. C. L.; Etchegoin, P. G., Single-Molecule Surface-Enhanced Raman Spectroscopy of Nonresonant Molecules. *J. Am. Chem. Soc.* **2009,** *131*, (40), 14466-14472.

23. Smith, E.; Dent, G., *Modern Raman Spectroscopy: A Practical Approach*. John Wiley & Sons: 2013; p 216.

24. Otto, A.; Mrozek, I.; Grabhorn, H.; Akemann, W., Surface-enhanced Raman scattering. *J. Phys.: Condens. Matter* **1992,** *4*, (5).

25. Kerker, M., Estimation of surface-enhanced Raman scattering from surface-averaged electromagnetic intensities. *J. Colloid Interface Sci.* **1987,** *118*, (2), 417-421.

26. Zeman, E. J.; Schatz, G. C., An accurate electromagnetic theory study of surface enhancement factors for silver, gold, copper, lithium, sodium, aluminum, gallium, indium, zinc, and cadmium. *J. Phys. Chem.* **1987,** *91*, (3), 634-643.

27. Kerker, M.; Siiman, O.; Bumm, L. A.; Wang, D. S., Surface enhanced Raman scattering (SERS) of citrate ion adsorbed on colloidal silver. *Appl. Optics* **1980,** *19*, (19).

28. Zhu, Z.; Zhu, T.; Liu, Z., Raman scattering enhancement contributed from individual gold nanoparticles and interparticle coupling. *Nanotechnology* **2004,** *15*, (3).

29. Maxwell, D. J.; Emory, S. R.; Nie, S., Nanostructured Thin-Film Materials with Surface-Enhanced Optical Properties. *Chem. Mater.* **2001,** *13*, (3), 1082-1088.

30. Creighton, J. A.; Blatchford, C. G.; Albrecht, M. G., Plasma resonance enhancement of Raman scattering by pyridine adsorbed on silver or gold sol particles of size comparable to the excitation wavelength. *J. Chem. Soc. Faraday II* **1979,** *75*, 790.

31. Gao, P.; Weaver, M. J., Metal-adsorbate vibrational frequencies as a probe of surface bonding: halides and pseudohalides at gold electrodes. *J. Phys. Chem.* **1986,** *90*, (17), 4057-4063.

32. Jeffrey, M. I.; Watling, K.; Hope, G. A.; Woods, R., Identification of surface species that inhibit and passivate thiosulfate leaching of gold. *Miner. Eng.* **2008,** *21*, (6), 443-452.

33. Bozzini, B.; Romanello, V.; Mele, C., A SERS investigation of the electrodeposition of Au in a phosphate solution. *Surf. Coat. Technol.* **2007,** *201*, (14), 6267-6272.

34. Loo, B. H., In situ identification of halide complexes on gold electrode by surface-enhanced Raman spectroscopy. *J. Phys. Chem.* **1982,** *86*, (4), 433-437.

35. Gao, P.; Weaver, M. J., Surface-enhanced Raman spectroscopy as a probe of adsorbate-surface bonding: benzene and monosubstituted benzenes adsorbed at gold electrodes. *J. Phys. Chem.* **1985,** *89*, (23), 5040-5046.

36. Turkevich, J.; Stevenson, P. C.; Hillier, J., A study of the nucleation and growth processes in the synthesis of colloidal gold. *Discuss. Faraday Soc.* **1951,** *11*.

37. Smoluchowski, M., Contributiona la théorie de l'endosmose électrique et de quelques phenomenes corrélatifs. *Bull. Intl Acad. Sci. Cracovie* **1903,** *8*, 182-200.

38. Schulze, H., Schwefelarsen in wässriger Lösung. *J. Prakt. Chem.* **1882,** *25*, (1), 431-452.

39. Verwey, E. J. W.; Overbeek, J. T. G., *Theory of the Stability of Lyophobic Colloids*. Courier Dover Publications: 1999; p 228.

40. Derjaguin, B. V.; Landau, L., Theory of the stability of strongly charged lyophobic sols and the adhesion of strongly charged particles in solutions of electrolytes. *Acta Physicochim. URSS* **1941,** *14*, 633-662.

41. Khlebtsov, N. G.; Dykman, L. A.; Krasnov, Y. M.; Mel'nikov, A. G., Light Absorption by the Clusters of Colloidal Gold and Silver Particles Formed During Slow and Fast Aggregation. *Colloid J.* **2000,** *62*, (6), 765-779.

42. Diegoli, S.; Manciulea, A. L.; Begum, S.; Jones, I. P.; Lead, J. R.; Preece, J. A., Interaction between manufactured gold nanoparticles and naturally occurring organic macromolecules. *Sci. Total Environ.* **2008,** *402*, (1), 51-61.

43. Kim, T.; Lee, C.-H.; Joo, S.-W.; Lee, K., Kinetics of gold nanoparticle aggregation: Experiments and modeling. *J. Colloid Interface Sci.* **2008,** *318*, (2), 238-243.

44. Fang, C.; Zhao, G.; Xiao, Y.; Zhao, J.; Zhang, Z.; Geng, B., Facile Growth of High-Yield Gold Nanobipyramids Induced by Chloroplatinic Acid for High Refractive Index Sensing Properties. *Scientific Reports* **2016,** *6*, 36706.

45. Magnussen, O. M., Ordered Anion Adlayers on Metal Electrode Surfaces. *Chem. Rev.* **2002,** *102*, (3), 679-726.

46. Zhang, Z.; Li, H.; Zhang, F.; Wu, Y.; Guo, Z.; Zhou, L.; Li, J., Investigation of Halide-Induced Aggregation of Au Nanoparticles into Spongelike Gold. *Langmuir* **2014,** *30*, (10), 2648-2659.

47. Magnussen, O. M.; Ocko, B. M.; Wang, J. X.; Adzic, R. R., In-Situ X-ray Diffraction and STM Studies of Bromide Adsorption on Au(111) Electrodes. *J. Phys. Chem.* **1996,** *100*, (13), 5500-5508.

48. Ocko, B. M.; Watson, G. M.; Wang, J., Structure and electrocompression of electrodeposited iodine monolayers on gold (111). *J. Phys. Chem.* **1994,** *98*, (3), 897-906.

49. Wasileski, S. A.; Weaver, M. J., Electrode Potential-Dependent Anion Chemisorption and Surface Bond Polarization As Assessed by Density Functional Theory. *J. Phys. Chem. B* **2002,** *106*, (18), 4782-4788.

50. Tezak, B.; Matijevic, E.; Schuiz, K. F., Coagulation of Hydrophobic Sols in Statu Nascendi. III. The Influence of the Ionic Size and Valency of the Counterion. *J. Phys. Chem.* **1955,** *59*, (8), 769-773.

51. Vikesland, P. J.; Rebodos, R. L.; Bottero, J. Y.; Rose, J.; Mason, A., Aggregation and sedimentation of magnetite nanoparticle clusters. *Environ. Sci.: Nano* **2016,** *3*, (3), 567-577.

52. Li, X.; Logan, B. E., Collision Frequencies of Fractal Aggregates with Small Particles by Differential Sedimentation. *Environ. Sci. Technol.* **1997,** *31*, (4), 1229-1236.

53. Thill, A.; Moustier, S.; Aziz, J.; Wiesner, M. R.; Bottero, J. Y., Flocs Restructuring during Aggregation: Experimental Evidence and Numerical Simulation. *J. Colloid Interface Sci.* **2001,** *243*, (1), 171-182.

54. Stokes, G. G., On the Effect of the Internal Friction of Fluids on the Motion of Pendulums. *Transactions of the Cambridge Philosophical Society* **1851,** *9*, 8.

Chapter 5. Conclusions

The work discussed in Chapters 2, 3, and 4 points to one conclusion: that new knowledge and analytical techniques will be essential to improve our collective understanding of the vastly complex dynamics of gold (as well as other types) nanomaterial behavior in the water environment. In Chapter 2, we illustrated that past techniques (column studies, UV-Vis spectroscopy) and past theories (colloidal filtration theory, DLVO theory) were insufficient for investigating and explaining the observed behavior of gold nanoparticles in water (in this case, specifically groundwater) environments. We concluded that there was significant AuNP aggregation occurring in the porespace of the packed-column used in our experiments. In Chapter 3, we proposed that Raman spectroscopy, and specifically SERS can be used to analyze the surface interaction between gold nanoparticles/aggregates and dissolved halides in water. The results from this chapter suggest that these SERS-active interactions are halide-specific, and can be used as an analytical technique to quantify AuNP aggregation in water. Finally, in Chapter 4, we combined the SERS technique developed in Chapter 3 with more traditional analytical methods (UV-Vis and DLS) to investigate AuNP behavior in water in the presence of monovalent (sodium) and divalent (calcium) halide salts at varying concentration levels. Many diverging results emerged from this series of experiments, with different analytical techniques providing separate pieces of the puzzle. Specifically, the SERS method we developed showed that beyond colloidal effects (Schulze-Hardy rule and DLVO theory), the dissolved halides in water played a very significant role in the aggregation behaviors of AuNP, especially at concentration levels below the generally accepted critical coagulation concentration. In addition, sedimentation of AuNP, previously thought of as being negligible under our conditions, proved to be a significant phenomenon in these systems.

The road ahead to improve our understanding of the complexity of nanomaterial fate and dynamics in the water environment is long. This work showed that no single analytical technique provided the full picture, and that past assumptions that we may hold to be true for many colloidal systems did not completely apply to citrate-coated gold nanomaterials in the water environment. Our hope is that the work presented here adds to the knowledge of nanotechnology and its implications on the environment, and that moving forward, we will slowly but surely unveil the whole story that is the complex dynamics of gold nanoparticle fate and dynamics in the water environment.

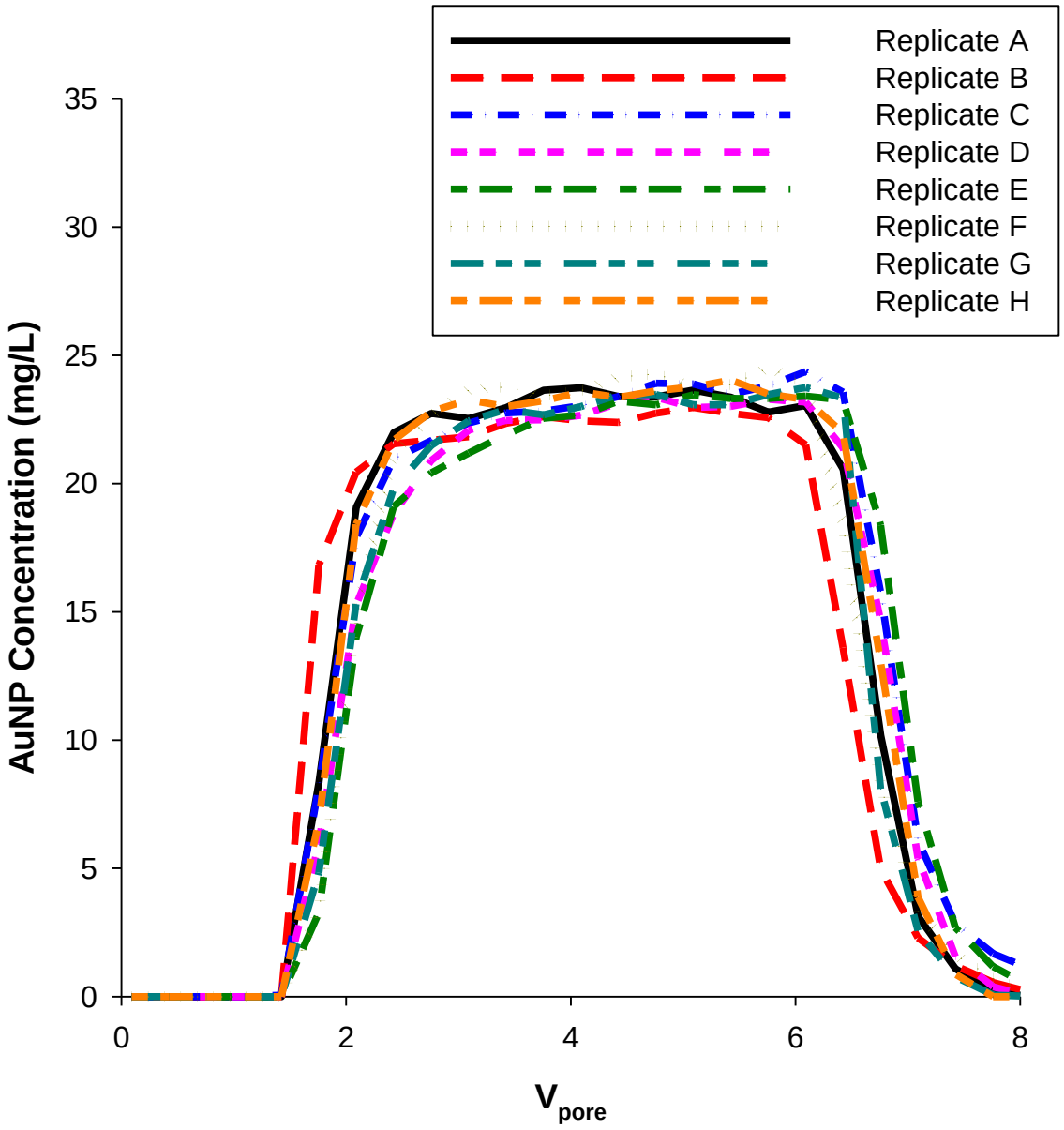

Figure A-1 – Replicate cit-AuNP breakthrough curves (n = 8) for 16 nm nanoparticles. The mobile phase consisted of 2 mM $NaHCO_3$ as a buffer. C_0 for cit-AuNP was ≈24.5 mg/L and the injection volume was $5V_{pore}$. Nitrate tracer studies were performed before and after each replicate (see Figure A-2).

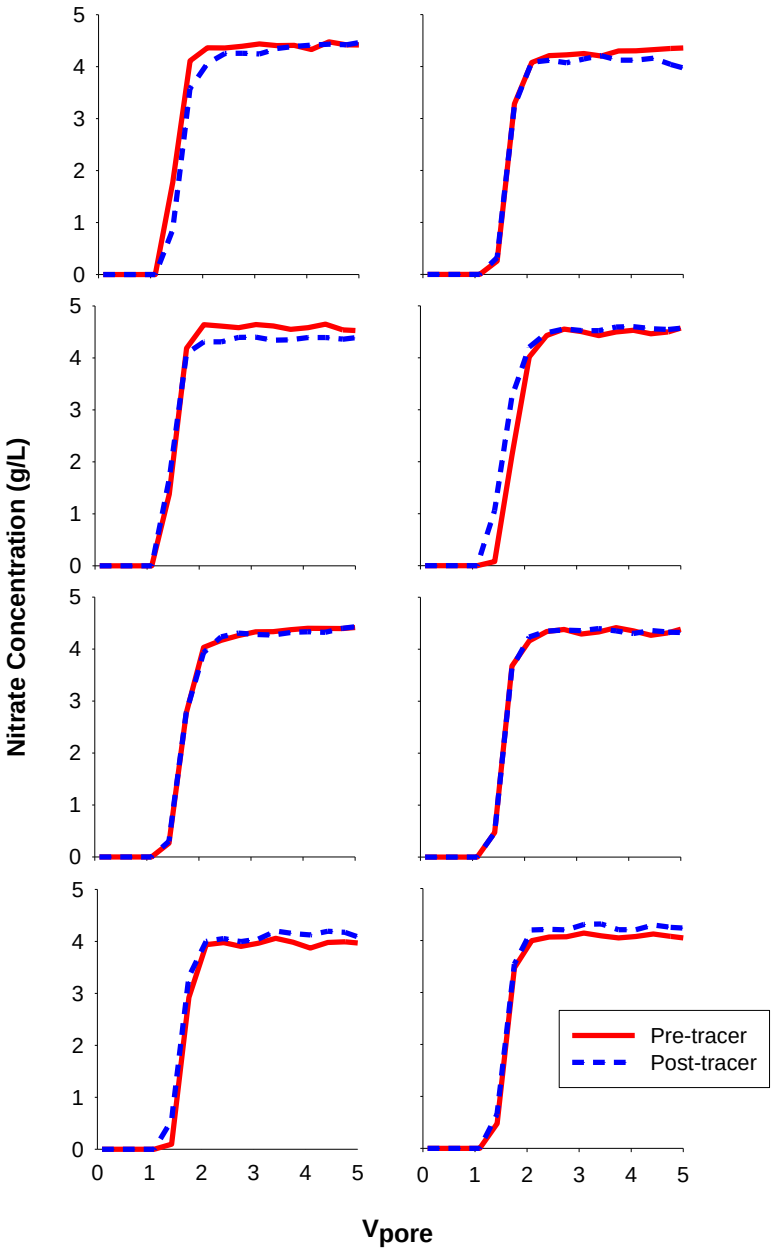

Figure A-2 – Representative breakthrough curves from nitrate tracer studies performed before and after AuNP injection. C_0 for nitrate ($NaNO_3$) was 4.54 g/L and the injection volume was 5 V_{pore}. Mobile phase contained 2 mM $NaHCO_3$ as a buffer. Each graph represents a pair of tracer breakthrough curves from an independent column experiment.

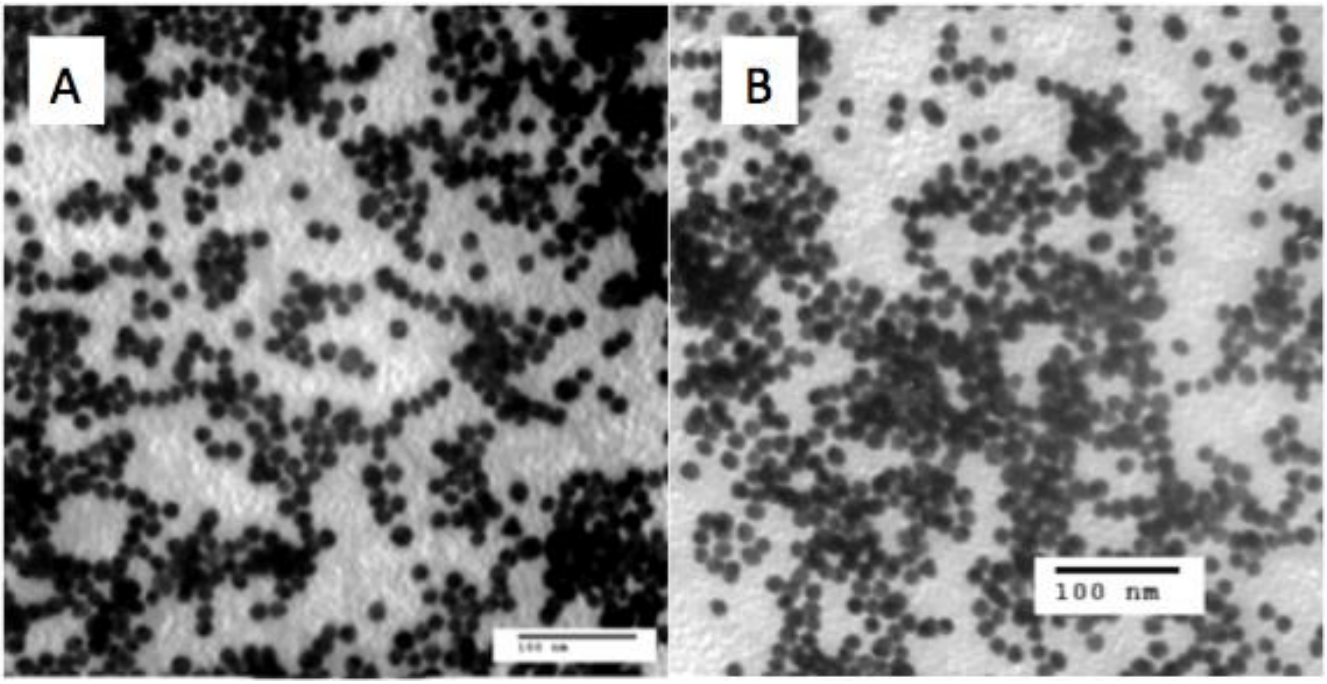

Figure A-3 – TEM images of A) cit-AuNP and B) BSA-cit-AuNP. ImageJ analysis of these figures indicates an AuNP core diameter of 16 ± 1.2 nm (n = 200).

Table A-1 – Characterization data of cit-AuNP and BSA-cit-AuNP

	d_{TEM} (nm)	d_{DLS} (nm)[b]	Electrophoretic mobility ($\mu m \cdot cm \cdot V^{-1} \cdot s^{-1}$)[b]	Zeta potential (mV)[b]
Cit-AuNP	16 ± 1.2[a]	19.7 ± 0.1	-3.01 ± 0.06	-38.4 ± 1.00
BSA-Cit-AuNP	16 ± 1.2[a]	29.4 ± 0.1	-1.93 ± 0.11	-24.6 ± 1.64

[a]The d_{TEM} values for the cit-AuNP and BSA-cit-AuNP nanoparticles reflect the core AuNP diameter.

[b]Electrophoretic mobility and d_{DLS} determined in nanopure water with 2 mM $NaHCO_3$. pH fixed at ≈ 8.

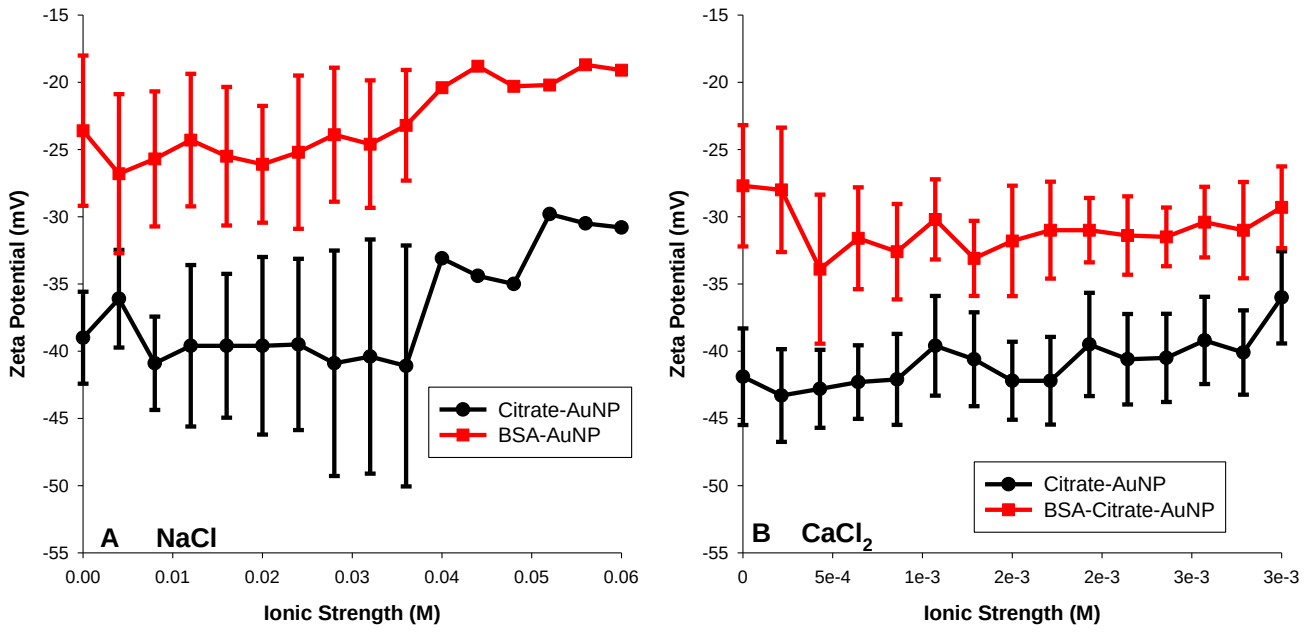

Figure A-4 – The AuNP zeta potential increases with an increase in ionic strength. The solution pH was fixed at ≈8. A) NaCl titration from 0-0.6 M ionic strength. B) $CaCl_2$ titration from 0-0.003 M ionic strength. Error bars indicate 95% confidence interval; 20 measurements were collected per data point. The error bars not included in part of Figure A-4A are the result of an instrument software limitation at high ionic strengths. Data obtained by NanoZS particle analyzer.

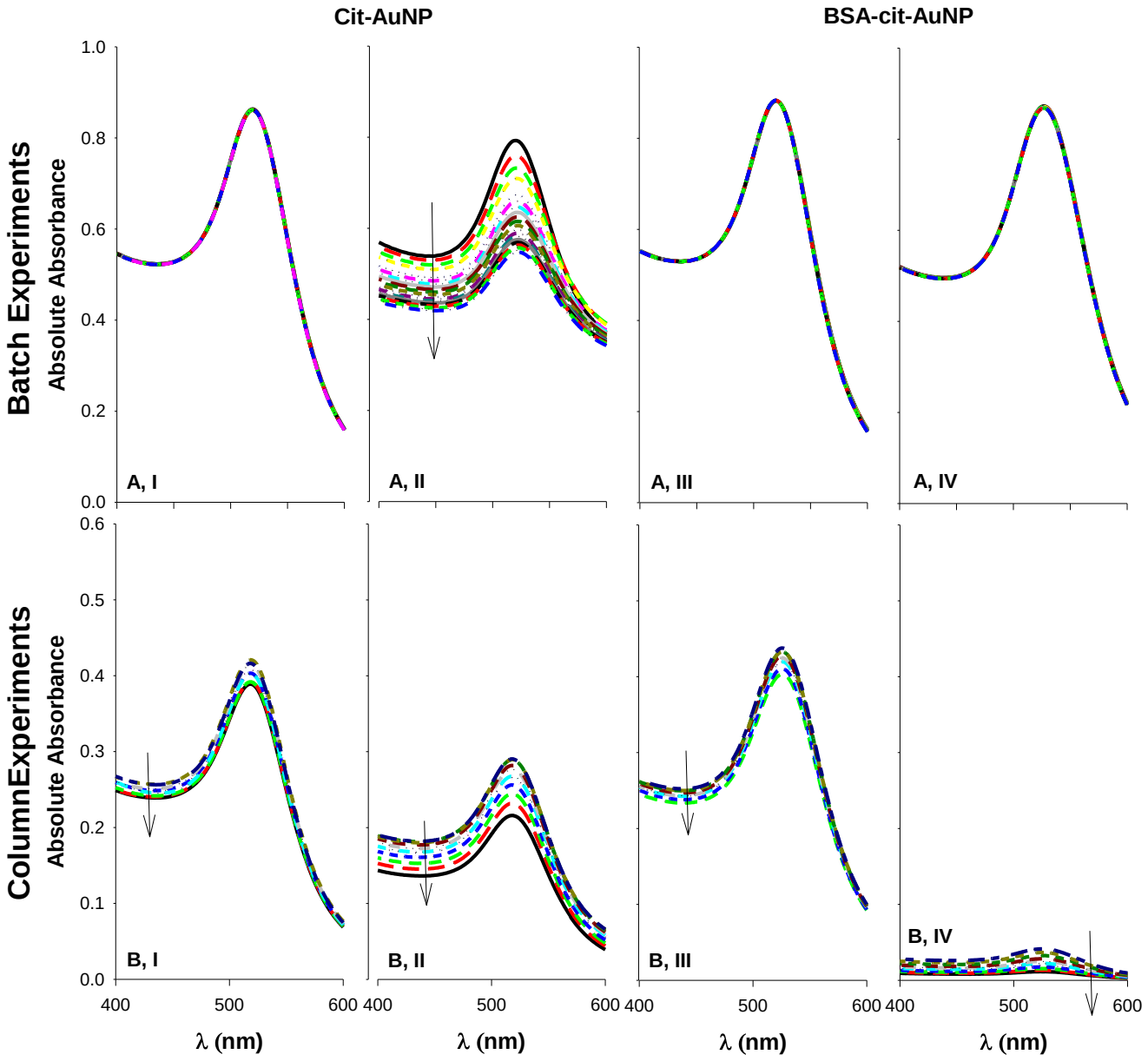

Figure A-5 – Comparison of UV-Vis spectra for batch and column experiments in the presence of NaCl. As labeled, the four graphs on the left are for cit-AuNP, while the plots on the right are for BSA-cit-AuNP. Plots labeled A in the top row are batch results; B in the bottom row are column data. NaCl concentrations: I = 20 mM, II = 40 mM, III = 5 mM, IV = 22 mM. The batch data were obtained over a timeframe relevant to the 'plateau' retention times in the column. The column data were obtained for V_{pore} values representative of the 'plateau' in the breakthrough curve. Arrows indicate time progression.

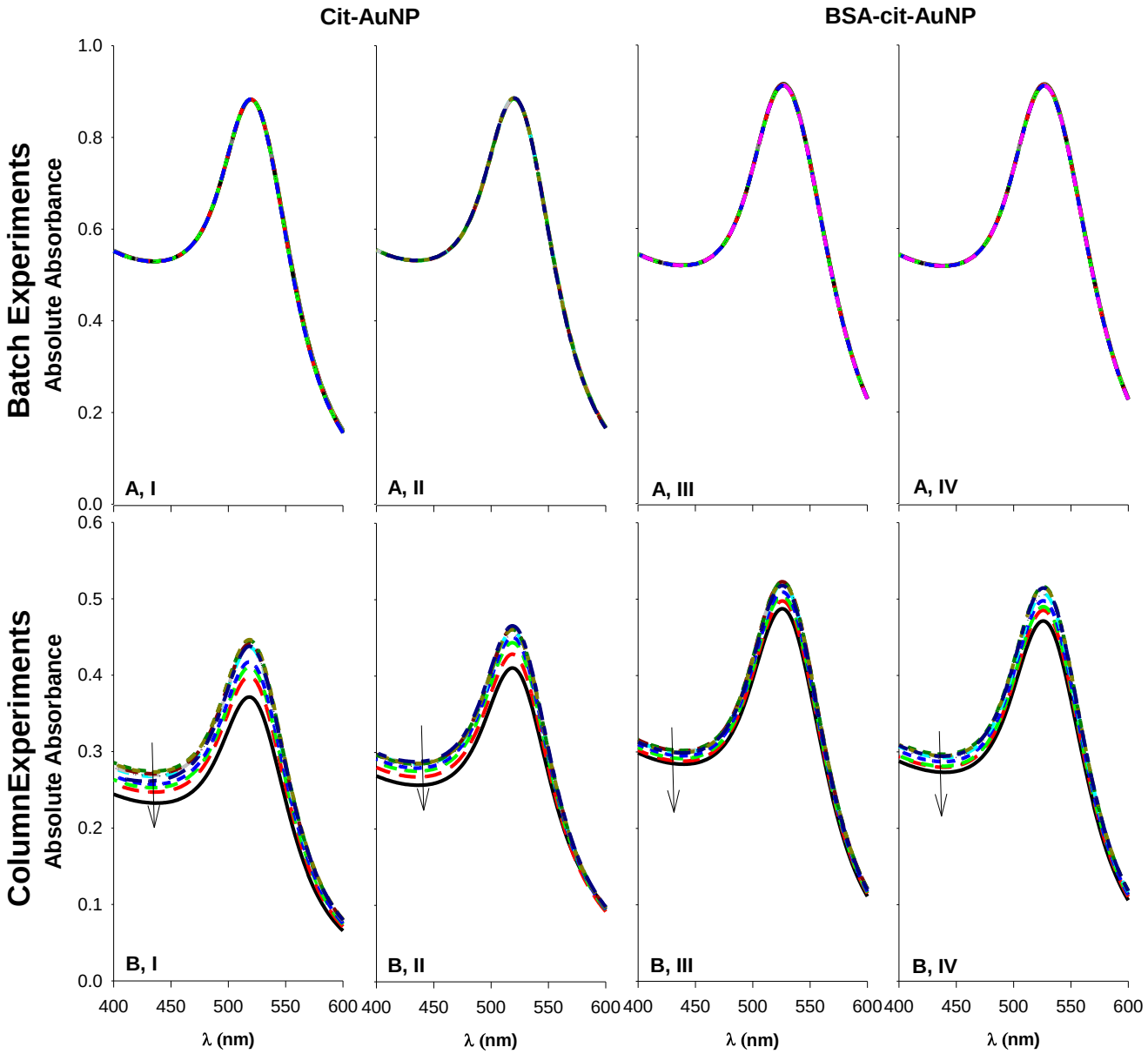

Figure A-6 – Comparison of UV-Vis spectra for batch and column experiments in the presence of $CaCl_2$. As labeled, the four graphs on the left are for cit-AuNP, while the plots on the right are for BSA-cit-AuNP. Plots labeled A in the top row are batch results; B in the bottom row are column data. NaCl concentrations: I = 0.1 mM, II = 0.6 mM, III = 0.1 mM, IV = 0.5 mM. The batch data were obtained over a timeframe relevant to the 'plateau' retention times in the column. The column data were obtained for V_{pore} values representative of the 'plateau' in the breakthrough curve. Arrows indicate time progression.

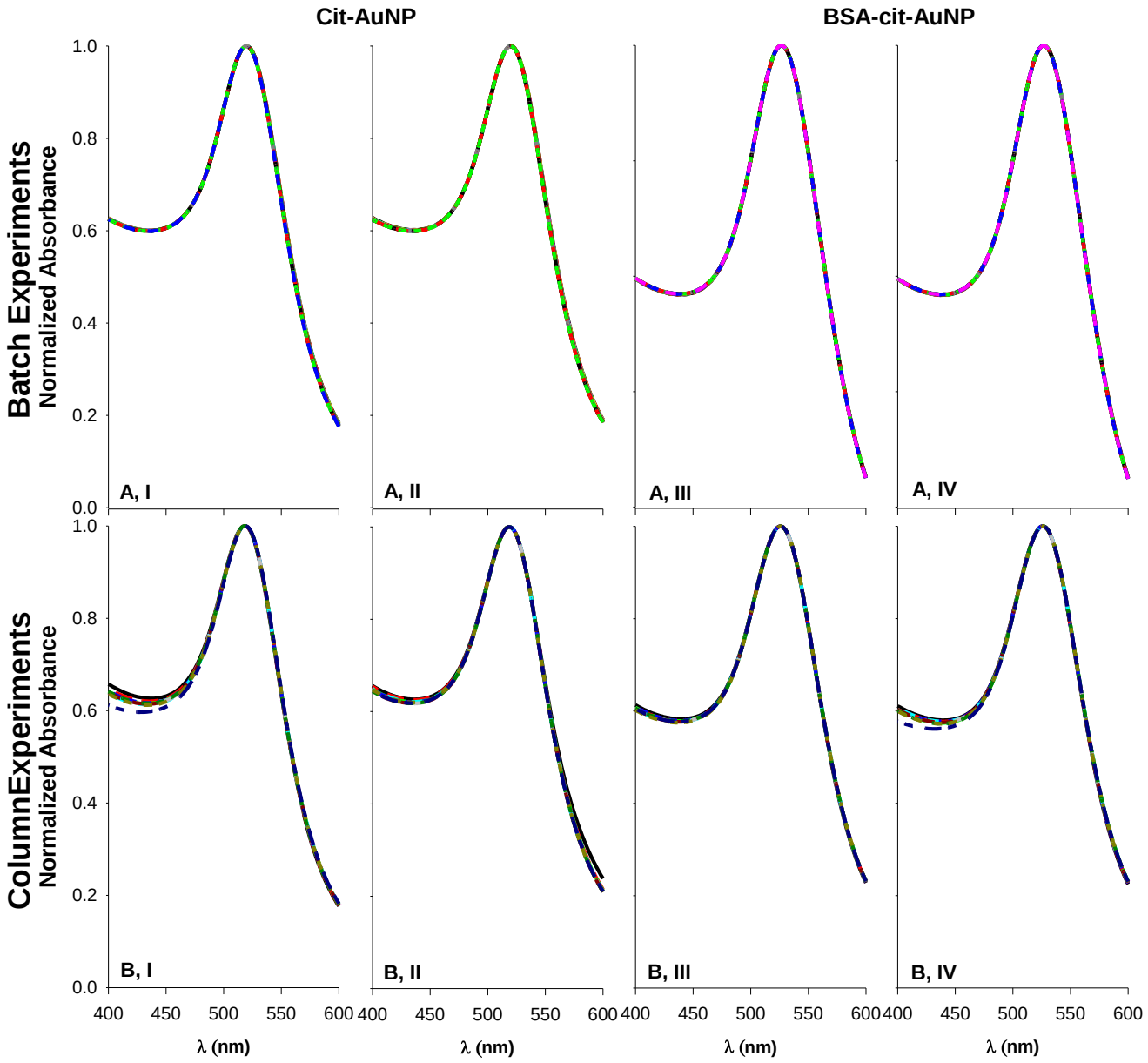

Figure A-7 – Comparison of UV-Vis spectra for batch and column experiments in the presence of $CaCl_2$. As labeled, the four graphs on the left are for cit-AuNP, while the plots on the right are for BSA-cit-AuNP. Plots labeled A in the top row are batch results; B in the bottom row are column data. NaCl concentrations: I = 0.1 mM, II = 0.6 mM, III = 0.1 mM, IV = 0.5 mM. The batch data were obtained over a timeframe relevant to the 'plateau' retention times in the column. The column data were obtained for V_{pore} values representative of the 'plateau' in the breakthrough curve. All data points were normalized against the maxima.

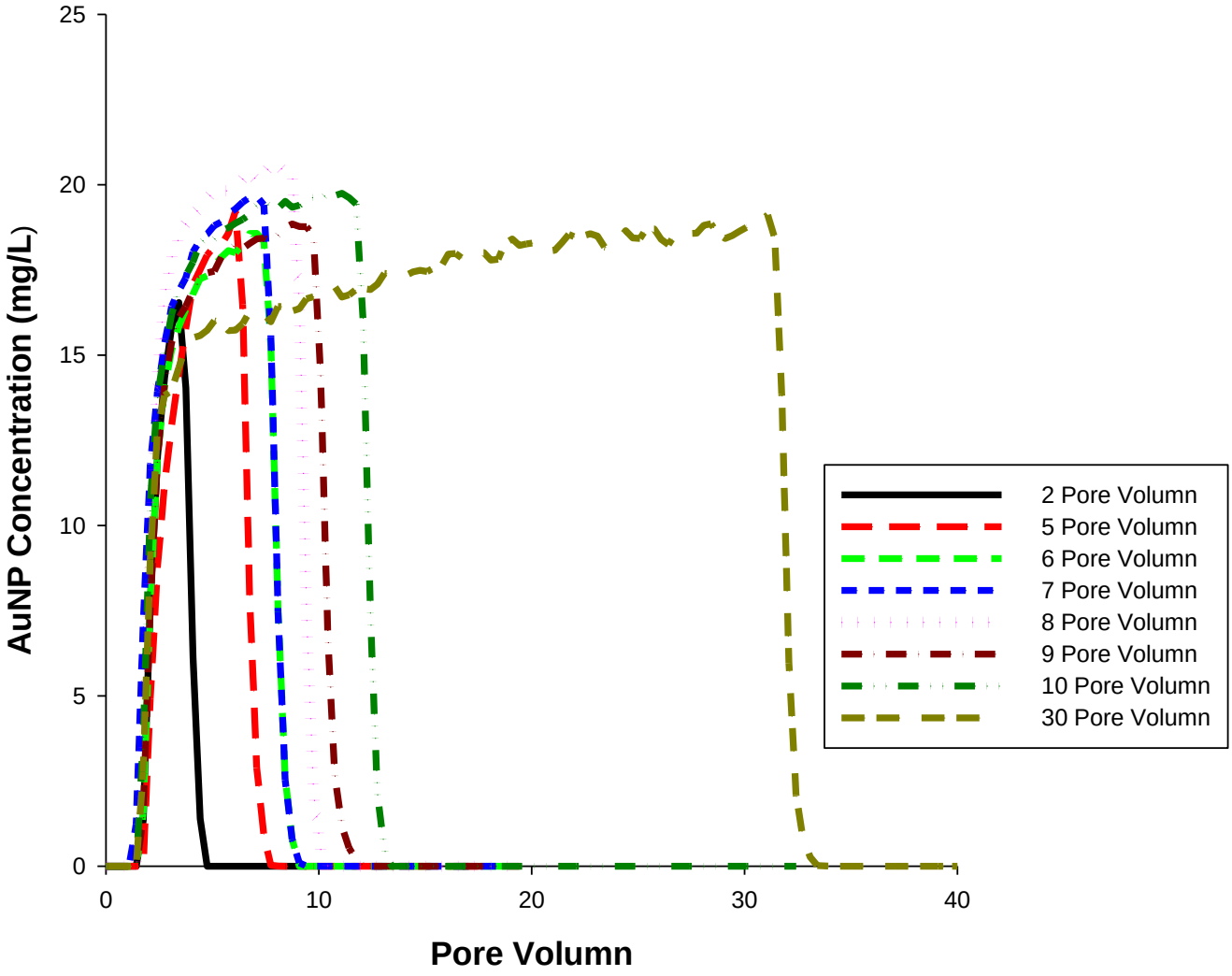

Figure A-8 – Breakthrough curves with varying injection volumes. All data collected at 30 mM NaCl. Note the sloping plateaus for all breakthrough curves.

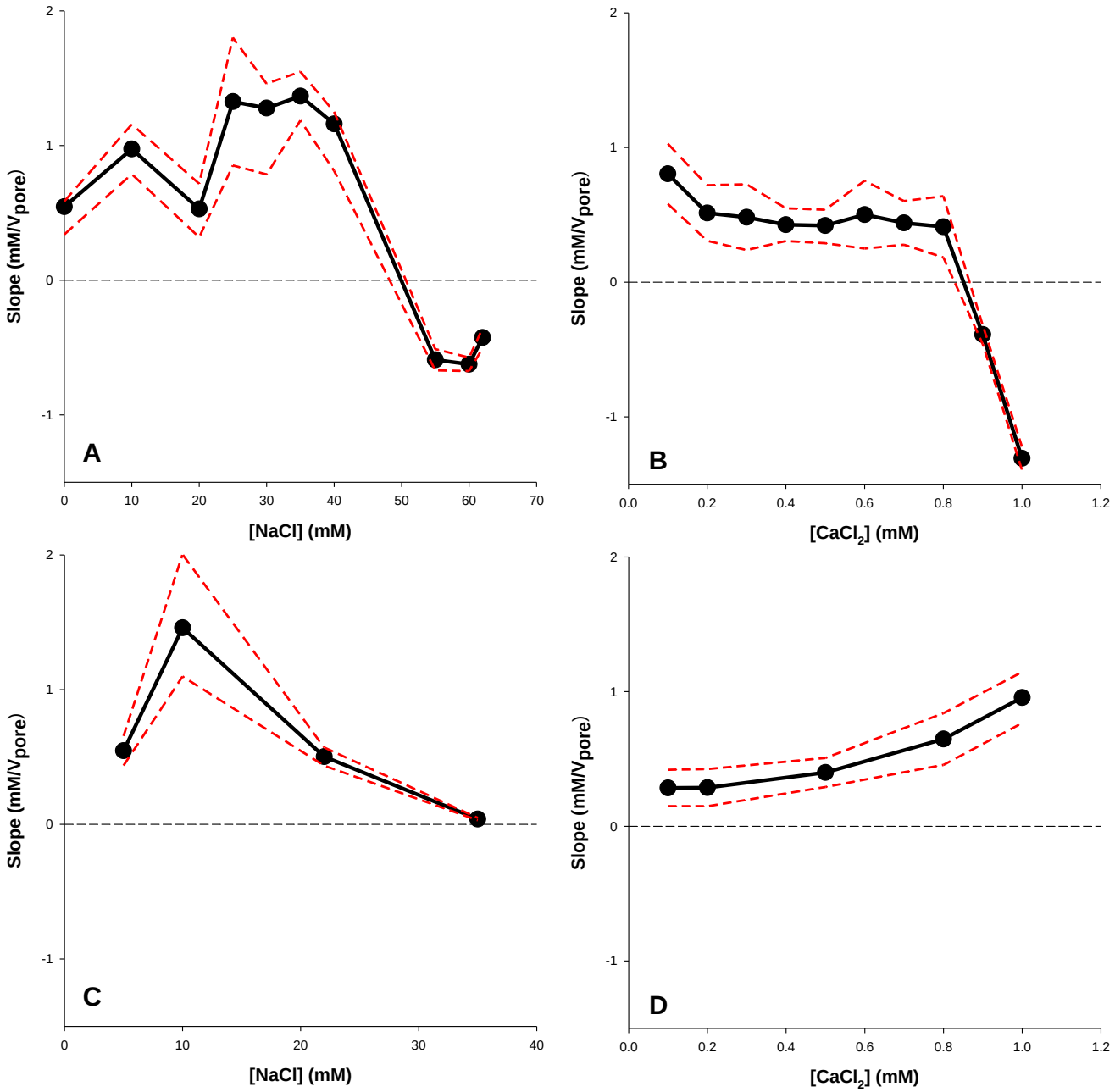

Figure A-9 – Calculated slopes for the 'plateau' region of the column breakthrough curves for cit-AuNP in the presence of A) NaCl and B) $CaCl_2$ and for BSA-cit-AuNP in the presence of C) NaCl and D) $CaCl_2$. Dashed-lines denote the 95% confidence interval for each calculated slope.

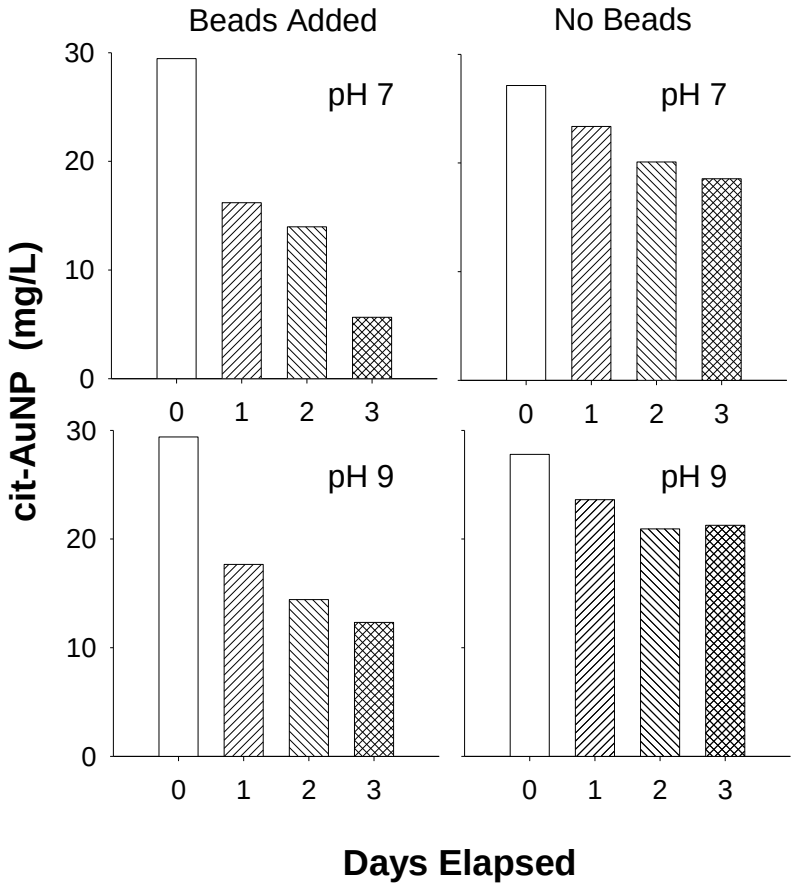

Figure A-10 – Batch experiment examining cit-AuNP aggregation in the presence of glass beads. The summarized results are for reactors containing 10 mM NaCl and cit-AuNP (C_0 = 30 mg/L) at pH 7 and pH 9 (this pH range bounds the column pH). The control reactors contained no glass beads, while the experimental reactors contained 10 g of glass beads. UV-Vis at 520 nm was used to determine the AuNP concentration on each day. As observed, the cit-AuNP concentration for the reactors with beads present decreased much more rapidly with time than the control reactors (no beads). This result is an indication that there is an interfacial interaction between the AuNP and the glass bead surface that can induce accelerated aggregation relative to that observed in the absence of the beads. We emphasize that the timescale of these experiments was considerably larger than that of the retention times in the columns and thus the kinetics observed in this experiment should not be construed as representative of the aggregation kinetics in the column.

A.1 Attachment efficiency calculations

To understand the mechanism(s) governing AuNP retention in the columns, the single-cell filtration attachment efficiency was calculated:[1]

$$\alpha = -\ln\left(\frac{C}{C_0}\right)\frac{(4a_c)}{3(1-\epsilon)\eta_0 L} \quad (1)$$

Where C is the plateau concentration of a given AuNP breakthrough curve, C_0 is the initial inflow concentration, a_c is the glass bead radius, ε is the packed column porosity, L is the length of the packed bed, and η_0 is the collector efficiency as calculated using the correlation of Tufenkji and Elimenech.[2]

Each calculated α denotes the ratio between AuNP that successfully made collision with a glass bead and those that remained attached after the collision.[3,4] Therefore, α=1 indicates that all collisions between AuNP and the glass bead surface led to attachment. When calculating α using equation 1 the collection efficiency (η_0) is of particular interest because it encompasses the physical parameters pertinent to transport within the column. These parameters include Brownian diffusion, gravitational sedimentation, and interception (advection).[2] Tufenkji and Elimelech developed a vigorous correlation to calculate this parameter:

$$\eta_0 = \eta_D + \eta_I + \eta_G \quad (2)$$

where η_D accounts for diffusion, η_I for advection and η_G for gravitational effects. Equation (2) expands:

$$\eta_0 = 2.4A_S^{1/3}N_R^{-0.081}N_{Pe}^{-0.715}N_{vdW}^{-0.052} + 0.55A_S N_R^{1.675}N_A^{0.125} + 0.22N_R^{-0.24}N_G^{1.11}N \quad (3)$$

where A_S is the porosity parameter; N_R is the aspect ratio between the porous media and the AuNP; N_{Pe} is the Péclet number; N_G is a dimensionless gravity parameter, N_A is a dimensionless parameter accounting for the attraction between AuNP and the porous media, and N_{vdW} is a dimensionless parameter accounting for van der Waals interactions. These parameters are in turn defined as:

$$A_S = \frac{2(1-\gamma^5)}{2-3\gamma+3\gamma^5-2\gamma^6} \qquad \gamma = (1-f)^{1/3} \tag{4}$$

$$N_R = \frac{d_p}{d_c} \tag{5}$$

$$N_{Pe} = \frac{U d_c}{D_\infty} \tag{6}$$

$$N_G = \frac{2}{g}\frac{a_p^2(\rho_p-\rho_f)g}{\mu U} \tag{7}$$

$$N_A = \frac{A}{12\pi\mu a_p^2 U} \tag{8}$$

$$N_{vdW} = \frac{A}{kT} \tag{9}$$

where f is porosity, d_p is the AuNP diameter, d_c is the glass bead diameter, U is the fluid approach velocity, D_∞ is the bulk diffusion coefficient as determined by the Stokes-Einstein equation, A is the Hamaker constant, k is the Boltzmann constant, T is the fluid temperature in K, a_p is the radius of the AuNP, ρ_p is the AuNP density, ρ_f is the fluid density, μ is the absolute fluid viscosity, and g is the gravitational acceleration. Using the parameters listed in Table A-2, the individual dimensionless terms in Equation (3) were calculated for the present system (Table A-3).

Table A-2 – Input parameters for the calculation of the collector efficiency (η_0)

Boltzmann constant (k_B)	1.38×10^{-23} J/K
Gravitational acceleration (g)	9.81 m/s^2
Particle diameter (d_p)	14 nm
Particle radius (a_p)	7 nm
Collector diameter (d_c)	250 μm
Approach velocity of fluid (U)	2.36×10^{-4} m/s
Hamaker constant (A)	3.2×10^{-20} J (obtained from literature[5])
Temperature (T)	298 K
Particle density (ρ_p)	19.3 g/cm^3
Fluid density (ρ_f)	0.9998 g/cm^3
Absolute (dynamic) viscosity of fluid (μ)	0.0009 N·s/m^2
Porosity (f)	0.34
Gamma (γ)	0.871
Porosity-dependent parameter (A_s)	56.39

Table A-3 – Dimensionless parameters for the calculation of collector efficiency (η_0)

N_R	5.60×10^{-5}
N_{Pe}	1.70×10^{3}
N_{vdW}	7.78
N_A	1.67×10^{18}
N_G	9.22×10^{-9}

Combining Table A-3 and Equation (3), $\eta_0 = 0.111$. It is important to note that the terms related to Brownian diffusion in Equation (3) essentially dominate η_0, such that for this study:

$$\eta_0 \cong 2.4 A_S^{1/3} N_R^{-0.081} N_{Pe}^{-0.715} N_{vdW}^{-0.052} \quad (10)$$

A.2 DLVO calculations

Classic DLVO theory states that the interaction between colloidal surfaces is comprised of the Lifshitz-van der Waals (LW) interaction and the electrostatic (EL) interaction.[6] This in practice can be expressed formally as:

$$U_{123}^{DLVO} = U_{123}^{LW} + U_{123}^{EL} \quad (11)$$

where U_{123}^{DLVO} is the total interaction energy between surfaces 1 and 3 suspended in liquid media 2, U_{123}^{LW} and U_{123}^{EL} are the energy contributions from the Lifshitz-van der Waals interaction and the electrostatic interaction, respectively.

The Lifshitz-van der Waals interaction accounts for electrodynamic interactions between surfaces in aqueous media, these include the dispersion due to dipole interactions between surfaces, the change in orientation due to dipole interactions, and the dispersion of surfaces in the media via dipole interactions.[7] In particular, these include the forces between two permanent dipoles, the forces between a permanent dipole and a corresponding induced dipole, and the forces between two instantaneously induced dipoles (e.g., London dispersion forces).[8] When considering the interaction between a single

AuNP and a grain of porous media in the column, it is reasonable to approximate such interactions to be between a perfect sphere and an infinitely long plate. This approximation is appropriate because relative to the size of an AuNP, the glass bead grain is much larger, effectively functioning like a flat plane. Derjaguin provided an approximation for U_{123}^{LW} as follows:

$$U_{123}^{LW} = -\left(\frac{Aa_p}{6h}\right)\left(1 + \frac{14h}{\lambda}\right)^{-1} \quad (12)$$

where A is the Hamaker constant for the surfaces that are interacting (in this case AuNP and glass); a_p is the radius of the AuNP, h is the distance between the interacting surfaces, and λ is the characteristic wavelength of the dielectric, which is typically estimated to be 100 nm.[6]

To evaluate whether there was significant aggregation between nanoparticles, the above approximation cannot be used. Geometrically the interaction between two spherical AuNP of similar size is very different from the interaction between a spherical particle and a flat plane.[9] As such, a different approximation is used:

$$U_{121}^{LW} = -\left(\frac{A}{6}\right)\left\{\left[\frac{2a_p^2}{h(4a_p + h)}\right] + \left[\frac{2a_p^2}{2(a_p + h)^2}\right] + \ln\left[\frac{h(4a_p + h)}{(2a_p + h)^2}\right]\right\} \quad (13)$$

In order for a colloidal suspension to remain stable according to DLVO theory, there must be an opposing interaction counteracting the Lifshitz-van der Waals attraction. In DLVO theory, the total interaction energy between two surfaces suspended in a medium also accounts for the electrostatic interactions between those two surfaces. Modeling electrostatic interactions is very complex, and usually simplifications must be made for the approximation. Common approximations usually either hold the electric potential of the surfaces to be constant, or the electric charge of the surfaces to be constant.[10] The model used here was developed by Hogg *et al.*, which assumes constant surface potential between a spherical particle and an infinitely flat plane.[11] The expression is as follows:

$$U_{123}^{EL} = \pi\varepsilon_r\varepsilon_0 a_p\left[2\zeta_1\zeta_3 \ln\left(\frac{1 + e^{-\kappa h}}{1 - e^{-\kappa h}}\right) + (\zeta_1^2 + \zeta_3^2)\ln(1 - e^{-2\kappa h})\right] \quad (14)$$

Where U_{123}^{EL} is the electrostatic interaction energy between surface 1 and surface 3 dispersed in medium 2; $\varepsilon_r\varepsilon_0$ is the dielectric permittivity of the suspending fluid (in this case, the value for water at 298 K was used; 6.95×10^{-10} F-m); a_p is the radius of the AuNP, ζ_1 and ζ_3 are the surface potentials of the interacting

surfaces (zeta potentials obtained from particle analyzer were used here); h is the distance between interacting surfaces; and κ is the inverse Debye length, which is defined as:

$$\kappa = \sqrt{\frac{e^2 \sum n_i z_i^2}{\varepsilon_r \varepsilon_0 kT}} \tag{15}$$

where e is the electron charge; n_i and z_i are the number concentration and valence of ion i. For the electrostatic interaction between two AuNP (assuming that both are perfect spheres), some simplification can be made:

$$U_{121}^{EL} = 2\pi \varepsilon_r \varepsilon_0 a_p \zeta_1^2 \ln(1 + e^{-\kappa h}) \tag{16}$$

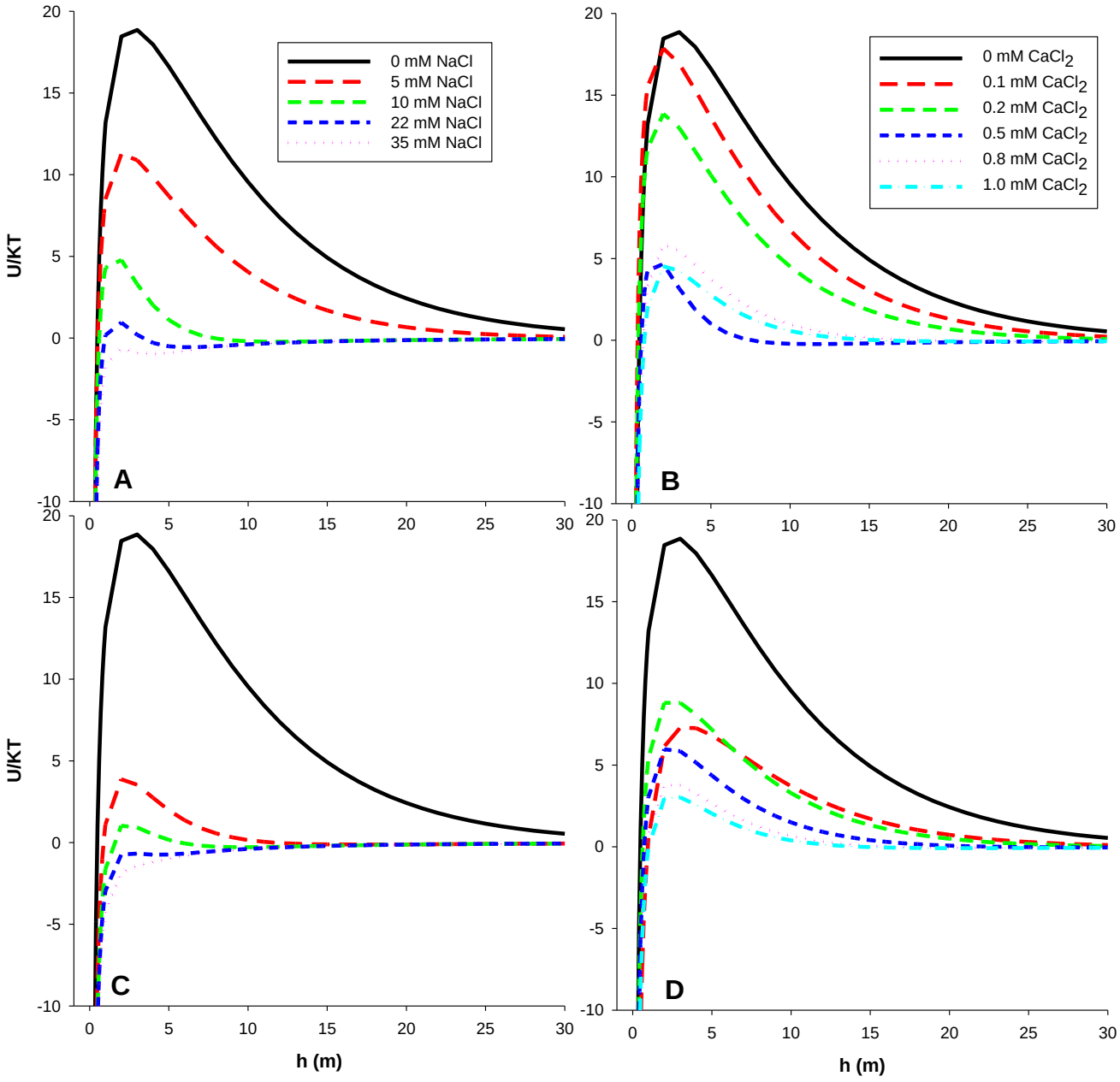

Figure A-11 – DLVO plot describing *deposition interaction* between AuNP and glass beads using equation (12) and (14). A.) cit-AuNP with increasing [NaCl]; B.) cit-AuNP with increasing [$CaCl_2$]; C.) BSA-cit-AuNP with increasing [NaCl]; and D.) BSA-cit-AuNP with increasing [$CaCl_2$].

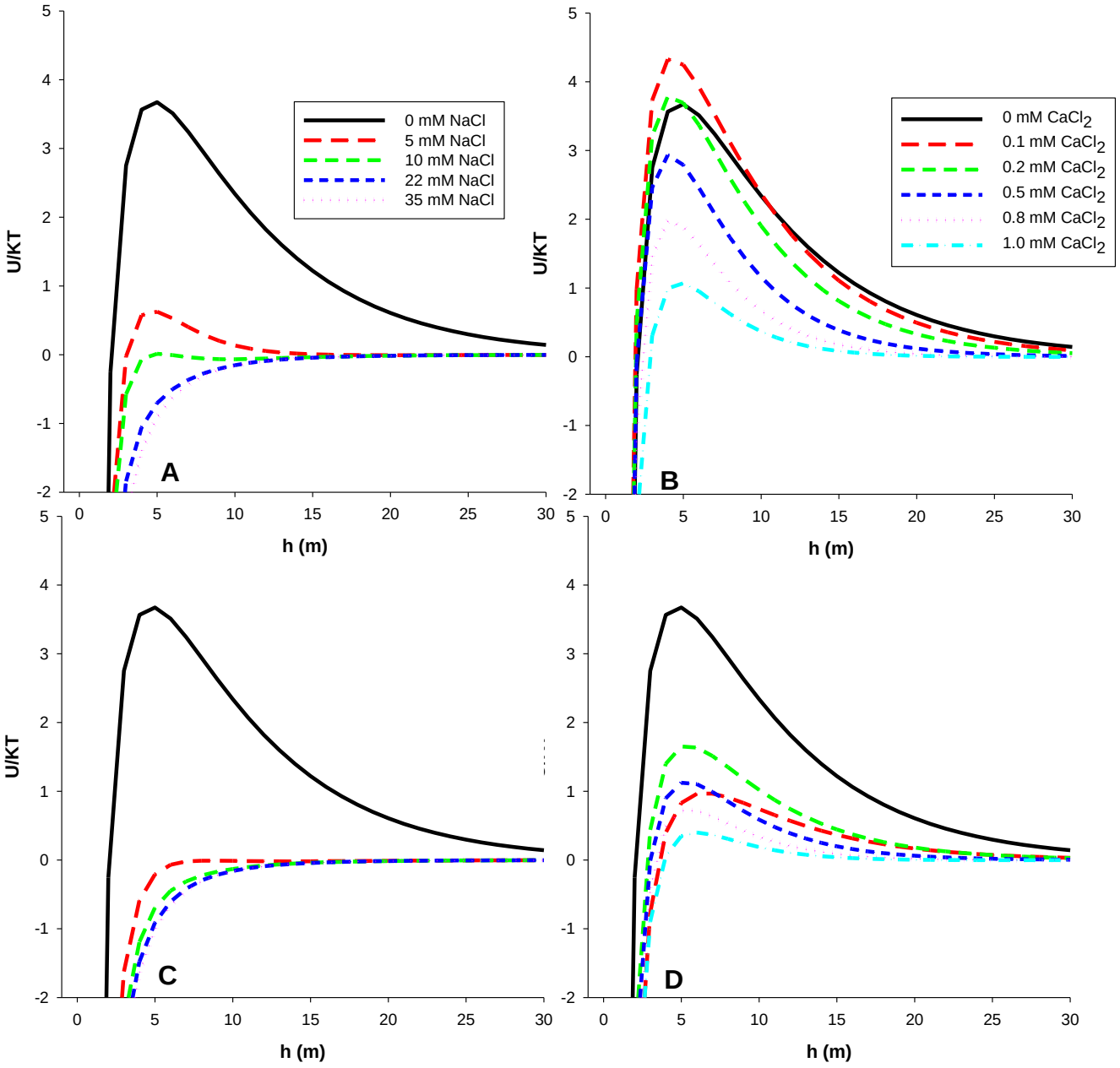

Figure A-12 – DLVO plot describing *aggregation interaction* between two AuNP using equation (13) and (16). A.) cit-AuNP with increasing [NaCl]; B.) cit-AuNP with increasing [$CaCl_2$]; C.) BSA-cit-AuNP with increasing [NaCl]; and D.) BSA-cit-AuNP with increasing [$CaCl_2$].

Derjaguin-Landau-Verwey-Overbeek (DLVO) theory was utilized to evaluate the possible connection between the low α values and AuNP aggregation within the porespace.[12,13] DLVO theory considers that colloidal interactions are comprised of Lifshitz-van der Waals (LW) and electrical double layer (EL) components.[6] As such, other interactions such as steric and hydrophobic interactions are not considered.

BSA is known to interact in ways that are not accounted for in DLVO theory.[14] Therefore, DLVO does not encapsulate the entire system of interactions for the experiments involving BSA-cit-AuNP. Nonetheless, DLVO theory can be used to provide a qualitative exploration of the interacting surfaces. Herein a comparison of the calculated energy barriers for both deposition and aggregation is presented, while detailed DLVO plots for each dataset are illustrated in Figure A-12 & A-13.

Several observations about the calculated DLVO repulsive energy barrier heights are notable (Figure A-13). First of all, the calculated energy barriers in Figure A-13A are all within the range of values

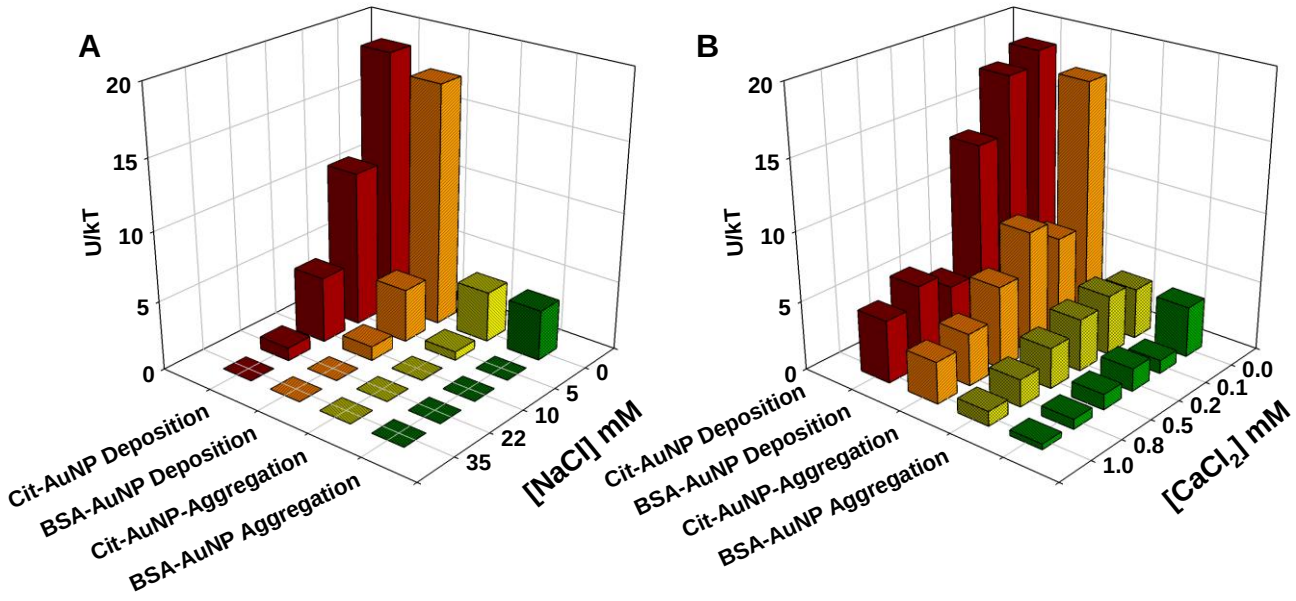

Figure A-13 – DLVO energy barrier height normalized by kT (T=298 K), where the deposition (AuNP onto glass bead) and aggregation (AuNP on AuNP) energy barriers are compared side by side. Figure A-13A and A-13B provides the energy barrier heights from the NaCl experiments and the $CaCl_2$ experiments, respectively.

reported in Figure A-13B. This observation confirms that although the concentration ranges used for NaCl and $CaCl_2$ were about an order of magnitude apart, they provided very similar interaction energies. Secondly, comparison of the repulsive energy barrier for cit-AuNP and BSA-cit-AuNP only partially reflects the experimental results. In Figure A-13A, the repulsive energy barrier for BSA-cit-AuNP deposition decreases much more rapidly than for cit-AuNP, corroborating the experimental observations.

This substantial decrease in the magnitude of the energy barrier suggests that the counter ion screening effects of NaCl dominate over the electrosteric stabilization that results from the BSA layer thus resulting in deposition/aggregation. For the BSA-cit-AuNP column experiments with $CaCl_2$, the DLVO repulsive barrier remains present at higher $CaCl_2$ concentrations (Figure A-13B), which correlates with the stability of BSA-cit-AuNP under those conditions. However, the DLVO calculations in Figure A-13B indicate that the energy barrier for BSA-cit-AuNP deposition was smaller in magnitude than that of cit-AuNP. The decreased magnitude of the BSA-cit-AuNP deposition energy barrier is a further indication that the stabilizing effect of BSA is neither electrostatic nor double layer related, and therefore is not reflected in classic DLVO calculations.

When considering the calculated energy barriers for aggregation, an immediate observation was that the aggregation energy barriers were much lower than those for deposition. The energy barrier for deposition was as high as 20 kT, while for aggregation the maximum height of the interaction energy was ≈4.5 kT. Furthermore, the locations of the energy barriers were also different. For deposition, the maximum energy barrier is located at ≈2 nm; while for aggregation, the barrier is located at ≈5 nm (see Figure A-12 & A-13). The difference in barrier location and height implies that the nanoparticles may have greater propensity to aggregate than to deposit. Another important finding from this comparison was that even small amounts of NaCl can decrease the energy barrier for BSA-cit-AuNP to the point that it no longer exists. From a DLVO standpoint, even at the lowest experimental concentration of NaCl, there was no repulsive double layer interaction preventing nanoparticle aggregation. In the presence of $CaCl_2$ BSA-cit-AuNP exhibits a decreased energy barrier, but the barrier remains. At the higher end of the experimental NaCl concentrations, the lack of a calculated repulsive interaction suggests the potential for aggregation of BSA-cit-AuNP within the porespace of the packed column.

We reiterate that classic DLVO cannot be used to quantitatively describe everything happening in these experiments, since it only considers one-to-one interactions and does not take into account the electrosteric effects of the BSA layer on an AuNP. Another major limitation of the DLVO calculation

was that it assumes the sizes of the AuNP stay constant. This assumption cannot be true if aggregation is occurring, which, as shown by the batch experiment did occur. If aggregates of nanoparticles are considered to be larger "particles", their deposition (and possibly further aggregation) interactions and energetics may or may not deviate from the DLVO calculations described here.[15,16]

Disclosure

This work has been published by the American Chemical Society: Chan, M. Y.; Vikesland, P. J., Porous Media-Induced Aggregation of Protein-Stabilized Gold Nanoparticles. *Environ. Sci. Technol.* **2014,** *48*, (3), 1532-1540.

References

(1) Yao, K.-M.; Habibian, M. T.; O'Melia, C. R., Water and waste water filtration. Concepts and applications. *Environ. Sci. Technol.* **1971,** *5*, (11), 1105-1112.

(2) Tufenkji, N.; Elimelech, M., Correlation Equation for Predicting Single-Collector Efficiency in Physicochemical Filtration in Saturated Porous Media. *Environ. Sci. Technol.* **2004,** *38*, (2), 529-536.

(3) Lecoanet, H. F.; Bottero, J.-Y.; Wiesner, M. R., Laboratory Assessment of the Mobility of Nanomaterials in Porous Media. *Environ. Sci. Technol.* **2004,** *38*, (19), 5164-5169.

(4) Elimelech, M., Effect of Particle Size on the Kinetics of Particle Deposition under Attractive Double Layer Interactions. *J. Colloid Interface Sci.* **1994,** *164*, (1), 190-199.

(5) Bergström, L., Hamaker constants of inorganic materials. *Adv. Colloid Interface Sci.* **1997,** *70*, 125-169.

(6) Bottero, J.-Y.; Wiesner, M. R., *Environmental nanotechnology: applications and impacts of nanomaterials*. McGraw-Hill Professional: 2007; p 553.

(7) Israelachvili, J. N., *Intermolecular and Surface Forces*. 3rd ed ed.; Academic Press: Burlington, MA, 2011; p 674.

(8) van der Waals forces. In *IUPAC Compendium of Chemical Terminology*, 2.1.0 ed.; Nič, M.; Jirát, J.; Košata, B.; Jenkins, A.; McNaught, A., Eds. IUPAC: Research Triagle Park, NC.

(9) van Oss, C. J., *Interfacial Forces in Aqueous Media, Second Edition*. 2 ed.; CRC Press: 2006; p 456.

(10) Hunter, R. J., *Foundations of Colloid Science*. 2nd ed ed.; Oxford University Press: Oxford, 2001; p 806.

(11) Hogg, R.; Healy, T. W.; Fuerstenau, D. W., Mutual coagulation of colloidal dispersions. *Trans. Faraday Soc.* **1966,** *62*, 1638-1651.

(12) Derjaguin, B. V.; Landau, L., Theory of the stability of strongly charged lyophobic sols and the adhesion of strongly charged particles in solutions of electrolytes. *Acta Physicochim. URSS* **1941,** *14*, 633-662.

(13) Verwey, E. J. W.; Overbeek, J. T. G., *Theory of the Stability of Lyophobic Colloids*. Courier Dover Publications: 1999; p 228.

(14) Chou, D.; Morr, C., Protein-water interactions and functional properties. *J. Am. Oil Chem. Soc.* **1979,** *56*, (1), A53-A62.

(15) Lin, S.; Wiesner, M. R., Exact Analytical Expressions for the Potential of Electrical Double Layer Interactions for a Sphere−Plate System. **2010,** *26*, (22), 16638-16641.

(16) Lin, S.; Wiesner, M. R., Deposition of Aggregated Nanoparticles — A Theoretical and Experimental Study on the Effect of Aggregation State on the Affinity between Nanoparticles and a Collector Surface. *Environ. Sci. Technol.* **2012,** *46*, (24), 13270-13277.

Appendix B. Supporting Information for Chapter 3

B.1 Experimental Procedures

B.1.1 Gold SERS Substrate Experimental Procedures

A commercial gold SERS substrate (Klarite®, Renishaw Diagnostics, Hoffman Estates, IL) was used to determine the fundamental SERS response of halides associated with a pristine gold surface. In these experiments, ≈0.5 μL aliquots of 1 mM salt (NaF, NaCl, NaBr, or NaI) were added to isolated regions of the substrate and then air-dried. Sample regions were analyzed using a confocal Alpha500R Raman spectrometer (WITec; Ulm, Germany) and a 10× objective. A 785 nm laser operating at 9.65 mW with an integration time of 0.1 s was used to acquire 100 × 100 μm^2 scans. The areal resolution was 50×50. The area under the Raman band from 170-350 cm^{-1} was integrated to form 2D chemical image maps (Figure B-1). The maps were averaged using the onboard WITec software to generate an overall Raman spectrum.

B.1.2 Citrate-coated Nanoparticle Suspension Experimental Procedures and Particle Characterizations

SERS experiments were also performed using in house synthesized citrate-coated gold nanoparticle (cit-AuNP) suspensions. These particles were extensively characterized: transmission

electron microscopy-determined diameter of 16 ± 1.2 nm (n = 200), hydrodynamic diameter of 19.0 ± 0.41 nm determined by dynamic light scattering, and a zeta potential of -38.4 ± 1.00 mV (Figure B-2).[1] An AuNP suspension was mixed with an aliquot of NaX to produce suspensions with a desired salt concentration. These salt-treated AuNP suspensions were immediately injected into a 1 mm path length quartz cell (Starna, Atascadero, CA). SERS spectra were collected within the cell over a 200 μm × 50 μm areal scan at 20 × 5 resolution. All 100 SERS spectra that resulted from a scan were averaged via the onboard software to produce a single representative SERS spectrum for a given time point.

B.1.3 $HAuCl_4$ Raman Control Experiments

To verify that our results stem from halide interactions with the gold surface, we measured the Raman spectrum of concentrated $HAuCl_4$ solution at 20 mM (Figure B-3). Under these conditions the scattering path length is long enough that the stretching and planar deformation of the dissolved $AuCl_4^-$ complex in solution generates sufficient Raman signal to be detectable without surface enhancement. As expected, we observed the Raman bands reported by Loo in this $HAuCl_4$ control.[2] The Raman band at 173 cm^{-1} corresponds to the $\nu_4(B_{1g})$ vibrational mode (the in-plane deformation of square planar $AuCl_4^-$), the 324 cm^{-1} band to the $\nu_2(B_{2g})$ vibrational mode (in-plane banding or "scissoring"), and the 348 cm^{-1} band to $\nu_1(A_{2g})$ (symmetrical stretching).[2,3] The results from this experiment shows that none of the bands observed in our $HAuCl_4$ control were observed in our halide SERS experiments, which corroborate our hypothesis that the bands observed in Figure 3-1 stem from the interaction between the dissolved halides and the gold surface. Under

our experimental conditions, insufficient quantities of gold complexes form or adsorb to the gold surface to be detectable.[4] Such a hypothesis is consistent with the understanding that gold primarily forms halide complexes under anodic potentials that lead to dissolution.[2,5-7] This relationship between applied potential and complexation behavior along with the data in Figure B-3 strengthens our conclusion that the Raman bands in Figure 3-1 originate from vibrational modes that occur adjacent to gold nanoaggregate surfaces that are detectable due to SERS enhancement and do not reflect conventional Raman signals that arise from dissolved Au complexes.

B.2 Supporting Figures

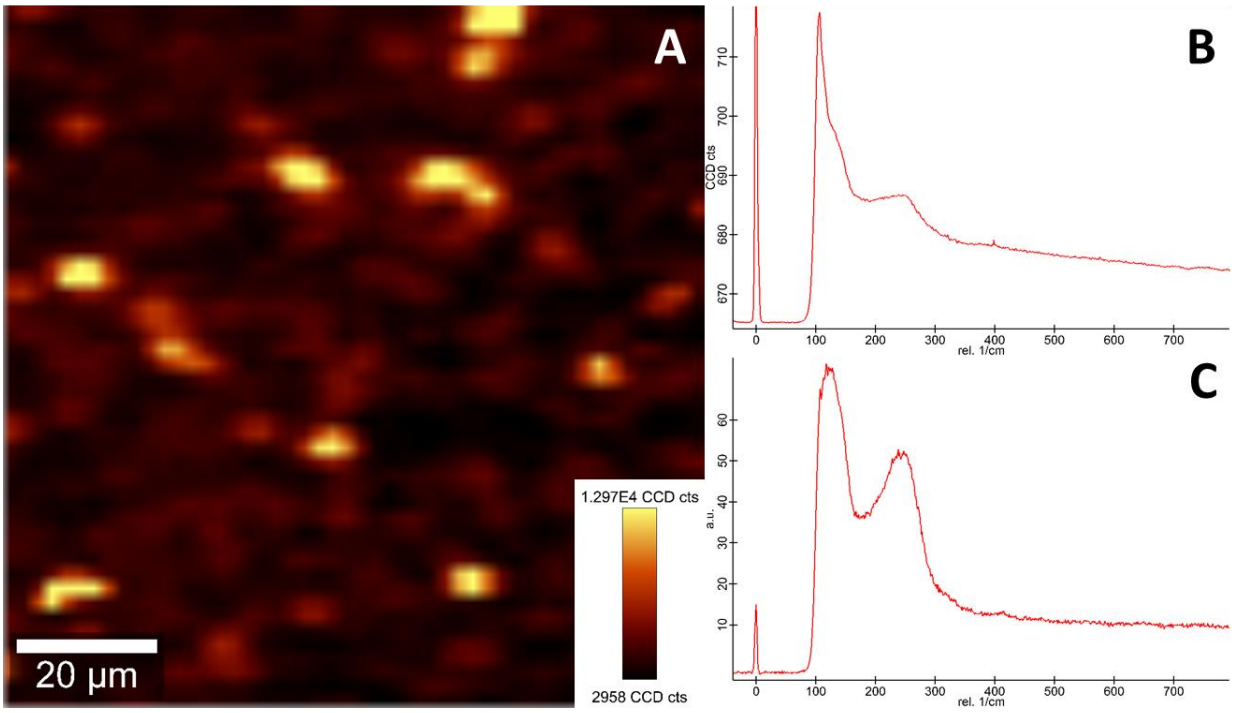

Figure B-1 – Sample 2D map from gold SERS substrate experiment with NaCl. A.) SERS map (170 cm^{-1} to 300 cm^{-1}) of gold substrate surface with dried NaCl droplet; B.) SERS spectrum from averaged the entire map from A; C.) Averaged SERS spectrum from B after background subtraction.

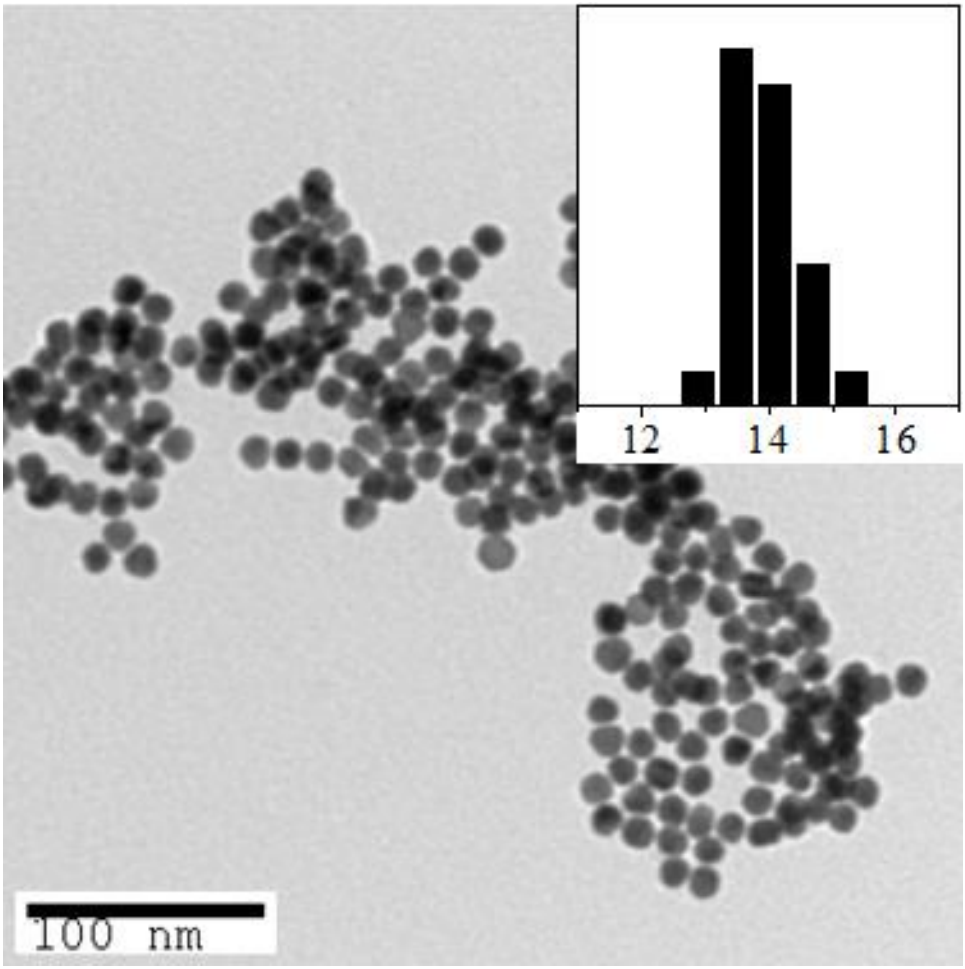

Figure B-2 – Citrate-coated gold nanoparticle characterization data. A Philips 420 TEM operating at 60 kV was used to determine size and morphology. Micrographs were analyzed using Image-J (National Institutes of Health) to quantify the AuNP core size. The electrophoretic properties of the AuNPs were measured using a Zetasizer NanoZS (Malvern Instruments) particle analyzer.

Table B-1 – Cit-AuNP characterization data summary.

LSPR (nm)	Concentration (NPs/mL)	TEM-determined diameter (nm)	Z_{avg} (nm) / PDI from DLS
519	6.54×10^{12}	13.9±0.5	17.7±0.8/0.03±0.01

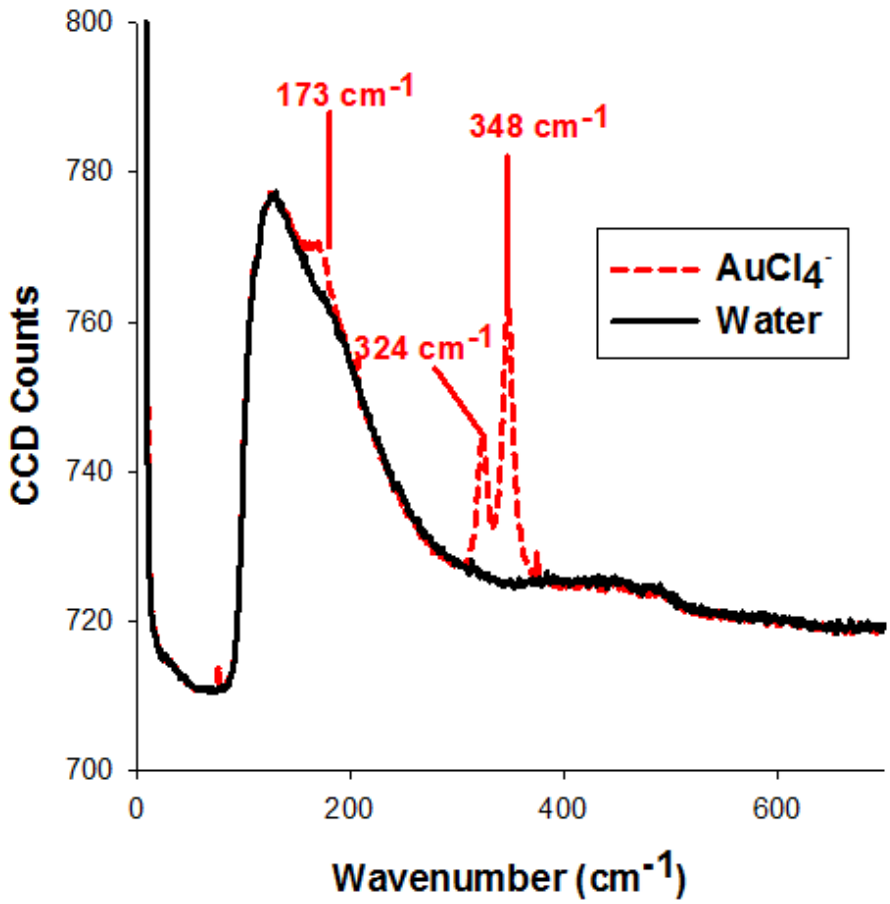

Figure B-3 – Raman spectra of a water control and 20 mM $HAuCl_4$ without any surface enhancement present. Note all three Raman bands from $AuCl_4^-$ (at 173 cm^{-1}, 324 cm^{-1}, and 348 cm^{-1}) corroborate values reported by Loo.[2]

Disclosure

This work is being prepared as a manuscript to be submitted to the German Chemical Society for consideration to be published as a Communication in the journal *Angewandt Chemie-International Edition*.

References

1. Turkevich, J.; Stevenson, P. C.; Hillier, J., A study of the nucleation and growth processes in the synthesis of colloidal gold. *Discuss. Faraday Soc.* **1951,** *11*.

2. Loo, B. H., In situ identification of halide complexes on gold electrode by surface-enhanced Raman spectroscopy. *J. Phys. Chem.* **1982,** *86*, (4), 433-437.

3. Harris, D. C.; Bertolucci, M. D., *Symmetry and spectroscopy: an introduction to vibrational and electronic spectroscopy*. Oxford University Press: New York, 1978; p xii, 550.

4. Gao, P.; Weaver, M. J., Metal-adsorbate vibrational frequencies as a probe of surface bonding: halides and pseudohalides at gold electrodes. *J. Phys. Chem.* **1986,** *90*, (17), 4057-4063.

5. Gaur, J. N.; Schmid, G. M., Electrochemical behavior of gold in acidic chloride solutions. *J. Electroanal. Chem. Interfacial Electrochem.* **1970,** *24*, (2–3), 279-286.

6. Cadle, S. H.; Bruckenstein, S., A ring-disk study of the effect of trace chloride ion on the anodic behavior of gold in 0.2 M H2SO4. *J. Electroanal. Chem. Interfacial Electrochem.* **1973,** *48*, (3), 325-331.

7. Gallego, J. H.; Castellano, C. E.; Calandra, A. J.; Arvia, A. J., The electrochemistry of gold in acid aqueous solutions containing chloride ions. *J. Electroanal. Chem. Interfacial Electrochem.* **1975,** *66*, (3), 207-230.

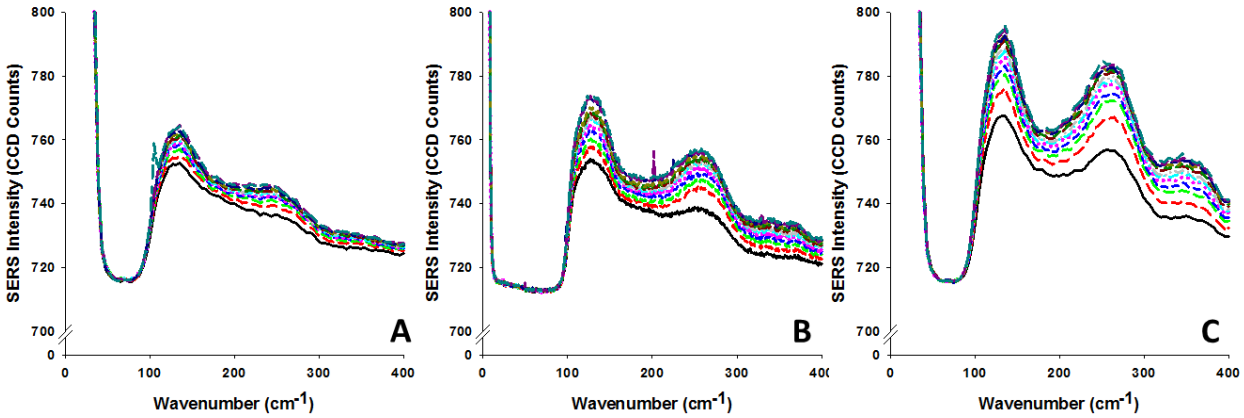

Figure C-1 – SERS spectra taken after salt addition to AuNP suspension at increasing time intervals superimposed onto the same graph. Black solid plots are at t = 1 min, each subsequent plot was taken starting at t = 5 min, and with increasing 5 min intervals up to 60 min. A.) 5 mM NaF; B.) 10 mM NaF; C.) 20 mM NaF. Note the presence and in some cases growth of the surface enhanced Rayleigh band present at ≈ 126 cm^{-1}.

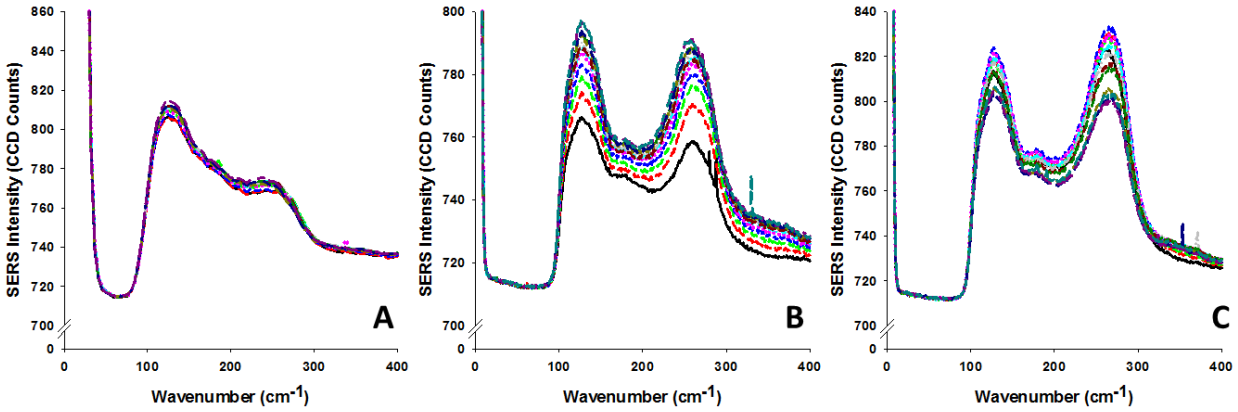

Figure C-2 – SERS spectra taken after salt addition to AuNP suspension at increasing time intervals superimposed onto the same graph. Black solid plots are at t = 1 min, each subsequent plot was taken starting at t = 5 min, and with increasing 5 min intervals up to 60 min. A.) 5 mM NaCl; B.) 10 mM NaCl; C.) 20 mM NaCl. N Note the presence and in some cases growth of the surface enhanced Rayleigh band present at ≈ 126 cm^{-1}.

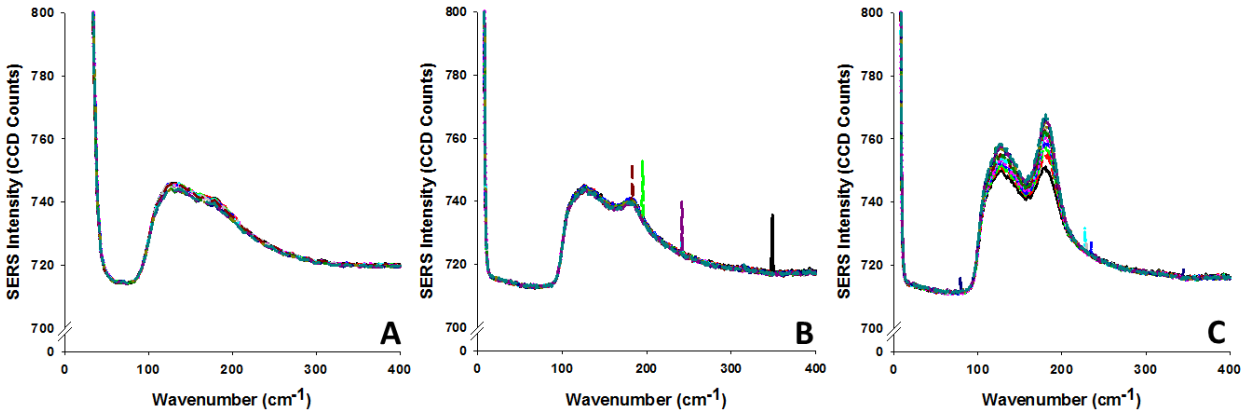

Figure C-3 – SERS spectra taken after salt addition to AuNP suspension at increasing time intervals superimposed onto the same graph. Black solid plots are at t = 1 min, each subsequent plot was taken starting at t = 5 min, and with increasing 5 min intervals up to 60 min. A.) 5 mM NaBr; B.) 10 mM NaBr; C.) 20 mM NaBr. Note the presence and in some cases growth of the surface enhanced Rayleigh band present at ≈ 126 cm^{-1}.

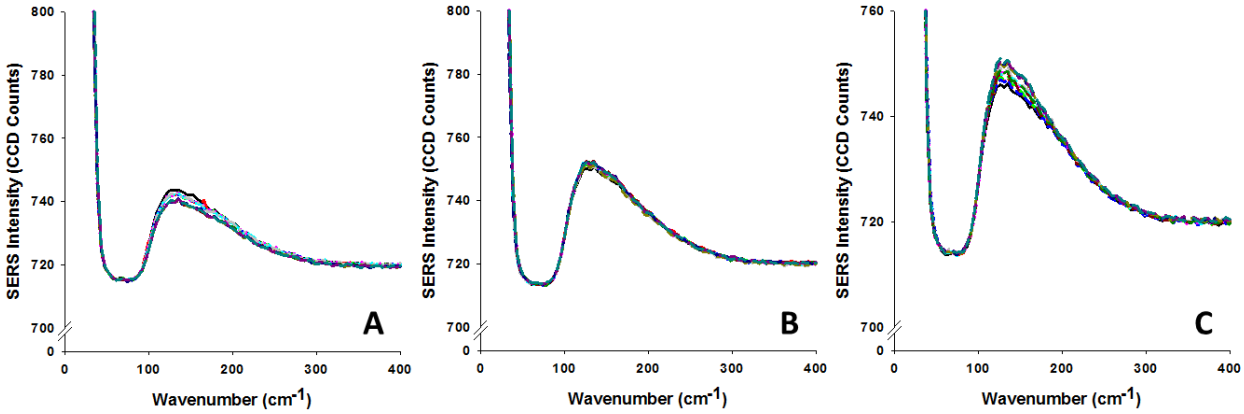

Figure C-4 – SERS spectra taken after salt addition to AuNP suspension at increasing time intervals superimposed onto the same graph. Black solid plots are at t = 1 min, each subsequent plot was taken starting at t = 5 min, and with increasing 5 min intervals up to 60 min. A.) 5 mM NaI; B.) 10 mM NaI; C.) 20 mM NaI. Note the presence and in some cases growth of the surface enhanced Rayleigh band present at ≈ 126 cm^{-1}.

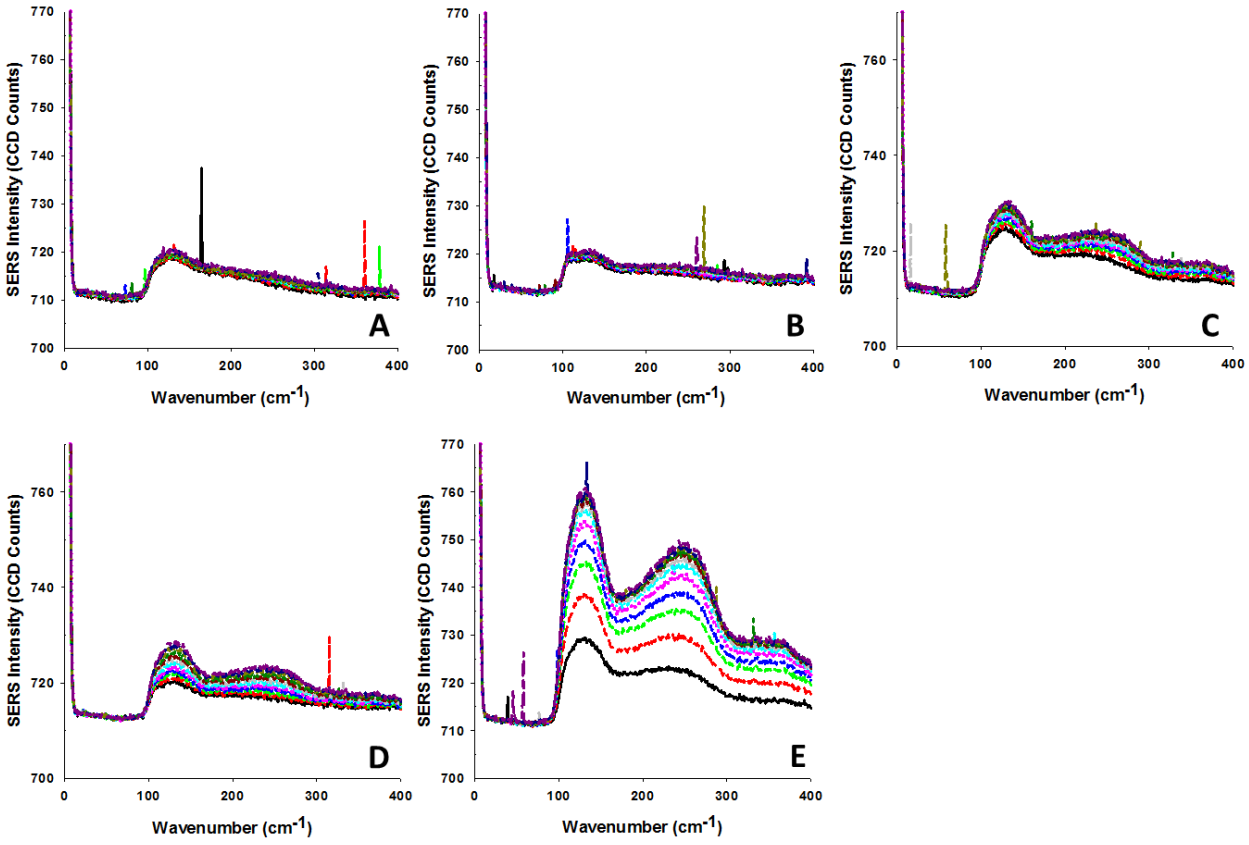

Figure C-5 – SERS spectra taken after salt addition to AuNP suspension at increasing time intervals superimposed onto the same graph. Black solid plots are at t = 1 min, each subsequent plot was taken starting at t = 5 min, and with increasing 5 min intervals up to 60 min. A.) 0.2 mM $CaCl_2$; B.) 0.5 mM $CaCl_2$; C.) 0.6 mM $CaCl_2$; D.) 0.8 mM $CaCl_2$; E.) 1.0 mM $CaCl_2$. Note the presence and in some cases growth of the surface enhanced Rayleigh band present at ≈ 126 cm^{-1}.

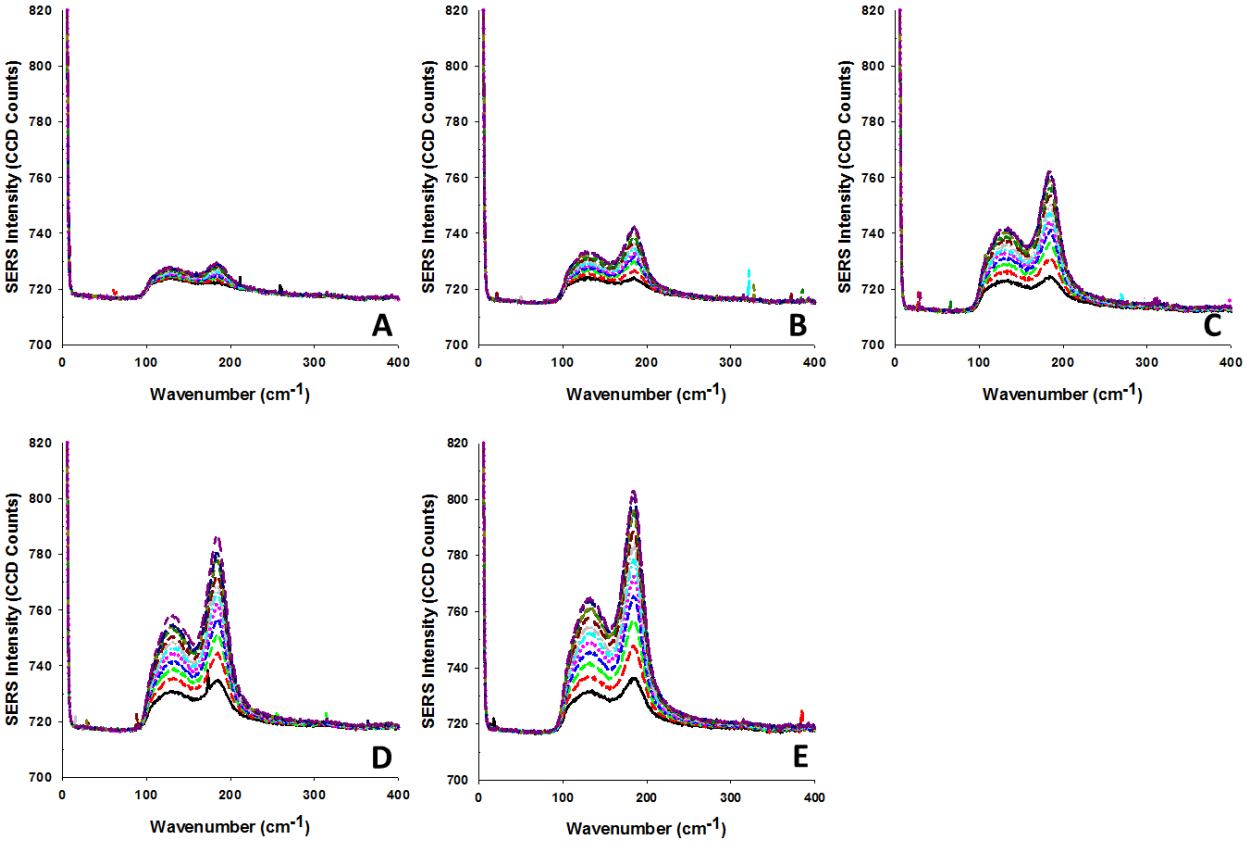

Figure C-6 – SERS spectra taken after salt addition to AuNP suspension at increasing time intervals superimposed onto the same graph. Black solid plots are at t = 1 min, each subsequent plot was taken starting at t = 5 min, and with increasing 5 min intervals up to 60 min. A.) 0.1 mM $CaBr_2$; B.) 0.2 mM $CaBr_2$; C.) 0.5 mM $CaBr_2$; D.) 0.8 mM $CaBr_2$; E.) 1.0 mM $CaBr_2$. Note the presence and in some cases growth of the surface enhanced Rayleigh band present at ≈ 126 cm^{-1}.

.

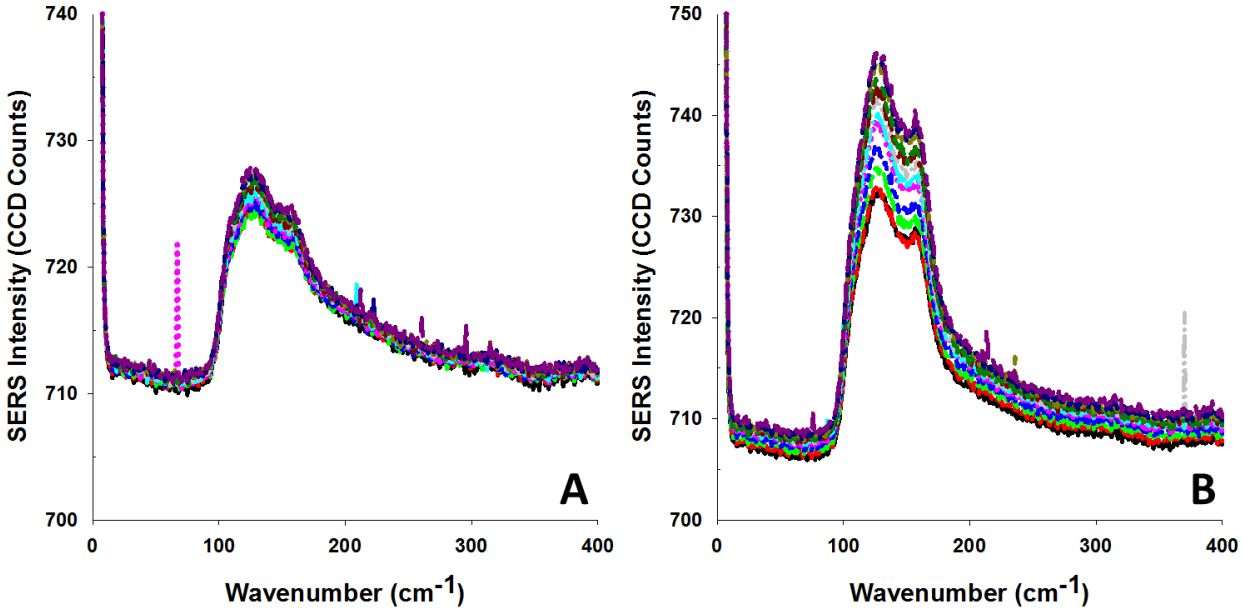

Figure C-7 – SERS spectra taken after salt addition to AuNP suspension at increasing time intervals superimposed onto the same graph. Black solid plots are at t = 1 min, each subsequent plot was taken starting at t = 5 min, and with increasing 5 min intervals up to 60 min. A.) 0.5 mM CaI_2; B.) 1.0 mM CaI_2. Note the presence and in some cases growth of the surface enhanced Rayleigh band present at ≈ 126 cm^{-1}.

C.1 Settling Velocity Estimation

Settling velocities were calculated using both the classical Stokes Law and a modified version that accounts for the fractal nature of the nanoparticle aggregats. Where classical Stokes Law is:

$$v_s = \frac{2}{9}\frac{\rho_p - \rho_f}{\mu} g R^2 \quad (1)$$

Where v_s is the settling velocity, ρ_p is the density of the AuNP, ρ_f is the density of water, μ is the dynamic viscosity of water, g is gravitational acceleration, and R is the radius of the particle (assumed to be spherical.)[1]

The modified form of Stokes Law[2-4] accounts for highly porous or fractal aggregates and is defined as:

$$u^* = \frac{(\rho_p - \rho_f) g \Phi d^2}{18 \mu \Omega} \quad (2)$$

Where u^* is the settling velocity, ρ_p is the density of gold, ρ_f is the density of water, μ is the dynamic viscosity of water, g is the gravitational acceleration, Φ is the volume fraction (assumed to be 0.5), d is the diameter of the aggregate, and Ω is the drag force ratio, calculated by:

$$\Omega = \frac{2\xi^2 \left(1 - \frac{\tanh \xi}{\xi}\right)}{2\xi + 3\left(1 - \frac{\tanh \xi}{\xi}\right)} \quad (3)$$

Where ξ is the non-dimensional permeability of the aggregates calculated by:

$$\xi = \frac{d}{2\sqrt{K}} \quad (4)$$

Where K is the cluster permeability of the aggregates calculated by:

$$K = \frac{2\alpha_p^2}{9\rho}\frac{\left(3 - 4.5\rho^{\frac{1}{3}} + 4.5\rho^{\frac{5}{3}} - 3\rho^2\right)}{\left(3 + 2\rho^{\frac{5}{3}}\right)} \quad (5)$$

Where α_p is the radius of the individual AuNP, and ρ is the aggregate cluster density calculated by:

$$\rho = c\left(\frac{d}{\alpha_p}\right)^{d_f - 3} \quad (6)$$

Where c is the packing density (assumed to be 0.1), and d_f is the fractal dimension, assumed to be 1.7.[5]

Disclosure

This work is being prepared as a manuscript to be submitted to the Royal Chemical Society for consideration to be published as an Article in the journal *Environmental Science: Nano*.

References

1. Stokes, G. G., On the Effect of the Internal Friction of Fluids on the Motion of Pendulums. *Transactions of the Cambridge Philosophical Society* **1851,** *9*, 8.

2. Vikesland, P. J.; Rebodos, R. L.; Bottero, J. Y.; Rose, J.; Masion, A., Aggregation and sedimentation of magnetite nanoparticle clusters. *Environ. Sci.: Nano* **2016,** *3*, (3), 567-577.

3. Li, X.; Logan, B. E., Collision Frequencies of Fractal Aggregates with Small Particles by Differential Sedimentation. *Environ. Sci. Technol.* **1997,** *31*, (4), 1229-1236.

4. Thill, A.; Moustier, S.; Aziz, J.; Wiesner, M. R.; Bottero, J. Y., Flocs Restructuring during Aggregation: Experimental Evidence and Numerical Simulation. *J. Colloid Interface Sci.* **2001,** *243*, (1), 171-182.

5. Berka, M.; Rice, J. A., Relation between Aggregation Kinetics and the Structure of Kaolinite Aggregates. *Langmuir* **2005,** *21*, (4), 1223-1229.